

CANADIAN THESES ON MICROFICHE

I.S.B.N.

THESES CANADIENNES SUR MICROFICHE



National Library of Canada
Collections Development Branch

Canadian Theses on
Microfiche Service

Ottawa, Canada
K1A 0N4

Bibliothèque nationale du Canada
Direction du développement des collections

Service des thèses canadiennes
sur microfiche

NOTICE

The quality of this microfiche is heavily dependent upon the quality of the original thesis submitted for microfilming. Every effort has been made to ensure the highest quality of reproduction possible.

If pages are missing, contact the university which granted the degree.

Some pages may have indistinct print especially if the original pages were typed with a poor typewriter ribbon or if the university sent us a poor photocopy.

Previously copyrighted materials (journal articles, published tests, etc.) are not filmed.

Reproduction in full or in part of this film is governed by the Canadian Copyright Act, R.S.C. 1970, c. C-30. Please read the authorization forms which accompany this thesis.

THIS DISSERTATION
HAS BEEN MICROFILMED
EXACTLY AS RECEIVED

AVIS

La qualité de cette microfiche dépend grandement de la qualité de la thèse soumise au microfilmage. Nous avons tout fait pour assurer une qualité supérieure de reproduction.

S'il manque des pages, veuillez communiquer avec l'université qui a conféré le grade.

La qualité d'impression de certaines pages peut laisser à désirer, surtout si les pages originales ont été dactylographiées à l'aide d'un ruban usé ou si l'université nous a fait parvenir une photocopie de mauvaise qualité.

Les documents qui font déjà l'objet d'un droit d'auteur (articles de revue, examens publiés, etc.) ne sont pas microfilmés.

La reproduction, même partielle, de ce microfilm est soumise à la Loi canadienne sur le droit d'auteur, SRC 1970, c. C-30. Veuillez prendre connaissance des formules d'autorisation qui accompagnent cette thèse.

LA THÈSE A ÉTÉ
MICROFILMÉE TELLE QUE
NOUS L'AVONS RECUE

National Library
of CanadaBibliothèque nationale
du Canada

Canadian Theses Division Division des thèses canadiennes

Ottawa, Canada
K1A 0N4

64033

PERMISSION TO MICROFILM — AUTORISATION DE MICROFILMER

• Please print or type — Écrire en lettres moulées ou dactylographier

Full Name of Author — Nom complet de l'auteur

WONG, Raymond C.L.

Date of Birth — Date de naissance

April 6, 1959

Country of Birth — Lieu de naissance

Hong Kong

Permanent Address — Résidence fixe

383 Hollywood Ave.
WILLOWDALE, Ontario

Title of Thesis — Titre de la thèse

COMPUTATION OF THREE-DIMENSIONAL TURBULENT FLOWS IN LADLES AND TUNDISHES

University — Université

University of Ottawa

Degree for which thesis was presented — Grade pour lequel cette thèse fut présentée

M.A.Sc. (Mechanical Engineering)

Year this degree conferred — Année d'obtention de ce grade

1983

Name of Supervisor — Nom du directeur de thèse

Dr. Martha Salcudean

Permission is hereby granted to the NATIONAL LIBRARY OF CANADA to microfilm this thesis and to lend or sell copies of the film.

The author reserves other publication rights, and neither the thesis nor extensive extracts from it may be printed or otherwise reproduced without the author's written permission.

L'autorisation est, par la présente, accordée à la BIBLIOTHÈQUE NATIONALE DU CANADA de microfilmer cette thèse et de prêter ou de vendre des exemplaires du film.

L'auteur se réserve les autres droits de publication; ni la thèse ni de longs extraits de celle-ci ne doivent être imprimés ou autrement reproduits sans l'autorisation écrite de l'auteur.

Date

February 11, 1983.

Signature

Ray C. L. Wong

COMPUTATION OF THREE-DIMENSIONAL TURBULENT FLOWS
IN LADLES AND TUNDISHES

by

Ray C.L. Wong

A thesis submitted to the School of Graduate Studies in partial
fulfillment of the requirements of the degree of

MASTER OF APPLIED SCIENCE

in the

Department of Mechanical Engineering

University of Ottawa

Ottawa, Canada

1982

© Ray C.L. Wong, OTTAWA, Canada, 1983

UNIVERSITÉ D'OTTAWA / UNIVERSITY OF OTTAWA
École des études supérieures / School of Graduate Studies
et de la recherche and Research

NAME OF AUTHOR WONG, Raymond. C. L.

TITLE OF THESIS COMPUTATION OF THREE-DIMENSIONAL TURBULENT FLOWS IN
LADLES AND TUNDISHES

DEGREE M.A.Sc. (Mechanical Eng.) YEAR GRANTED 1983

The author hereby permits the consultation and the lending of this thesis pursuant to the regulations established by the Librarian of the University of Ottawa. The author also authorizes the University of Ottawa, its successors and assignees, to make reproductions of this copy by photographic means or by photocopying and to lend or sell such reproductions at cost to libraries and to scholars requesting them.

The right to publish the thesis by other means and to sell it to the public is reserved to the author, subject to the regulations of the University of Ottawa governing the publication of theses.

Ray C. L. Wong
(Signed) (Author)

Date: February 11, 1983

Permanent Address:
383 Hollywood Ave.

WILLOWDALE, Ontario

UNIVERSITÉ D'OTTAWA / UNIVERSITY OF OTTAWA
École des études supérieures/School of Graduate Studies

Title of thesis COMPUTATION OF THREE-DIMENSIONAL TURBULENT FLOWS IN
LADLES AND TUNDISHES

Name of candidate WONG, Raymond C.L.

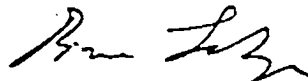
Degree M.A.Sc. Department MECHANICAL ENGINEERING

Date of defence February 11, 1983

This thesis prepared under the supervision of Dr. M. Salcudean has been approved by a jury composed of the following examiners:

DR. W. KOZICKI

DR. S.-C. CHENG



(Dean of Graduate Studies)

COMPUTATION OF THREE-DIMENSIONAL TURBULENT FLOWS
IN LADLES AND TUNDISHES

Dr. Salcudean

(Dr. Martha Salcudean)
Supervisor

Ray C. L. Wong

(Ray C.L. Wong)
Candidate

i

ABSTRACT

This work is aimed at the modelling of flows as applied to steel-making processes. The three dimensional, steady-state equations of motion for incompressible turbulent flow have been numerically integrated. The numerical procedure is based on the SIMPLE algorithm of Patankar and Spalding [1]. The governing equations were solved by means of the control integral volume method. The turbulence was modelled using two transport equations to estimate the local effective viscosity.

The recirculatory flows in gas-agitated reactors with centered and off-centered gas jets and in T-shaped tundishes were considered. The flow in ladles is buoyancy-driven, and the flow in tundishes is forced-convective. The off-centered jet is mid-way between the center line and the side wall. The prediction is extended to include a 150-ton, full-scale industrial ladle. A T-shaped tundish with one inlet and two outlet nozzles is also considered. The flow prediction for the T-shaped tundish is based on a water model of reduced scale. The overall agreement between the computed values and the available data is satisfactory.

ACKNOWLEDGEMENTS.

I wish to express my sincere thanks to my supervisor, Dr. Martha Salcudean for her advice, guidance, inspiration, encouragement and financial assistance throughout this study.

My gratitude also to the National Research Council of Canada for its financial support of the project.

My thanks go to Steven Low from the University of Ottawa and Chushao Xu from McGill University for their co-operation in providing their data, both published and unpublished. The stimulating discussions held with Steven Low, and his valuable suggestions, are appreciated.

Thanks are also due to Henry Knoll and my wife Sandy for their diligence in preparing the typescript of the thesis.

TABLE OF CONTENTS

	<u>Page</u>
ABSTRACT	i
ACKNOWLEDGEMENT	ii
TABLE OF CONTENTS	iii
LIST OF TABLES	vi
LIST OF FIGURES	vii
NOMENCLATURE	xi
 CHAPTER	
1 INTRODUCTION	1
1.1 THE PROBLEM AND ITS PRACTICAL RELEVANCE ..	1
1.2 OUTLINE OF THE PRESENT CONTRIBUTION	3
1.3 LAYOUT OF THE THESIS	4
2 SURVEY OF LITERATURE	6
2.1 NUMERICAL METHODS	6
2.2 TURBULENCE MODELS	8
2.3 THE EFFECTIVE VISCOSITY MODEL	10
2.4 THE K- ϵ MODEL	11
2.5 LADLE-TUNDISH SYSTEM IN CONTINUOUS- CASTING	12
3 MATHEMATICAL FORMULATION	18
3.1 INTRODUCTION	18
3.2 GENERAL EQUATION	18
3.3 TIME-AVERAGED EQUATION	19
3.4 THE K- ϵ EFFECTIVE-VISCOSITY MODEL	20
3.5 EQUATIONS TO BE SOLVED FOR STEADY FLOW ...	22
3.6 GENERAL FORM OF EQUATIONS	25
3.7 TREATMENT OF NEAR-WALL REGIONS	28
3.8 OTHER BOUNDARY CONDITIONS	33

4	THE SOLUTION PROCEDURE	35
4.1	FORMATION OF THE FINITE-DIFFERENCE EQUATION	35
4.1.1	The Grid Arrangement	35
4.2	INTEGRATION OF THE PARTIAL DIFFERENTIAL EQUATIONS	35
4.2.1	Expressions for the Flux Term, F ..	37
4.2.2	Expressions for the Source Term ...	43
4.3	THE SOLUTION OF THE FINITE-DIFFERENCE EQUATION	45
4.3.1	Introduction	45
4.3.2	The Iteration Method	46
4.4	THE PRESSURE CORRECTION EQUATION	46
4.5	THE 'SIMPLE' ALGORITHM	49
4.6	NUMERICAL STABILITY	50
4.6.1	Underrelaxation	50
4.6.2	False Source Term	51
4.6.3	Convergence	52
4.7	COMPUTATIONAL METHODS FOR THE GAS-AGITATED LADLE	53
4.7.1	Description of the Physical Model for Both Centered and Off-Centered Gas-Stirred Ladles	53
4.7.2	Assumptions Made for the Buoyancy Calculation	56
4.7.3	Initial and Boundary Conditions ...	58
4.7.4	Programming Details of Flow Predictions in a Ladle	60
4.8	COMPUTATIONAL METHODS FOR THE PHYSICAL MODEL OF THE T-SHAPED TUNDISH	60
4.8.1	Description of the Physical Model of the T-Shaped Tundish	60
4.8.2	Initial and Boundary Conditions ...	61
4.8.3	Programming Details of Flow Predictions in a Tundish	64
4.9	SUMMARY OF THE COMPUTER PROGRAM	65

5	RESULTS AND DISCUSSION	69
5.1	GENERAL	69
5.2	COMPUTATIONAL PREDICTIONS FOR CENTERED GAS-STIRRED LADLE	69
5.3	FULL-SCALE AND OFF-CENTERED JETTING PREDICTION	73
5.4	COMPUTATIONAL PREDICTIONS FOR A T-SHAPED TUNDISH	76
6	CLOSURE	79
6.1	CONCLUSIONS	79
6.2	RECOMMENDATION FOR FUTURE WORK	80
	REFERENCES	120
	APPENDICES	
A	DERIVATION OF MOMENTUM EQUATIONS	127
B	TRIDIAGONAL MATRIX ALGORITHM	129

LIST OF TABLES

<u>Table</u>		<u>Page</u>
1	Definition of ϕ , Γ , and S_ϕ of equation (19)	25
2	Constants in the Turbulence Model	27
3	Physical and thermal properties data for the three vessels studied	55
4	Physical and thermal properties data for the T-shaped tundish	62

LIST OF FIGURES

<u>Figure</u>		<u>Page</u>
1a	Vertical, bend strand, and curved-mold continuous-casting machines	81
1b	Arrangement of continuous-casting machine at Atlas Steels	81
2	Cell arrangements for Cartesian Coordinates	82
3	A grid cell for cylindrical coordinates	83
4	Function of f_e versus Pe	40
5a	Arrangement of ladle, cover and consumable lance in the vacuum-oxygen decarburization process in Atlas Steels	84
5b	Schematic diagram of centered jet	84
5c	Schematic diagram of off-centered jet ...	84
6	Schematic diagram of the T-shaped tundish	85
7	Schematic diagrams of the T-shaped tundish (half). Planes for which computational results are presented	86
8	A flow chart for the computer program developed	66
9	Computed velocity distribution in vessel 1. Centered jet with slip	87
10	Predicted turbulence kinetic energy distribution in vessel 1. Centered jet with slip	88
11	Predicted effective viscosity distribution in vessel 1. Centered jet with slip	89

12	Predicted characteristic length scale distribution in vessel 1. Centered jet with slip	90
13	Computed velocity distribution in vessel 1. Non-slip centered jet	91
14	Predicted velocity distribution in vessel 1. Non-slip centered jet with average void fraction	92
15a	Szekely's et al experimental flow pattern [54] in vessel 1. Centered jet	93
15b	Salcudean's et al predicted velocity pattern [58] in vessel 1. Centered jet with slip	93
16	Predicted velocity distribution in vessel 2. Centered jet with slip	94
17	Predicted velocity distribution in vessel 2. Non-slip centered jet	95
18	Guthrie's et al experimental flow pattern in vessel 2	96
19	Comparison of experimentally measured [63] and predicted vertical velocity components at different depths in vessel 2	97
20	Predicted velocity distribution in vessel 3. Centered jet with slip	98
21	Predicted turbulence kinetic energy distribution in vessel 3. Centered jet with slip	99
22	Predicted effective viscosity distribution in vessel 3. Centered jet with slip	100
23	Predicted characteristic length scale distribution in vessel 3. Centered jet with slip	101

24	Schematic diagram of an off-centered gas jetting ladle	102
25a	Predicted velocity distribution in vessel 1. Off-centered jet with slip ...	103
25b	Salcudean's et al predicted velocity distribution in vessel 1. Off-centered jet with slip	103
26	Predicted velocity distribution in vessel 3. Non-slip off-centered jet	104
27	Predicted turbulence kinetic energy distribution in vessel 3. Non-slip off-centered jet	105
28	Predicted effective viscosity distribution in vessel 3. Non-slip off-centered jet	106
29	Predicted effective viscosity distribution in vessel 3. Non-slip off-centered jet. (Half cross-section through the top of the vessel is illustrated)	107
30	Predicted characteristic length scale distribution in vessel 3. Non-slip off-centered jet	108
31	Predicted velocity distribution. Plane, IX=19 (see Fig. 7), in the T-shaped tundish	109
32	Predicted velocity distribution. Plane, IZ=8 (see Fig. 7), in the T-shaped tundish	110
33	Predicted velocity distribution. Plane, IY=20 (see Fig. 7), in the T-shaped tundish	111
34	Predicted velocity distribution. Plane, IX=7 (see Fig. 7), in the T-shaped tundish	112

35	Predicted velocity distribution. Plane, IY=8 (see Fig. 7), in the T-shaped tundish	112
36	Experimental flow direction in the T-shaped tundish	113
37	Predicted temperature distribution. Plane, IX=9 (see Fig. 7), in the T-shaped tundish	114
38	Predicted temperature distribution. Plane, IZ=2 (see Fig. 7), in the T-shaped tundish	115
39	Predicted temperature distribution. Plane, IY=20 (see Fig. 7), in the T-shaped tundish	116
40	Predicted turbulence kinetic energy distribution. Plane, IY=8 (see Fig. 7) in the T-shaped tundish	117
41	Predicted temperature distribution. Plane, IY=8 (see Fig. 7), in the T-shaped tundish	117
42	Predicted turbulence kinetic energy distribution. Plane, IX=9 (see Fig. 7) in the T-shaped tundish	118
43	Predicted turbulence kinetic energy distribution. Plane, IZ=2 (see Fig. 7) in the T-shaped tundish	119

NOMENCLATURE

<u>Symbol</u>	<u>Definition</u>
A	Area, m ²
A ₊	Constant in the length scale expression
a	Coefficients in the algebraic equation for the line solution procedure
C ₁ , C ₂	Constants in the modelled ε-equation
C _μ	Constant in the effective viscosity expression
C _D	Constant in the dissipation term of the K-equation
C _j	Coefficients in the algebraic equation for the line solution procedure
C _P	Specific heat of fluid at constant pressure, J/kg-°K
D	Diffusion term
E	Integration constant in the wall region
e _{ij}	Rate of strain tensor ($= \frac{\partial U_i}{\partial x_j} + \frac{\partial U_j}{\partial x_i}$), s ⁻¹
F	Flux at the control volume boundary
f	Weight factor
G	Generation of turbulence energy
g	Gravitational acceleration
\hat{h}	Total specific energy ($= h + \frac{1}{2} U_j U_j$), kJ/kg
h	Specific enthalpy ($= h_{ref} + \int_{T_{ref}}^T C_p dT$), kJ/kg

IX	Planes normal to the x-axis
IY	Planes normal to the y-axis
IZ	Planes normal to the z-axis
K	Turbulence kinetic energy $(= \frac{1}{2} \overline{U_i U_i})$, m^2/s^2
l	Characteristic dissipation length scale
NX	Total number of cells in x (or θ) direction
NY	Total number of cells in y (or r) direction
NZ	Total number of cells in z direction
p	p-function in the wall-function method
P	Local pressure, N/m^2
P'	Pressure correction, N/m^2
Pe	Peclet number $(= \rho u L / \Gamma)$
Pr	Prandtl number $(= C_p \mu / \lambda)$
Q	Heat flux, W/m^2
r	Radius (in Cartesian coordinates, $r = 1$ & $\partial r = \partial y$), m
R	Radius of the ladle, m
R_c	Estimate for the radial width of gas-liquid mixture column, m
Re	Reynolds number $(= U \Delta r / \nu)$
R_ϕ	Total divergence
S	Source term in the conservation equation
S_h	Energy source due to radiation, electrical heat, etc.
T	Local fluid temperature, $^{\circ}K$

t	Time, sec
U^+	Non-dimensional velocity in the wall region (= U/U_τ)
U_τ	Friction velocity (= $\sqrt{\tau_w/\rho}$)
W_{slip}	Relative velocity of the gas bubble to its surrounding liquid
U, V, W	Mean velocity component in the x-, y- and z- directions respectively in rectangular coordi- nates; mean velocity component in the θ -, r- and z-direction respectively in cylindrical coordinates, m/s
u, v, w	Velocity fluctuation component in the x-, y- and z-direction respectively, m/s
v'	Characteristic velocity of the velocity fluctu- ation field
VOL	Cell volume, m^3
x, y, z	General Cartesian coordinates
y^+	Non-dimensional distance from the wall (= $\rho U_\tau y/\mu$)

Greek lettersDefinition

ϵ	Dissipation rate of turbulence kinetic energy
κ	Von Karman constant
λ	Thermal conductivity, $W/m\text{-}^\circ K$
Γ_h, Γ	Exchange coefficient (= μ/σ)
Γ_t	Turbulent diffusivity
μ	Dynamic viscosity, $kg/m\text{-}sec$
ν	Kinematic viscosity, m^2/sec

ρ	Fluid density, kg/m^3
τ	Shear stress, N/m^2
ϕ	General variable
σ	Prandtl number
σ_K	Constant in the modelled K-equation
σ_ϵ	Constant in the modelled ϵ -equation
γ	Relaxation factor
θ	Angle in angular direction
α	Void fraction
$\bar{\alpha}$	Average void fraction in a horizontal level
δ	Constant, equal to 1 for cylindrical coordinates, equal to 0 for Cartesian coordinates

SubscriptsDefinition

1,2,3	Direction of Cartesian coordinate system
E,e	"East" side of the cell
eff	Effective (molecular plus turbulent)
f	False
g	Gas
H,h	"High" side of the cell
inlet	For inlet boundary
L,l	"Low" side of the cell
liq	Liquid

lam	Laminar
K	For kinetic energy of turbulence
N,n	"North" side of the cell
outlet	For outlet boundary
outlet-1	For the cell just before the outlet boundary
p	Center node of control volume
ref	Reference
slip	With slip condition
S,s	"South" side of the cell
t	Turbulent
W	Wall value
W,w	"West" side of the cell
wall	At wall
ϵ	For dissipation rate of turbulence energy

SuperscriptsDefinition

'	Fluctuation quantity; correction
—	Average value
*	Gussed value

CHAPTER 1
INTRODUCTION

1.1 THE PROBLEM AND ITS PRACTICAL RELEVANCE

In most continuous-casting machines, various ladle-tundish systems (Fig. 1) are used. This thesis investigates the hydrodynamics of the gas-stirred ladles and the T-shaped tundish. A better understanding of the fluid flow in these components may lead to the improvement of the design of the metallurgical operations and the quality of the final product.

Ladle-metallurgical operations involve the injection of reactants, such as deoxidizers, desulphurizing agents, or the alloying additions, into ladles containing molten steel which is being agitated either by an electromagnetic force or by an injected gas stream. One of the most important application is the argon-stirred ladle, where a stream of argon bubbles is injected into a metal bath to promote homogenization and deoxidation of the steel.

The stirring of the steel results in uniform temperatures during teeming. This is particularly important for continuous casting. Stirring also makes for lower teeming temperatures for some grades of steel possible. Stirring

the steel in the ladle improves precision in determining heat composition; therefore, the addition of expensive alloying elements can be closely controlled.

The amount of dissolved gas can also be greatly reduced by chemical reactions as for example the removal of oxygen by using such deoxidizers as aluminum, manganese, or silicon. Those deoxidizers react with the oxygen in steel; consequently, oxides are formed. This method has the disadvantage of leaving small particles of oxidized products like alumina or silica in the metal. Impurities in the form of oxides, sulfides, and silicates may be present in metals either in solution or as separate particles called inclusions. Such impurities generally impair the properties of the metal or alloy.

The performance of the tundish is essential, because the circulation generated in it not only causes inclusions to float to the surface of the molten steel, but also supplies a constant uniform flow to the mold. Since tundish teeming has these advantages over direct teeming, various tundish designs have been developed from water-model tests. A T-shaped tundish with baffles and two pouring nozzles was designed as an alternative to the trough-shaped tundish, to promote a flow that proceeds up to the surface and then turns down directly above the nozzles. Segregation of inclusions

takes place on the free surface. Tundish powder is used to absorb inclusions and then form a layer of slag. In the case of alumina, clusters of alumina are formed. The slag can be easily skimmed off.

The difference between the temperature of the liquid metal and the temperature of the metal at the beginning of solidification is called superheat. The variation of the superheat in the tundish during the continuous-casting process affects the solidification speed of the metal in the mold. If the superheat is too low, blocking of the teeming nozzle could occur. If the superheat is too high, an increase of the formation of internal cracks and axial porosity can be observed. Hence, a small variation of the teeming temperature is desired.

1.2 OUTLINE OF THE PRESENT CONTRIBUTION

The purpose of this work is to obtain a greater insight into the fluid-flow phenomena, and the heat and mass transfer in bubble-stirred and forced convection systems. A three-dimensional model was developed to investigate the three-dimensional, turbulent flow in gas-stirred ladles and tundishes. The three-dimensional model developed can handle both rectangular and cylindrical coordinates. It is built with variable mesh size.

In this study, the two-equation model of turbulence is used. Local turbulent viscosity is determined from the solution of transport equations for the kinetic energy of turbulence and the energy dissipation rate. The numerical procedure developed is based on the SIMPLE algorithm with hybrid central and upwind differentiating scheme by Patankar and Spalding [1].

The flow in the gas-stirred ladles and T-shaped tundishes has been predicted. Predicted results of the flow in ladles were compared with the available data from experimental water modeling. Full-scaled runs with industrial specifications were also tested. A vessel with an off-centered gas jet was also studied. The flow prediction for the T-shaped tundish which has one inlet and two outlet nozzles is based on a reduced-scale water model. The agreement between the computed values and the available data is satisfactory.

1.3 LAYOUT OF THE THESIS

The main body of the thesis consists of six chapters. A brief review of the related literature on mathematical turbulence models is presented in Chapter 2. Chapter 3 deals with the mathematical modelling where the exact and final forms of the governing equations of motion are presented. In Chapter 4, the numerical methods and prediction methods

are discussed. Chapter 5 presents the investigation of gas-stirred ladles and a T-shaped tundish. Chapter 6 summarizes the results of the study and provides some recommendations for future work.

CHAPTER 2

SURVEY OF LITERATURE

2.1 NUMERICAL METHODS

Numerical methods for the solution of the equations governing fluid flow have been extensively developed. One of the early successful numerical methods for the solution of these equations is the two-dimensional boundary layer procedure of Patankar and Spalding [2] [3]. Shortly after, another two-dimensional procedure for "general flow", i.e., flow in which recirculation may occur, was devised by Gosman et al [4]. Other two- and three-dimensional methods for steady and unsteady flows have also been reported by Harlow and Welch [5], Amsden and Harlow [6] and many others.

A method for the calculation of two-dimensional boundary-layer flows was reported by Gosman and Spalding [7]. This was later revised by Patankar and Spalding [1] who derived a procedure called SIMPLE (see Chapter 4), and made it applicable to two- and three-dimensional general flow. SIMPLE has so far been one of the most popular procedures for calculating general flows, and has been applied in various flow conditions. Pratap and Spalding [8] described a numerical procedure which made use of the SIMPLE algorithm

7

for the calculation of partially parabolic flow situations. Based on the similar numerical procedure, Majumdar et al [9] predicted two-dimensional flows in gas-agitated reactors. Later on, Markatos et al [10] applied the same technique to predict turbulent flows around bodies of irregular shapes. Again, Pollard and Spalding [11] predicted a three-dimensional turbulent parabolic flow field in a flow-splitting T-junction based on a similar numerical procedure. Patankar [12] summarized this numerical procedure in detail and showed how it can have other applications such as in a steam generator.

Revised versions of the SIMPLE algorithm in various applications can be found in Rodi and Srivatsa [13] and Serge-Eldin and Spalding [14]. Rodi and Srivatsa [13] extended the partially parabolic procedure of Pratap and Spalding [8] to flows where local reverse-flow regions occur by treating these regions as being elliptic. Serge-Eldin and Spalding [14] described a numerical prediction which handled the cyclic boundary conditions efficiently in can-combustor problems. Various problems related to the prediction of turbulent flow using a two-equation model were reviewed by Launder and Spalding [15]. Spalding [16] has reviewed the central difference scheme. He also has shown that the upwind difference scheme of formulating differential expressions, in problems involving transport

by simultaneous convection and diffusion, is superior to the central difference scheme, when the local Peclet number of the grid is large. However, a combination of the central difference scheme and the upwind difference scheme, i.e. a hybrid scheme, is somewhat more accurate than the upwind difference scheme. Recently, Leschziner [17] examined the performance of three steady-state, finite-difference schemes, namely, (i) the hybrid central/upwind, (ii) the hybrid central/skew-upwind and (iii) the quadratic, upstream-weighted differencing schemes. A revised version of the SIMPLE algorithm exists for various special flow conditions, yet it is believed that the original SIMPLE is still one of the most popular procedures in the field of numerical prediction of the turbulent flow.

2.2 TURBULENCE MODELS

There has been extensive research into the nature of turbulence and its approximate mathematical representation. In the early work of Prandtl [18], turbulence stresses have been related to velocity gradients through a prescribed length-scale distribution; i.e., scales representing typical sizes of the turbulent eddies. Since then research on turbulence phenomena has led to methods for obtaining the turbulence stresses from one or two equations of characteristic

variables of the turbulence field. Among such models are: the one-differential-equation models of Prandtl [19], Bradshaw [20]; and the two-differential-equation models of Kolmogorov [21], Harlow and Nakayama [22], Spalding [23], Jones and Launder [24], Launder and Spalding [25]. Other more complicated models, like the Reynolds stress model of turbulence, have been investigated by Hanjalic and Launder [26].

Prandtl [19] and Kolmogorov [21] proposed that the turbulent viscosity should be proportional to the square root of the turbulence kinetic energy and a length scale representative of the energy-containing eddies.

Van Driest [27] suggested that the effective viscosity is given by the sum of the laminar and turbulent viscosity; i.e.,

$$\mu_{\text{eff}} = \mu_{\text{lam}} + \rho \ell^2 \left| \frac{\partial U}{\partial y} \right|$$

$$\text{where } \ell = \kappa y \left[1 - \exp\left(-\frac{y^+}{A_+} \right)^{1/2} \right]^{1/2}$$

$$A_+ = 26.0$$

Patankar and Spalding [2] showed that the Prandtl mixing-length hypothesis could be used to provide accurate predictions for a wide variety of boundary-layer flows. They used algebraic wall functions for this region. The wall

functions were based on a modification to the Van Driest [27] proposal. They proposed that the mixing length ℓ is modified by viscosity according to the formula:

$$\ell = \kappa y \{1 - \exp[- (\frac{\tau}{\rho}) y / \nu A_+]\}$$

where τ is the local shear stress. The turbulent viscosity is then obtained from the mixing-length relation:

$$\mu_t = \rho \ell^2 \left| \frac{\partial U}{\partial y} \right|$$

and the Prandtl's turbulent number is assumed to be

$$\sigma_t \equiv \frac{\mu_t C_P}{\lambda_t} = 0.9$$

Shortly after, a model similar to the mixing-length model was adopted by Harlow and Nakayama [22], and Spalding [23] wherein convective transport equations are solved for two scalar properties of turbulence; namely, turbulent kinetic energy and its dissipation rate. Later on, Jones and Launder [24] proposed another form of the two-equation model for regions where the Reynold's number is low. In recent years, the two-equation model has been widely used and reported satisfactory by authors mentioned in the previous subsection.

2.3 THE EFFECTIVE VISCOSITY MODEL

In "effective viscosity" models, the turbulent diffusional fluxes are expressed in terms of "effective diffusivities"

(or "exchange coefficients"; e.g., turbulent viscosity and turbulent diffusivity Γ_t) multiplying gradients of mean properties. According to Prandtl [18], the general relation of μ_t and local properties of turbulence is

$$\mu_t = C_\mu \rho V' \ell$$

The effective viscosity is obtained from

$$\mu_{\text{eff}} = \mu_{\text{lam}} + \mu_t$$

2.4 THE K- ϵ MODEL

Kolmogorov [21] and Prandtl [19] proposed that V' is equivalent to the square root of the kinetic energy of turbulence, K . Hence the time-mean rate of dissipation of turbulence energy is related to K and ℓ through

$$\epsilon = K^{3/2} \ell^{-1}$$

The essence of the K- ϵ model is that the turbulence can be described through two transport equations; i.e., the K equation and the ϵ equation (Chou, [28]; Harlow and Nakayama, [22]; Jones and Launder, [24]). Thus, in terms of K and ϵ ,

$$\mu_t = C_\mu \rho \frac{K^2}{\epsilon}$$

In this study, the K- ϵ equations have been modelled in the form introduced by Launder and Spalding [15] as described in Chapter 3.

2.5 LADLE-TUNDISH SYSTEM IN CONTINUOUS-CASTING

In recent years, metallurgical research has aimed to improve the design of various metallurgical components. In ladle metallurgy, the removal of unwanted elements (S, Si, P, O, C, H, N) from iron and steel improved overall product quality. Close quality control of inclusions, dissolved gas contents, etc. has been achieved. Most ladles use gas injected through a submerged lance, plug, or nozzle to stir the contents of the ladle. This injected gas promotes temperature and chemical homogeneities and, through the generation of turbulence, aids inclusion agglomeration and float-out. The essence of composition and temperature control in ladle-tundish systems were discussed by Widdowson [29]. The existing methods of ladle-flushing, ladle injection, and vacuum-degassing were also summarized. Guthrie [30] gave predictions of the tapping operation - pouring molten steel from one vessel to another - in ladle metallurgy. Some in-plant experience and research were presented by The Iron & Steel Institute [31]; Leclerc et al [32]; Relander et al [33]; Whitake and Palmer [34]; Grip et al [35]. Leclerc et al explained how various parameters, such as casting temperature, casting speed, stream protection between ladle and tundish, design of tundish, and the shape of submerged nozzles affect continuous casting of plates and sheets. Relander et al have

shown the progress of the developmental work on various nozzle shapes in a tundish. On the basis of in-plant studies at Atlas Steel, Whitaker and Palmer concluded that the stirring of molten steel in the ladle gives very uniform temperatures and a low rate of temperature variation during teeming. Stirring the steel in the ladle also improves precision in determining heat composition.

A common technique used to observe flow phenomena is water-modelling. Usually a scale factor of one-third or one-fourth is used for metallurgical process modelling because performing experimental work for a 100- to 400-ton steel-reactor is time- and money-consuming. Hlinka [36] had examined the use of water models and related scaling problems in ladle-tundish-mold system. Other water models reported were those by Robertson and Sheridan [37], Hlinka and Miller [38]. Robertson and Sheridan investigated various nozzle designs in a triangular tundish. Hlinka and Miller compared the temperature of both ladle and tundish in the 7-1/2 -ton melt shop heat* with a one-sixth scale water model during teeming. They also gave a mathematical proof that hot water

* A batch of molten steel heated up in the furnance before being poured into the ladle.

contained in acrylic plastic can be used to model steel contained in refractory vessels, if certain scaling requirements are fulfilled.

Mathematical models are often used to predict the flow and temperature distributions in ladle-tundish-mold systems. Salcudean and Guthrie [39] [40] investigated the ladle-tapping operation. Issa and Gosman [41] also studied turbulent two-phase flow in stirred vessels equipped with a central axisymmetric impeller. Heat losses in a ladle and tundish were considered by Alberny and Leclercq [42]. Szekely and Yadoya [43]; Brimacombe et al [44] examined flow and temperature field in the upper region of the liquid pool in the mold region. Solidification and cooling of cast roll was examined by Spencer et al [45]; Stanek and Szekely [46]. Asai and Szekely [47]; Mizikar [48]; Perkins and Irvind [49] investigated solidification and velocity profiles in a slab mold. Velocity fields in an inductively stirred ladle were reported by Szekely et al [50] [51]. El-Kaddah and Szekely [52] calculated the rate of desulphurization in ladle metallurgical operation. Development of horizontal continuous casting was analyzed by Miyashita et al [55]. Most of the mathematical predictions by all these researchers were compared with experimental data from water-modelling. Reasonable agreement between the two was reported.

In recent years, gas-stirred reactors have been playing an increasingly important role in metallurgical operations. Gas-stirring induces motion in the fluid, thus enhancing chemical reaction, improving precision in determining heat composition and minimizing temperature heterogeneities. A number of hydrodynamic studies have been performed to gain a better understanding of the fluid flow phenomena in the gas-stirring process. Early experimental studies were mainly based on reduced-scale water models. For example, Szekely et al [54] attempted two-dimensional water-modelling of an argon-stirred ladle. In their mathematical model, the gas jet core was modelled as a solid wall moving upward at constant velocity. The K-W two-equation model of turbulence was used to predict the flow field. Reasonable agreement was found between the prediction and the experimental velocity field.

Another two-dimensional mathematical model which was based on a buoyancy-driven flow was first presented by Deb Roy et al [55] and more recently by Szekely et al [56]. In both models, the average void fraction in a horizontal plane was calculated by using the inlet gas flow rate to estimate the plume velocity. The plume was modelled as a vertical cylinder. Both slip and non-slip conditions (see Chapter 4) were tested. For the slip condition, the gas was assumed to move with a velocity, W_{slip} , relative to the surrounding

liquid. Patankar and Spalding's [1] numerical method was used. A constant effective viscosity, suggested by Pun and Spalding [57] for confined jets, was used in both works.

Many industrial applications such as off-centered gas-jetting in ladle metallurgy involve three-dimensional flows. However, the literature on investigations of this nature is limited. Most recently, Salcudean et al [58] described a three-dimensional mathematical model which used a finite difference technique based on the MAC-Los Alamos method. Centered, off-centered, cylindrical and conical jets with slip and non-slip conditions were studied. Again, a constant effective viscosity similar to the one suggested by Pun and Spalding [57] was used.

The three-dimensional mathematical model used in this study is based on the K- ϵ two-equation differential model of turbulence (Salcudean et al [59]). Flow patterns and turbulence characteristics were derived for centered and off-centered gas jets. The energy equation for analyzing the heat flow characteristics was solved. Plume voids were estimated for both slip and non-slip conditions. The plume is modelled as a vertical cylinder. Predictions are compared with available data. The author understands that there are no existing mathematical models in the literature which describe the three-dimensional flow in tundishes. In this

thesis, computations are carried out to investigate the flow in a T-shaped tundish. The computational method and program developed and applied to investigate argon-stirring and the flow in the tundish can be adapted to other three-dimensional flows (e.g. flow in the mold during continuous casting).

CHAPTER 3

MATHEMATICAL FORMULATION

3.1 INTRODUCTION

This chapter presents the mathematical foundation on which the present study is based. The prediction of all turbulent flows requires the formulation of the governing equations in the form of a closed set.

Section 3.2 presents the time-dependent equations of motion and energy, while Section 3.3 presents the time-averaged form. In Section 3.4, the unknown fluxes are determined by means of a turbulence model. Sections 3.5 and 3.6 summarize the complete set of equations in standard form. Section 3.7 gives the boundary conditions of the flows considered in this study.

3.2 GENERAL EQUATION

The basic conservation equations which govern natural and forced convection, are those for mass, momentum, and energy. They may be expressed in Cartesian tensor notation as follows:

$$\text{Mass conservation: } \frac{\partial \rho}{\partial t} + \frac{\partial}{\partial x_j} (\rho U_j) = 0 \quad (1)$$

Momentum conservation (for direction i , $i=1,2,3$):

$$\frac{\partial}{\partial t}(\rho U_i) + U_j \frac{\partial}{\partial x_j}(\rho U_i) = - \frac{\partial P}{\partial x_i} + \frac{\partial}{\partial x_j}(\mu e_{ij}) + \rho g_i \quad (2)$$

Energy conservation:

$$\begin{aligned} \frac{\partial}{\partial t}(\rho h) + U_j \frac{\partial}{\partial x_j}(\rho h) = & -P \frac{\partial U_j}{\partial x_j} + \frac{\partial}{\partial x_j}(\Gamma_h C_P \frac{\partial T}{\partial x_j}) \\ & + \mu(e_{ij}) \frac{\partial U_i}{\partial x_j} + S_h \end{aligned} \quad (3)$$

3.3 TIME-AVERAGED EQUATION

The instantaneous value $\hat{\phi}$ of any variable can be decomposed into a time-average (or mean) component $\bar{\phi}$ and a fluctuating component ϕ' . For steady flow, $\bar{\phi}$ is expressed as:

$$\bar{\phi} = \lim_{t \rightarrow \infty} \frac{1}{t} \int_0^t \hat{\phi} dt$$

$$\hat{\phi} = \bar{\phi} + \phi'$$

ϕ may stand for any of the variables ρ , U_i , P , h and T . Therefore, in steady-state flow, after time-averaging, the governing equations become*:

for continuity:

$$\frac{\partial}{\partial x_j}(\rho U_j) = 0 \quad (4)$$

*Capital letters in equations below stand for average quantities.

for momentum:

$$U_j \frac{\partial}{\partial x_j} (\rho U_i) = - \frac{\partial P}{\partial x_i} + \frac{\partial}{\partial x_j} \left[\mu \left(\frac{\partial U_j}{\partial x_i} + \frac{\partial U_i}{\partial x_j} \right) - \overline{\rho u_i u_j} \right] + \rho g_i \quad (5)$$

for energy:

$$U_j \frac{\partial}{\partial x_j} (\rho h) = \frac{\partial}{\partial x_j} \left(- \rho u_j h' + \Gamma_{h,P} C_P \frac{\partial T}{\partial x_j} \right) + S_h \quad (6)$$

3.4 THE K-ε EFFECTIVE-VISCOSITY MODEL

For the time-average equation, new unknown terms such as the Reynolds stresses $(-\overline{\rho u_i u_j})$ and the turbulent heat flux $(-\overline{\rho u_j h'})$ arise. Hinze [60] suggested that

$$-\overline{\rho u_i u_j} = \mu_t \left(\frac{\partial U_i}{\partial x_j} + \frac{\partial U_j}{\partial x_i} \right) \quad (7)$$

$$-\overline{\rho \phi' u_j} = \Gamma_{\phi,t} \frac{\partial \phi}{\partial x_j} \quad (8)$$

Prandtl [18] suggested

$$\mu_t = C_\mu \rho V' l$$

The effective viscosity is obtained from

$$\mu_{\text{eff}} = \mu_{\text{lam}} + \mu_t$$

where μ_{lam} and μ_t are the laminar and turbulent viscosities respectively.

Kolmogorov [21] and Prandtl [19] proposed

$$\mu_t = C_\mu \rho K^{1/2} l^2$$

(K = kinetic energy of turbulence);

Chou [28], Harlow and Makayama [22] and Jones and
Launder [24] proposed

$$\varepsilon = K^{3/2} l^{-1}$$

(ε = time-mean rate of dissipation of turbulence energy)

to yield:

$$\mu_t = C_\mu \rho K^2 / \varepsilon \quad (9)$$

The modelled form of K- ε equations by Launder and
Spalding [15], neglecting the buoyancy effect, is

$$\underbrace{\frac{\partial}{\partial x_j} (\rho U_j K)}_I = - \underbrace{\rho u_i u_j \frac{\partial U_i}{\partial x_j}}_{II} + \underbrace{\frac{\partial}{\partial x_j} \left(\frac{\mu_t}{\sigma_K} \frac{\partial K}{\partial x_j} \right)}_{III} - \underbrace{\rho \varepsilon C_D}_{IV} \quad (10)$$

$$\underbrace{\frac{\partial}{\partial x_j} (\rho U_j \varepsilon)}_I = - C_1 \frac{\varepsilon}{K} \underbrace{\rho u_i u_j \frac{\partial U_i}{\partial x_j}}_{II} + \underbrace{\frac{\partial}{\partial x_j} \left(\frac{\mu_t}{\sigma_\varepsilon} \frac{\partial \varepsilon}{\partial x_j} \right)}_{III} - \underbrace{C_2 \rho \frac{\varepsilon^2}{K}}_{IV} \quad (11)$$

I = convection by mean motion

II = generation by turbulence stresses acting on
mean flow

III = diffusive transport

IV = viscous dissipation

C_1 , C_2 , σ_K , σ_ϵ , C_D are empirical functions (assumed to be constant at high Reynolds numbers).

3.5 EQUATIONS TO BE SOLVED FOR STEADY FLOW

The following conservation equations can be applied to both Cartesian and cylindrical coordinates. For cylindrical coordinates, δ is set to 1; for Cartesian coordinates, δ is set to 0 and r is replaced by l . Also, $\partial\theta$ is replaced by ∂x and ∂r by ∂y . The conservation of momentum equations are derived from the Navier-Stokes equations. The velocities and pressures are expressed as mean and fluctuating components. After the time-averaging step (see Section 3.3) and the rearrangement of the convective terms (see Appendix A), the momentum equations can be obtained in the form expressed in this section:

Continuity equation:

$$\frac{\partial(\rho V)}{\partial r} + \frac{1}{r} \frac{\partial(\rho U)}{\partial \theta} + \frac{\partial(\rho W)}{\partial z} + \delta \frac{\rho V}{r} = 0 \quad (12)$$

Momentum equations:Radial:

$$\begin{aligned}
& \frac{1}{r} \frac{\partial}{\partial r} (r \rho V V) + \frac{1}{r} \frac{\partial}{\partial \theta} (\rho U V) + \frac{\partial}{\partial z} (\rho V W) - \frac{1}{r} \frac{\partial}{\partial r} (\mu_{\text{eff}} r \frac{\partial V}{\partial r}) \\
& - \frac{1}{r} \frac{\partial}{\partial \theta} (\mu_{\text{eff}} r \frac{\partial V}{\partial \theta}) - \frac{\partial}{\partial z} (\mu_{\text{eff}} \frac{\partial V}{\partial z}) - \frac{\partial}{\partial z} (\mu_{\text{eff}} \frac{\partial W}{\partial r}) - \frac{1}{r} \frac{\partial}{\partial r} (r \mu_{\text{eff}} \frac{\partial V}{\partial r}) \\
& - \frac{1}{r} \frac{\partial}{\partial \theta} (r \mu_{\text{eff}} \frac{\partial}{\partial r} (\frac{U}{r})) + \delta \frac{2\mu_{\text{eff}}}{r} \frac{\partial U}{\partial \theta} + \delta \frac{2\mu_{\text{eff}}}{r} V - \delta \frac{\rho U^2}{r} \\
& + \frac{\partial P}{\partial r} + \rho g_r = 0 \tag{13}
\end{aligned}$$

Axial:

$$\begin{aligned}
& \frac{1}{r} \frac{\partial}{\partial r} (r \rho V W) + \frac{1}{r} \frac{\partial}{\partial \theta} (\rho U W) + \frac{\partial}{\partial z} (\rho W W) - \frac{1}{r} \frac{\partial}{\partial r} (\mu_{\text{eff}} r \frac{\partial W}{\partial r}) \\
& - \frac{1}{r} \frac{\partial}{\partial \theta} (\mu_{\text{eff}} r \frac{\partial W}{\partial \theta}) - 2 \frac{\partial}{\partial z} (\mu_{\text{eff}} \frac{\partial W}{\partial z}) - \frac{1}{r} \frac{\partial}{\partial r} (r \mu_{\text{eff}} \frac{\partial V}{\partial z}) \\
& - \frac{1}{r} \frac{\partial}{\partial \theta} (\mu_{\text{eff}} \frac{\partial U}{\partial z}) + \frac{\partial P}{\partial z} + \rho g_z = 0 \tag{14}
\end{aligned}$$

Angular:

$$\begin{aligned}
& \frac{1}{r} \frac{\partial}{\partial r} (r \rho U V) + \frac{1}{r} \frac{\partial}{\partial \theta} (\rho U U) + \frac{\partial}{\partial z} (\rho U W) - \frac{1}{r} \frac{\partial}{\partial r} (\mu_{\text{eff}} r \frac{\partial U}{\partial r}) \\
& - \frac{1}{r} \frac{\partial}{\partial \theta} (\mu_{\text{eff}} r \frac{\partial U}{\partial \theta}) - \frac{\partial}{\partial z} (\mu_{\text{eff}} \frac{\partial U}{\partial z}) - \frac{\mu_{\text{eff}}}{r} \frac{\partial^2 W}{\partial \theta \partial z} \\
& - \frac{1}{r} \frac{\partial}{\partial r} (\mu_{\text{eff}} r (\frac{1}{r} \frac{\partial V}{\partial \theta} - \delta \frac{U}{r})) + \rho \delta \frac{U V}{r} - \frac{\partial}{\partial \theta} (\frac{\mu_{\text{eff}}}{r} (\frac{\partial U}{\partial \theta} + \delta 2V)) \\
& - \delta \frac{\mu_{\text{eff}}}{r} (\frac{\partial U}{\partial r} + \frac{\partial V}{r \partial \theta} - \frac{U}{r}) + \frac{\partial P}{r \partial \theta} + \rho g_\theta = 0 \tag{15}
\end{aligned}$$

Energy equation:

$$\begin{aligned} & \frac{1}{r} \frac{\partial}{\partial r} (r \rho V T) + \frac{1}{r} \frac{\partial}{\partial \theta} (\rho U T) + \frac{\partial}{\partial z} (\rho W T) - \frac{1}{r} \frac{\partial}{\partial r} \left(\frac{\mu_{\text{eff}}}{\sigma_{\text{eff}}} r \frac{\partial T}{\partial r} \right) \\ & - \frac{1}{r} \frac{\partial}{\partial \theta} \left(\frac{\mu_{\text{eff}}}{\sigma_{\text{eff}}} \frac{\partial T}{r \partial \theta} \right) - \frac{\partial}{\partial z} \left(\frac{\mu_{\text{eff}}}{\sigma_{\text{eff}}} \frac{\partial T}{\partial z} \right) + S_h = 0 \end{aligned} \quad (16)$$

$$\text{where } \frac{\mu_{\text{eff}}}{\sigma_{\text{eff}}} = \frac{\mu}{\sigma} + \frac{\mu_t}{\sigma_t}$$

Turbulence kinetic energy equation:

$$\begin{aligned} & \frac{1}{r} \frac{\partial}{\partial r} (r \rho V K) + \frac{1}{r} \frac{\partial}{\partial \theta} (\rho U K) + \frac{\partial}{\partial z} (\rho W K) - \frac{1}{r} \frac{\partial}{\partial r} \left(\frac{\mu_{\text{eff}}}{\sigma_K} r \frac{\partial K}{\partial r} \right) \\ & - \frac{1}{r} \frac{\partial}{\partial \theta} \left(\frac{\mu_{\text{eff}}}{\sigma_K} \frac{\partial K}{r \partial \theta} \right) - \frac{\partial}{\partial z} \left(\frac{\mu_{\text{eff}}}{\sigma_K} \frac{\partial K}{\partial z} \right) - \mu_{\text{eff}} G + \rho \epsilon C_D = 0 \end{aligned} \quad (17)$$

$$\begin{aligned} \text{where } G \equiv & 2 \left[\left(\frac{\partial W}{\partial z} \right)^2 + \left(\frac{\partial V}{\partial r} \right)^2 + \left(\frac{\partial U}{r \partial \theta} + \delta \frac{V}{r} \right)^2 \right] + \left(\frac{\partial W}{\partial r} + \frac{\partial V}{\partial z} \right)^2 \\ & + \left(\frac{\partial U}{\partial z} + \frac{\partial W}{r \partial \theta} \right)^2 + \left(\frac{\partial V}{r \partial \theta} + \frac{\partial U}{\partial r} - \delta \frac{U}{r} \right)^2 \end{aligned}$$

Energy dissipation:

$$\begin{aligned} & \frac{1}{r} \frac{\partial}{\partial r} (r \rho V \epsilon) + \frac{1}{r} \frac{\partial}{\partial \theta} (\rho U \epsilon) + \frac{\partial}{\partial z} (\rho W \epsilon) - \frac{1}{r} \frac{\partial}{\partial r} \left(\frac{\mu_{\text{eff}}}{\sigma_\epsilon} r \frac{\partial \epsilon}{\partial r} \right) \\ & - \frac{1}{r} \frac{\partial}{\partial \theta} \left(\frac{\mu_{\text{eff}}}{\sigma_\epsilon} \frac{\partial \epsilon}{r \partial \theta} \right) + \frac{\partial}{\partial z} \left(\frac{\mu_{\text{eff}}}{\sigma_\epsilon} \frac{\partial \epsilon}{\partial z} \right) - C_1 \mu_{\text{eff}} \frac{G \epsilon}{K} + C_2 \rho \frac{\epsilon^2}{K} = 0 \end{aligned} \quad (18)$$

The thermal buoyancy has been neglected in this study since the thermal buoyancy effects are negligible when compared to density variation effects due to gaseous inflow. If ΔT is assumed to be 10°C and $\alpha = 0.05$, then for water,

$$\frac{\rho g \beta \Delta T}{\alpha \rho g} = 0.04$$

3.6 GENERAL FORM OF EQUATIONS

All equations (U, V, W, K, ε, T) can be summarized by a single transport equation of the form:

$$\frac{1}{r} \frac{\partial}{\partial r} (rV\rho\phi) + \frac{1}{r} \frac{\partial}{\partial \theta} (U\rho\phi) + \frac{\partial}{\partial z} (W\rho\phi)$$

convection terms:

$$= \frac{1}{r} \frac{\partial}{\partial r} (\Gamma_{\phi} r \frac{\partial \phi}{\partial r}) + \frac{1}{r} \frac{\partial}{\partial \theta} (\Gamma_{\phi} \frac{\partial \phi}{r \partial \theta}) + \frac{\partial}{\partial z} (\Gamma_{\phi} \frac{\partial \phi}{\partial z}) + S_{\phi} \quad (19)$$

diffusion terms source term

Table 1 Definition of ϕ , Γ_{ϕ} , and S_{ϕ} of equation (19)

Conservation of	ϕ	Γ_{ϕ}	S_{ϕ}
mass	1	0	0
momentum in axial direction	W	μ_{eff}	$\frac{\partial}{\partial z} (\mu_{\text{eff}} \frac{\partial W}{\partial z}) + \frac{1}{r} \frac{\partial}{\partial r} (r \mu_{\text{eff}} \frac{\partial V}{\partial z})$ $+ \frac{1}{r} \frac{\partial}{\partial \theta} (\mu_{\text{eff}} \frac{\partial U}{\partial z}) - \frac{\partial P}{\partial z}$
momentum in radial direction	V	μ_{eff}	$\frac{\partial}{\partial z} (\mu_{\text{eff}} \frac{\partial W}{\partial r}) + \frac{1}{r} \frac{\partial}{\partial r} (r \mu_{\text{eff}} \frac{\partial V}{\partial r})$ $+ \frac{1}{r} \frac{\partial}{\partial \theta} (r \mu_{\text{eff}} \frac{\partial U}{\partial r}) - \delta \frac{2\mu_{\text{eff}}}{r^2} \frac{\partial U}{\partial \theta}$ $- \delta \frac{2\mu_{\text{eff}}}{r^2} V + \delta \frac{U^2}{r} - \frac{\partial P}{\partial r}$

Table 1 (continued)

Conservation of	ϕ	Γ_ϕ	S_ϕ
momentum in angular direction	U	μ_{eff}	$\frac{\partial}{\partial z} \left(\frac{\mu_{\text{eff}}}{r} \frac{\partial w}{\partial \theta} \right)$ $+ \frac{1}{r} \frac{\partial}{\partial r} \left(\mu_{\text{eff}} r \left(\frac{1}{r} \frac{\partial v}{\partial \theta} - \delta \frac{U}{r} \right) \right)$ $- \delta \rho \frac{UV}{r} + \frac{\partial}{r \partial \theta} \left(\frac{\mu_{\text{eff}}}{r} \left(\frac{\partial U}{\partial \theta} + \delta 2V \right) \right)$ $+ \delta \frac{\mu_{\text{eff}}}{r} \left(\frac{\partial U}{\partial r} + \frac{\partial V}{r \partial \theta} - \frac{U}{r} \right) - \frac{\partial P}{r \partial \theta}$
energy	T	$-\frac{\mu}{\sigma} + \frac{\mu}{\sigma_t}$	S_h
kinetic energy	K	$\mu_{\text{eff}}/\sigma_K$	$G_K = \rho \epsilon C_D$
dissipation rate	ϵ	$\mu_{\text{eff}}/\sigma_\epsilon$	$\frac{\epsilon}{K} (C_1 G_K - C_2 \rho \epsilon)$

where

$$G_K = \mu_{\text{eff}} \left\{ 2 \left[\left(\frac{\partial w}{\partial z} \right)^2 + \left(\frac{\partial v}{\partial r} \right)^2 + \left(\frac{\partial U}{r \partial \theta} + \delta \frac{V}{r} \right)^2 \right] + \left(\frac{\partial w}{\partial r} + \frac{\partial V}{\partial z} \right)^2 \right.$$

$$\left. + \left(\frac{\partial U}{\partial z} + \frac{\partial w}{r \partial \theta} \right)^2 + \left(\frac{\partial v}{r \partial \theta} + \frac{\partial U}{\partial r} - \delta \frac{U}{r} \right)^2 \right\}$$

Definition of ϕ , Γ , and S_ϕ of equation (19) is summarized in Table 1. The constants in the turbulence model are assigned the values shown in Table 2 (Launder and Spalding [15]).

Table 2Constants in the Turbulence Model

C_1	C_2	C_μ	C_D	σ_K	σ_ϵ	σ_t
1.44	1.92	0.09	1.0	1.0	1.3	0.9

Assumptions for K- ϵ models [60].

a) Reynolds numbers of turbulence Re_t are assumed to be sufficiently large so that molecular transport may be neglected.

$$Re_t = \rho V' \ell / \mu = \rho K^2 / \mu \epsilon$$

b) Based on a), the small scales of turbulence which are responsible for the destruction of turbulence are assumed to be isotropic.

$$\epsilon = \nu \overline{\left(\frac{\partial u_i}{\partial x_j} \right) \left(\frac{\partial u_i}{\partial x_j} + \frac{\partial u_j}{\partial x_i} \right)}$$

If Re_t is high, viscous dissipation takes place in the smallest eddies in which distribution of energy is isotropic so that the above equation reduces to

$$\epsilon = \nu \overline{\left(\frac{\partial u_i}{\partial x_j} \right)^2}$$

3.7 TREATMENT OF NEAR-WALL REGIONS

The near-wall regions have two major characteristics that distinguish them from the central region of the flow[61]:

- a) steep non-linear gradients in flow properties, and
- b) levels of turbulence Reynolds number sufficiently low for molecular viscosity to influence the production, destruction, and diffusion of turbulence energy, so that local isotropy of small-scale turbulence no longer prevails.

Hence the basic turbulence model becomes inapplicable in these regions, and an alternative representation must be found.

Wall-function methods are commonly used. They are based on the fact that for most wall flows both mean and turbulence quantities are nearly universal functions of the dimensionless distance along a normal to the wall, y^+ is defined as

$$y^+ = \rho U_\tau y / \mu$$

Experiments show that in all steady wall flows, the thin fluid layer close to the wall can be sub-divided into three main regions based on y^+ : the viscous layer ($y^+ \leq 5$) where viscous forces dominate; followed by the

buffer layer ($5 < y^+ < 30$) which is a transition region in which the flow is neither completely dominated by viscous effects nor completely turbulent; and the inertial sublayer ($y^+ > 30$) where the flow is assumed to be completely turbulent, but sufficiently close to the wall so that the shear stress is approximately uniform.

In many engineering calculations, the buffer layer is disposed of by assuming that the viscous sublayer extends to $y^+ \approx 11.63$, beyond which point the flow is taken to be fully turbulent. This implies that the low Re_t region covers the range $0 < y^+ < 11.63$.

In this study, the wall is taken to be both smooth and impermeable. Previous works (Ideriah, [61]) have shown that the shear stress in this thin layer is uniform. Thus, from a one-dimensional analysis, assuming zero streamwise pressure gradient, the momentum equation for the flow parallel to the wall reduces to

$$v_t \frac{\partial U}{\partial y} = \tau = \frac{\tau_w}{\rho}$$

where v_t = eddy kinematic viscosity

In the wall region, distances from the wall are often measured in terms of the non-dimensional distance y^+ :

$$y^+ = \frac{U_t y}{\nu}$$

where $U_\tau = \sqrt{\frac{\tau_w}{\rho}}$

By assuming $l \propto y$ and $V' = U_\tau$

the expression $\mu_t = C_\mu \rho V' l$

becomes $\nu_t = \kappa y U_\tau$

Then the momentum equation can be written as

$$\kappa y U_\tau \frac{\partial U}{\partial y} = U_\tau^2$$

$$\kappa y \frac{1}{U_\tau} \frac{\partial U}{\partial y} = 1$$

$$\kappa y^+ \frac{\partial U^+}{\partial y^+} = 1$$

where $U^+ = \frac{U}{U_\tau}$

After integration, the momentum equation becomes

$$U^+ = \frac{1}{\kappa} \ln y^+ + \text{constant}$$

$$\text{or } U^+ = \frac{1}{\kappa} \ln(Ey^+) \quad (20)$$

The log-law constants κ and E have the numerical values of approximately 0.4 and 0.9 for a smooth wall (Launder and Spalding [15]).

FOR K EQUATION

In the inertial sublayer, both convection and diffusion

of K are negligible, thus

production rate of K = dissipation rate of K

$$\text{i.e., } -\overline{uv} \left(-\frac{\partial U}{\partial y} \right) = \epsilon$$

$$v_t \left(\frac{\partial U}{\partial y} \right)^2 = \frac{K^{3/2}}{l}$$

$$v_t^2 \left(\frac{\partial U}{\partial y} \right)^2 = C_\mu K^2$$

$$K = -C_\mu^{-1/2} \overline{uv}$$

Since shear stress is approximately uniform in the wall region ($y^+ < 200$)

$$-\overline{\rho uv} \approx \tau_w$$

$$\text{or } -\overline{\rho uv} = \rho U_\tau^2$$

$$\text{then } K = C_\mu^{-1/2} U_\tau^2 = C_\mu^{-1/2} \left(\frac{\tau_w}{\rho} \right) \quad (21)$$

WALL SHEAR STRESS (τ_w)

Since shear stress is approximately uniform in the wall region, U^+ may be approximated as

$$U^+ = \frac{U \sqrt{\tau_w \rho}}{\tau_w}$$

$$\text{where } \tau_w = -\overline{\rho uv} = \rho C_\mu^{1/2} K$$

Substitute the above expression for U^+ in equation (20), to obtain

$$\frac{U\sqrt{\tau_W \rho}}{\tau_W} = \frac{1}{\kappa} \ln(Ey^+)$$

then $\tau_W = \kappa U \sqrt{\tau_W \rho} / [\ln(Ey^+)]$

$$= \rho \kappa C_\mu^{1/4} K^{1/2} U / [\ln(Ey^+)] \quad (22)$$

FOR ϵ EQUATION

Since $\frac{\partial U}{\partial y} = \frac{U_\tau}{\kappa y}$ and $-\overline{uv} = \rho U_\tau^2$

substitute in $\epsilon = -\overline{uv} \left(-\frac{\partial U}{\partial y} \right)$

to get $\epsilon = \frac{U_\tau^3}{\kappa y}$

but $U_\tau^2 = C_\mu^{1/2} K$ then $\epsilon = C_\mu^{3/4} K^{3/2} / (\kappa y)$ (23)

FOR HEAT TRANSPORT EQUATION (SCALAR)

For one-dimensional flow in the inertial sublayer,

$$\dot{q}'' = \Gamma_t C_P \frac{\partial T}{\partial y}$$

where $\dot{q}'' =$ energy flux

dividing both sides by the wall heat flux \dot{q}_W'' , then

$$\frac{\dot{q}''}{\dot{q}_W''} = \frac{\Gamma_t}{\mu} \frac{\partial T^+}{\partial y^+}$$

where $T^+ = \frac{\rho U_\tau C_P (T_W - T)}{\dot{q}_W''}$

but, within the sublayer, $q'' = q_w''$

$$\text{also, } \frac{\Gamma_t}{\rho} = \frac{v_t}{\sigma_t} = \frac{KyU_\tau}{\sigma_t}$$

$$\text{then } \frac{\Gamma_t}{\rho} \frac{1}{v} \frac{\partial T^+}{\partial y^+} = 1$$

$$\frac{\partial T^+}{\partial y^+} = v \frac{\sigma_t}{kyU_\tau} = \frac{\sigma_t}{\kappa} \frac{v}{yU_\tau} = \frac{\sigma_t}{\kappa} \frac{1}{y^+}$$

integrating this equation gives

$$T^+ = \frac{\sigma_t}{\kappa} \ln y^+ + \text{const} \quad (24)$$

where "const" is the integration constant which is a function of the Prandtl number.

The expression for T^+ is often re-written [61], [62] as

$$T^+ = \sigma_t (U^+ + p)$$

$$\text{where } p = 9.24 \left(\frac{\sigma}{\sigma_t} \right)^{0.75}$$

Then the wall heat flux can be written as

$$q_w'' = \frac{\rho C_p (T_w - T) C_\mu^{1/4} \kappa^{1/2}}{\sigma_t \left[\frac{1}{\kappa} \ln(Ey^+) + p \right]} \quad (25)$$

3.8 OTHER BOUNDARY CONDITION

The problems investigated include the following types of boundaries:

1) Wall boundaries, where the boundary values or their fluxes are prescribed; e.g.

$$\text{at wall, } U = V = W = K = \varepsilon = \mu_{\text{eff}} = 0 ; T = T_{\text{wall}}$$

2) Entry boundaries, where the boundary values or their fluxes are prescribed; e.g.

$$U = V = 0 ; W = W_{\text{inlet}} ; K = K_{\text{inlet}} ;$$

$$\varepsilon = \varepsilon_{\text{inlet}} ; \mu_{\text{eff}} = \mu_{\text{eff, inlet}} ; T = T_{\text{inlet}}$$

3) Downstream exit boundaries, where the gradients are assumed to be zero; e.g.

$$\frac{dK}{dz} = \frac{d\varepsilon}{dz} = \frac{d\mu_{\text{eff}}}{dz} = \frac{dT}{dz} = 0$$

Applying the mass conservation equation results in:

$$[\sum W_{ij} A_{ij}]_{\text{outlet}} = [\sum W_{ij} A_{ij}]_{\text{inlet}}$$

Therefore, one can assume

$$W_{ij, \text{outlet}} = W_{ij, \text{outlet}} + \frac{1}{\sum A_{ij, \text{outlet}}} [(\sum W_{ij} A_{ij})_{\text{inlet}} - (\sum W_{ij} A_{ij})_{\text{outlet}}]$$

$$U_{\text{outlet}} = V_{\text{outlet}} = 0$$

CHAPTER 4

THE SOLUTION PROCEDURE

4.1 FORMATION OF THE FINITE-DIFFERENCE EQUATION

The transformation of the partial-differential equations into algebraic forms can be accomplished through various approaches. In this study, the "micro-integration" approach is used (Gosman et al [4]; Roache [63]).

4.1.1 THE GRID ARRANGEMENT

As shown in Fig. 2 and Fig. 3, the control volumes surround the storage locations at which the discrete values of the flow variables are located. These values represent averages over the respective control volumes. Variables ($P, T, K, \epsilon, \mu_{\text{eff}}, \rho$) are stored at the grid nodes, while the velocities U, V and W are stored mid-way between the grid nodes. Variables U, V and W are located between the pressures which drive them. Moreover, the velocities are located where they are needed for the calculation of the convective fluxes of scalar flow variables.

4.2 INTEGRATION OF THE PARTIAL DIFFERENTIAL EQUATIONS.

Using the "micro-integral" technique, the general form of equations is written as:

$$\begin{aligned} \frac{1}{r} \frac{\partial}{\partial r} (rV\rho\phi) + \frac{1}{r} \frac{\partial}{\partial \theta} (\rho U\phi) + \frac{\partial}{\partial z} (\rho W\phi) - \frac{1}{r} \frac{\partial}{\partial r} (\Gamma_\phi r \frac{\partial \phi}{\partial r}) \\ - \frac{1}{r} \frac{\partial}{\partial \theta} (\Gamma_\phi \frac{\partial \phi}{\partial \theta}) - \frac{\partial}{\partial z} (\Gamma_\phi \frac{\partial \phi}{\partial z}) - S_\phi = 0 \end{aligned} \quad (26)$$

It can be integrated over the control volume shown in Fig. 3, thus

$$\begin{aligned} \iiint_{VOL} \left\{ \frac{1}{r} \frac{\partial}{\partial r} [r(\rho V\phi - \Gamma_\phi \frac{\partial \phi}{\partial r})] + \frac{1}{r} \frac{\partial}{\partial \theta} (\rho U\phi - \Gamma_\phi \frac{\partial \phi}{r\partial \theta}) \right. \\ \left. + \frac{\partial}{\partial z} (\rho W\phi - \Gamma_\phi \frac{\partial \phi}{\partial z}) - S_\phi \right\} d(VOL) = 0 \end{aligned} \quad (27)$$

Since the Divergence theorem states that

$$\iiint_{VOL} \left(\frac{\partial}{\partial x_j} f_j \right) d(VOL) = \iint_S f_j d(A_j) \quad j = 1, 2, 3$$

f_j = component of function in direction j

A_j = area perpendicular to direction j

then equation (27) becomes

$$\begin{aligned} \iint_{nshl} \left[\underbrace{\frac{1}{r} (\rho U\phi - \Gamma_\phi \frac{\partial \phi}{r\partial \theta})}_F e - \underbrace{\frac{1}{r} (\rho U\phi - \Gamma_\phi \frac{\partial \phi}{r\partial \theta})}_F w \right] d(A_{nshl}) \\ + \iint_{ewhl} \left[\underbrace{\frac{1}{r} (r\rho V\phi - r\Gamma_\phi \frac{\partial \phi}{\partial r})}_F n - \underbrace{\frac{1}{r} (r\rho V\phi - r\Gamma_\phi \frac{\partial \phi}{\partial r})}_F s \right] d(A_{ewhl}) \\ + \iint_{nsew} \left[\underbrace{(\rho W\phi - \Gamma_\phi \frac{\partial \phi}{\partial z})}_F h - \underbrace{(\rho W\phi - \Gamma_\phi \frac{\partial \phi}{\partial z})}_F l \right] d(A_{nsew}) \\ - \iiint_{VOL} S_\phi d(VOL) = 0 \end{aligned} \quad (28)$$

4.2.1 EXPRESSIONS FOR THE FLUX TERM, F

For a steady, one-dimensional situation in which only the convective and diffusive terms are present (Ideriah [61]; Patankar [12]), the governing equation is

$$\frac{\partial}{\partial x}(\rho U \phi) = \frac{\partial}{\partial x}(\Gamma \frac{\partial \phi}{\partial x}) \quad ; \quad (29)$$

also the continuity equation becomes

$$\frac{\partial}{\partial x}(\rho U) = 0 \quad \text{or} \quad \rho U = \text{Constant}$$

The above governing equation can be solved exactly, if Γ is taken to be constant, with boundary conditions at

$$x = 0 \quad \phi = \phi_0$$

$$x = L \quad \phi = \phi_L$$

After integration, equation (29) becomes

$$\frac{\rho U}{\Gamma} x + \text{Const}_2 \frac{\rho U}{\Gamma} = \ln\left(\frac{\rho U}{\Gamma} \phi + \text{Const}_1\right)$$

$$\phi = \frac{\Gamma}{\rho U} e^{\left(\frac{\rho U}{\Gamma} x + \text{Const}_2 \frac{\rho U}{\Gamma}\right)} - \text{Const}_1 \frac{\Gamma}{\rho U}$$

By using the two boundary conditions, the exact solution can be obtained:

$$\phi = \left[\frac{\Gamma}{\rho U} e^{\left(\frac{\rho U}{\Gamma}\right)x} \right] \frac{(\phi_L - \phi_0) \frac{\rho U}{\Gamma}}{e^{\left(\frac{\rho U}{\Gamma}\right)L} - 1} + \phi_0 - \frac{\phi_L - \phi_0}{e^{\left(\frac{\rho U}{\Gamma}\right)L} - 1}$$

or

$$\frac{\phi - \phi_0}{\phi_L - \phi_0} = \frac{e^{\left(\frac{\rho U}{\Gamma}\right)x} - 1}{e^{\left(\frac{\rho U}{\Gamma}\right)L} - 1} \quad (30)$$

$$\frac{\phi - \phi_0}{\phi_L - \phi_0} = \frac{\exp[(Pe)(x/L)] - 1}{\exp(Pe) - 1} \quad (31)$$

$$\text{where } Pe = \frac{\rho UL}{\Gamma}$$

Pe is the Peclet number (ratio of the strengths of convection and diffusion).

Now consider the equation with

$$F_e = \iint (\rho U \phi - \Gamma \frac{\partial \phi}{\partial x})_e dA_e \quad (32)$$

The exact solution above can be used as a profile between points p and E, which replace ϕ_0 & ϕ_L ; the distance $(\delta x)_e$ then replaces L; i.e.,

$$\frac{\phi - \phi_p}{\phi_E - \phi_p} = \frac{\exp(Pe)[x/(\delta x)_e] - 1}{\exp(Pe) - 1} \quad (33)$$

$$\text{where } Pe = (\rho U)_e (\delta x)_e / \Gamma_e$$

The derivative of ϕ with respect to x is

$$\frac{d\phi}{dx} = (\phi_E - \phi_p) \frac{Pe}{(\delta x)_e} \frac{e^{(Pe)[x/(\delta x)_e]}}{e^{Pe} - 1} \quad (34)$$

Substituting equations (33) and (34) into equation (32) yields

$$F_e = \left[\frac{(\rho U)_e (\phi_p - \phi_E)}{\exp(Pe) - 1} + (\rho U)_e \phi_p \right] A_e \quad (35)$$

$$\text{or } F_e = (\rho U)_e A_e [(1 + f_e)\phi_p - f_e\phi_E]$$

$$\text{where } f_e = 1 / [\exp(Pe) - 1]$$

Next, the total flux term F_e is expressed in terms of the nodal values for the variables. For the east boundary,

$$F_e = \rho_e U_e A_e [(1 + f_e)\phi_p - f_e\phi_E] \quad (36)$$

$$\text{where } f_e = 1 / [\exp(Pe_e) - 1]$$

$$Pe_e = \rho_e U_e (\delta x)_{pE} / \Gamma_e$$

$$\rho_e = (\rho_E + \rho_p) / 2$$

$$\Gamma_e = (\Gamma_E + \Gamma_p) / 2$$

$$A_e = \delta_{ns} \delta_{hl}$$

Since

$$\frac{e^x}{e^x - 1} = 1 + \frac{1}{e^x - 1} = 1 + \frac{1}{x} \left(\frac{x}{e^x - 1} \right)$$

and

$$\frac{x}{e^x - 1} = 1 - \frac{1}{2}x + \sum_{n=1}^{\infty} (-1)^{n+1} \frac{B_n x^{2n}}{(2n)!} \quad \text{for } -\infty < x < \infty$$

where B_n = Bernoulli numbers.

$$\begin{array}{lll} \text{e.g. } B_1 = \frac{1}{6} & B_2 = \frac{1}{30} & B_3 = \frac{1}{42} \\ B_4 = \frac{1}{30} & B_5 = \frac{5}{66} & B_6 = \frac{691}{2730} \quad \text{etc.} \end{array}$$

$$\begin{aligned}
 \text{then } \frac{e^x}{e^x - 1} &= 1 + \frac{1}{x} \left[1 - \frac{1}{2}x + \sum_{n=1}^{\infty} \frac{(-1)^{n+1} B_n x^{2n}}{(2n)!} \right] \\
 &= 1 + \frac{1}{x} - \frac{1}{2} + \frac{1}{x} \sum_{n=1}^{\infty} \frac{(-1)^{n+1} B_n x^{2n}}{(2n)!} \\
 &= \frac{1}{2} \left(1 + \frac{2}{x} \right) + \underbrace{\frac{1}{12}x - \frac{1}{720}x^3 + \dots}_{\text{negligible}}
 \end{aligned}$$

$$\text{Thus } \frac{1}{e^x - 1} \approx \frac{1}{x} - \frac{1}{2}$$

$$\text{and } f_e = \frac{1}{e^{Pe} - 1} \approx \frac{1}{Pe} - \frac{1}{2} \quad (37)$$

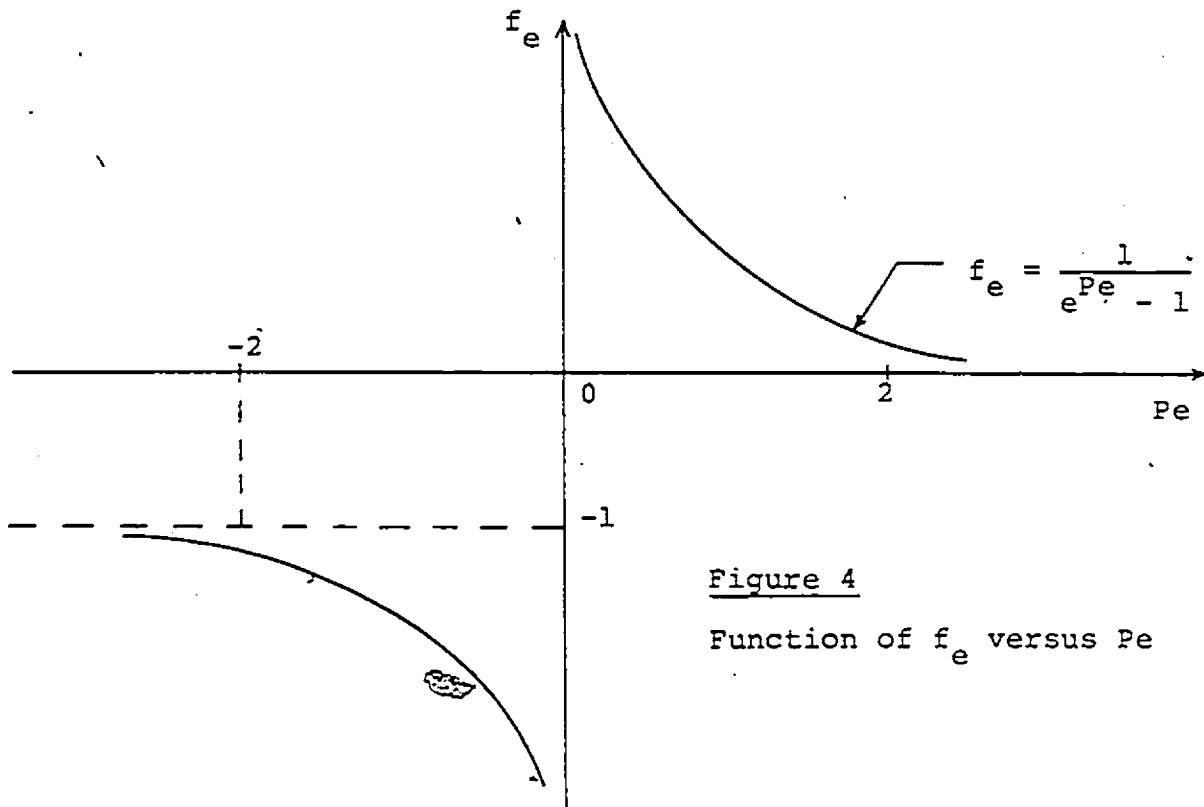


Figure 4

Function of f_e versus Pe

The validity of equation (37) is then examined.

In Fig. 4, if $(Pe)_e > 2$ $f_e = 0$

$$(Pe)_e < -2 \quad f_e = -1$$

$$|(Pe)_e| < 2 \quad f_e = \frac{1}{Pe} - \frac{1}{2}$$

$$\text{Let } a_e = \rho_e U_e A_e f_e$$

$$C_e = \rho_e U_e A_e$$

$$D_e = \Gamma_e A_e / \delta x_{pE}$$

$$(Pe)_e = C_e / D_e$$

then equation (36) becomes $F_e = a_e (\phi_p - \phi_E) + C_e \phi_p$

$$\text{where } a_e = \begin{cases} D_e - \frac{1}{2} C_e & |\frac{1}{2} C_e| < D_e \\ 0 & \frac{1}{2} C_e > D_e \\ -C_e & \frac{1}{2} C_e < -D_e \end{cases}$$

$$\text{or } a_e = \max(|\frac{1}{2} C_e|, D_e) - \frac{1}{2} C_e$$

(38.a)

This procedure represents the hybrid-central difference numerical scheme (See Patankar & Spalding [1]; Ideriah [61]; Patankar [12]).

Similarly, by following the above procedure, expressions for F_w, F_n, F_s, F_h, F_l can be derived; e.g.

for F_w , the boundary conditions for equation (29)

can be replaced by:

$$\phi_0 = \phi_w, \quad \phi_L = \phi_p$$

the resulting flux term can be obtained:

$$F_w = \rho_w U_w A_w [f_w \phi_w + (1 - f_w) \phi_p] \quad (38.b)$$

$$\text{where } f_w = \frac{\exp(\text{Pe}_w)}{\exp(\text{Pe}_w) - 1} \quad \text{Pe}_w = \frac{\rho_w U_w \delta x_{pw}}{\Gamma_w}$$

$$\text{or } F_w = a_w (\phi_w - \phi_p) + C_w \phi_p$$

$$a_w = \max\left(\left|\frac{1}{2} C_w\right|, D_w\right) + \frac{1}{2} C_w$$

$$\text{also } F_n = a_n (\phi_p - \phi_n) + C_n \phi_p$$

$$F_s = a_s (\phi_s - \phi_p) + C_s \phi_p$$

$$F_h = a_h (\phi_p - \phi_h) + C_h \phi_p$$

$$F_l = a_l (\phi_L - \phi_p) + C_l \phi_p \quad (38.c)$$

$$a_n = \max\left(\left|\frac{1}{2} C_n\right|, D_n\right) - \frac{1}{2} C_n$$

$$a_s = \max\left(\left|\frac{1}{2} C_s\right|, D_s\right) + \frac{1}{2} C_s$$

$$a_h = \max\left(\left|\frac{1}{2} C_h\right|, D_h\right) - \frac{1}{2} C_h$$

$$a_l = \max\left(\left|\frac{1}{2} C_l\right|, D_l\right) + \frac{1}{2} C_l$$

Then by substituting the above equations into the conservation equation for the control volume; i.e.

$$F_e - F_w + F_n - F_s + F_h - F_l = \iiint_{\text{VOL}} S_\phi \, d(\text{VOL})$$

yields:
$$\phi_p [(a_e + a_w + a_n + a_s + a_h + a_l) + (C_e - C_w + C_n - C_s + C_h - C_l)] - (a_e \phi_E + a_w \phi_W + a_n \phi_N + a_s \phi_S + a_h \phi_H + a_l \phi_L) - \iiint_{VOL} S_\phi d(VOL) = 0 \quad (39)$$

In a control volume, $C_e + C_w + C_n + C_s + C_h + C_l = 0$

to fulfill continuity conditions.

Then
$$\sum_i a_i \phi_i - \phi_p \sum_i a_i + \iiint_{VOL} S_\phi d(VOL) = 0 \quad (40)$$

where $i = n, s, e, w, h, l$

4.2.2 EXPRESSIONS FOR THE SOURCE TERM

In the general form of equations, there are source terms for all variables (i.e., U, V, W, K, ε, T). They can be put in the form

$$\iiint_{VOL} S_\phi d(VOL) = Sp(\phi_p) + Su \quad (41)$$

For U

$$Sp = - \delta \frac{\mu_{eff}}{r^2}$$

$$\begin{aligned} Su = & P \Big|_e^w \Delta r \Delta z + \frac{1}{r} (\mu_{eff} \frac{1}{r} \frac{\Delta U}{\Delta \theta} - \delta \frac{2\mu_{eff}}{r} V) \Big|_w^e \frac{VOL}{\Delta \theta} + \frac{1}{r} (\mu_{eff} \frac{\Delta V}{\Delta \theta} \\ & - \delta U \mu_{eff}) \Big|_s^n \frac{VOL}{\Delta r} + \frac{1}{r} (\mu_{eff} \frac{\Delta W}{\Delta \theta}) \Big|_l^h \frac{VOL}{\Delta z} + \delta [(\frac{\mu_{eff}}{r} \frac{\Delta U}{\Delta r}) \Big|_s^n \\ & + (\frac{\mu_{eff}}{r^2} \frac{\Delta V}{\Delta \theta}) \Big|_w^e - \frac{\rho UV}{r}] \end{aligned} \quad (42)$$

For V

$$S_p = - \delta \frac{2\mu_{\text{eff}}}{r^2}$$

$$\begin{aligned} S_u = P & \left| \frac{s}{n} \Delta\theta \Delta z + \frac{1}{r} (\mu_{\text{eff}} r \frac{\Delta V}{\Delta r}) \right| \frac{n}{s} \frac{\text{VOL}}{\Delta r} + \frac{1}{r} (\mu_{\text{eff}} \frac{\Delta U}{\Delta r}) \left| \frac{e}{w} \frac{\text{VOL}}{\Delta\theta} \right. \\ & + (\mu_{\text{eff}} \frac{\Delta W}{\Delta r}) \left| \frac{h}{l} \frac{\text{VOL}}{\Delta z} + \delta \left[\frac{\rho U^2}{r} - 2 \left(\frac{\mu_{\text{eff}}}{r^2} \frac{\Delta U}{\Delta\theta} \right) \right] \frac{e}{w} \right. \\ & \left. - \frac{1}{r} \left(\frac{\mu_{\text{eff}}}{r} \frac{\Delta U}{\Delta\theta} \right) \right| \frac{e}{w} \end{aligned} \quad (43)$$

For W

$$S_p = 0$$

$$\begin{aligned} S_u = P & \left| \frac{l}{h} \Delta\theta \Delta r + (\mu_{\text{eff}} \frac{\Delta W}{\Delta z}) \right| \frac{h}{l} \frac{\text{VOL}}{\Delta z} + \frac{1}{r} (\mu_{\text{eff}} \frac{\Delta U}{\Delta z}) \left| \frac{e}{w} \frac{\text{VOL}}{\Delta\theta} \right. \\ & \left. + \frac{1}{r} (\mu_{\text{eff}} r \frac{\Delta V}{\Delta z}) \right| \frac{n}{s} \frac{\text{VOL}}{\Delta r} \end{aligned} \quad (44)$$

For K

$$S_p = - \frac{C_\mu C_D \rho^2 K_p (\text{VOL})}{\mu_t} \quad (45)$$

$$S_u = \mu_t G (\text{VOL})$$

For ε

$$S_p = - C_2 \frac{\rho \epsilon_p}{K_p} (\text{VOL}) \quad (46)$$

$$S_u = C_1 \frac{\mu_t G \epsilon_p}{K_p} (\text{VOL})$$

For T

$$S_p = 0$$

$$S_u = 0$$

Then, the integrated transport equations become

$$\sum_i a_i \phi_i - \phi_p \sum_i a_i + S_p \phi_p + S_u = 0$$

$$\text{or } \phi_p (\sum_i a_i - S_p) = \sum_i a_i \phi_i + S_u \quad (47)$$

4.3 THE SOLUTION OF THE FINITE-DIFFERENCE EQUATION

4.3.1 INTRODUCTION

The solution procedure used in this study was the "guess-correct" procedure. Since the equations are non-linear and inter-linked, the algebraic equations of all variables were solved simultaneously. The line iteration method was used and was carried out by sweeping through all three directions. Values of the previous iteration were used as the new "guess" values until the solution converged. The solution procedure was developed based on the SIMPLE algorithm of Patankar and Spalding [1].

4.3.2 THE ITERATION METHOD

A grid line is chosen (e.g. in the y-direction) while the neighboring lines (i.e., in the x- and z-direction) are known from their values of the previous iteration. The ϕ values in the chosen line can be solved by the Tridiagonal Matrix Algorithm (TDMA, see Appendix B). Then the procedure is repeated in one sweep for all lines in the y-direction. One or more sweeps in other directions (i.e., x- and z-direction) could follow, if desired.

The convergence of the line iteration method is fast, because the information from the end boundaries of the line is transmitted at once to the interior of the domain. By alternating the line directions, one can quickly bring the information from all boundaries to the interior.

4.4 THE PRESSURE CORRECTION EQUATION

The steady-state continuity equation is given as

$$\frac{1}{r} \frac{\partial}{\partial r}(r\rho V) + \frac{1}{r} \frac{\partial}{\partial \theta}(\rho U) + \frac{\partial}{\partial z}(\rho W) = 0 \quad (48)$$

The integration of the continuity equation for the typical control volume shown in Fig. 2 gives

$$\begin{aligned} \frac{1}{r}(\rho UA)_e - \frac{1}{r}(\rho UA)_w + \frac{1}{r}(r\rho VA)_n - \frac{1}{r}(r\rho VA)_s + (\rho WA)_h \\ - (\rho WA)_l = 0 \end{aligned} \quad (49)$$

If p^* is the guessed pressure, then the correct pressure is obtained from $p = p^* + p'$ where p' is the pressure correction.

Consider the x-momentum algebraic equation,

$$\left(\sum_i a_i - Sp\right)U_e = \sum_i a_i U_i + b + (P_p - P_E)A_e \quad (50)$$

Now, using the guess values, P^* , U^* , V^* , W^*

$$\left(\sum_i a_i - Sp\right)U_e^* = \sum_i a_i U_i^* + b + (P_p^* - P_E^*)A_e \quad (51)$$

Subtract equation (51) from (50) to yield

$$\left(\sum_i a_i - Sp\right)(U_e - U_e^*) = \sum_i a_i (U_i - U_i^*) + (P_p' - P_E')A_e \quad (52)$$

assuming $U_i = U_i^*$ and $U_e = U_e^* + U_e'$

$$\text{Then, } \left(\sum_i a_i - Sp\right)U_e' = (P_p' - P_E')A_e$$

$$\text{or } U_e = U_e^* + d_e(P_p' - P_E') \quad (53)$$

$$\text{where } d_e = A_e / \left(\sum_i a_i - Sp\right)$$

Equation (53) is called the velocity-correction formula for U_e . Other formulas are :

$$U_w = U_w^* + d_w(P_w' - P_p')$$

$$U_n = U_n^* + d_n (P_p' - P_N')$$

$$U_s = U_s^* + d_s (P_s' - P_p')$$

$$U_h = U_h^* + d_h (P_p' - P_H')$$

$$U_l = U_l^* + d_l (P_L' - P_p')$$

Substituting all the velocity correction formulas in equation (49) yields

$$\left(\sum_i a_i \right) P_p' = \sum_i a_i P_i' + C \quad (55)$$

$$\text{where } a_E = \rho_e d_e A_e$$

$$a_W = \rho_w d_w A_w$$

$$a_N = \rho_n d_n A_n$$

$$a_S = \rho_s d_s A_s$$

$$a_H = \rho_h d_h A_h$$

$$a_L = \rho_l d_l A_l$$

$$C = (\rho U^* A)_W - (\rho U^* A)_E + (\rho V^* A)_S - (\rho V^* A)_N + (\rho W^* A)_L - (\rho W^* A)_H \quad (56)$$

Note that for the pressure-correction equation (55), the source term $S_u = C$; $S_p = 0$

4.5 THE 'SIMPLE' ALGORITHM

The procedure used to solve the pressure-linked momentum equations is the SIMPLE algorithm which stands for Semi-Implicit Method for Pressure-Linked Equations. The important steps in the operation are:

- 1) ~~Guess~~ the pressure field P^*
- 2) Solve the momentum equations to obtain U^* , V^* , W^*
- 3) Solve the P' (pressure correction) equation
- 4) Update the pressure (P) by adding P' to P
- 5) Update U , V , W from their guessed values using the velocity-correction formulas (see Section 4.4)
- 6) Solve other ϕ equations (e.g., temperature, K , ϵ)
- 7) Calculate new fluid and turbulence properties (e.g., ρ , μ_{eff})
- 8) Use the new corrected pressure as a newly guessed pressure P^* , return to Step 2, and repeat the whole procedure until a converged solution has been achieved.

4.6 NUMERICAL STABILITY

4.6.1 UNDERRELAXATION

Underrelaxation is used to avoid divergence in the iteration solution of strongly nonlinear equations. It slows down the changes of the solution from iteration to iteration. For the x-momentum equation,

$$(\sum_i a_i - Sp)U_p = \sum_i a_i U_i + Su \quad (57)$$

$$U_p = \frac{\sum_i a_i U_i + Su}{\sum_i a_i - Sp} \quad (58)$$

Manipulating equation (58), yields

$$U_p = U_p^* + \left(\frac{\sum_i a_i U_i + Su}{\sum_i a_i - Sp} - U_p^* \right)$$

where the contents of the parentheses represent the change in U_p produced by the current iteration. This change can be reduced by the introduction of a relaxation factor γ , so that

$$U_p = U_p^* + \gamma \left(\frac{\sum_i a_i U_i + Su}{\sum_i a_i - Sp} - U_p^* \right)$$

$$\text{or } \frac{(\sum_i a_i - Sp)}{\gamma} U_p = \sum_i a_i U_i + Su + (1 - \gamma) \frac{(\sum_i a_i - Sp)}{\gamma} U_p^* \quad (59)$$

When the solution converges after a number of iterations, U_p becomes equal to U_p^* . This implies that the converged

values of U_p do satisfy the original equations.

4.6.2 FALSE SOURCE TERM

As described by Patankar [12], there are two rules concerning the values of the coefficients in equation (47); i.e.,

$$(\sum_i a_i - Sp) \phi_p = \sum_i (a_i \phi_i) + Su$$

where $i = n, s, e, w, h, \ell$

The rules are

- (i) All coefficients $(\sum_i a_i - Sp$ and neighbouring coefficients $a_i)$ must always be positive,
- (ii) When the source term is linearized as $S = Su + Sp\phi_p$, the coefficient Sp must always be less than or equal to zero.

By examining the equations in Section 4.2.1 and 4.2.2, it can be seen that the coefficients (a_i) are always greater than or equal to zero and Sp is always smaller than or equal to zero.

However, numerical instability may arise when all the coefficients $(a_i$ and $Sp)$ are zero. Under this condition, the tridiagonal matrix (see Appendix B) would become singular, since $\sum_i a_i - Sp = 0$ in equation (47).

Therefore, a false mass source is introduced, such that

$$-\iiint_{VOL} S_{false} d(VOL) = (S_p)_f \phi_p + (Su)_f \quad (60)$$

where

$$(Sp)_f = - \sum_i C_i$$

$$(Su)_f = (\sum_i C_i) \phi_p^*$$

$$\sum_i C_i = \max(0.0, \rho_n V_n A_n - \rho_s V_s A_s + \rho_e U_e A_e - \rho_w U_w A_w + \rho_h W_h A_h - \rho_l W_l A_l)$$

Then the general algebraic equation (47) becomes

$$[\sum_i a_i - Sp - (Sp)_f] \phi_p = \sum_i a_i \phi_i + Su + (Su)_f \quad (61)$$

In this way, the case of all coefficients being zero can be eliminated. Also, the false source terms have no effect on the final solution, since $\phi_p^* = \phi_p$ and $\sum_i C_i = 0$, when that solution is obtained.

4.6.3 CONVERGENCE

In the SIMPLE algorithm, convergence is considered achieved when the total divergence (R_ϕ) is less than a chosen value, for all equations. Total divergence is defined as

$$R_\phi = \frac{\sum_{\text{all } i, j, k} (\text{convection} + \text{diffusion} + \text{source})}{J_{\phi_{\text{reference}}}}$$

$$R_\phi = \frac{\sum_{\text{all } i, j, k} \left| (\sum_m a_m - Sp)\phi - \sum_m (a_m \phi_m) - Su \right|}{J_{\phi_{\text{reference}}}} \quad (62)$$

where $m = n, s, e, w, h, \ell$

$J_{\phi \text{ reference}}$ is the reference flux for variable ϕ .

e.g. $J_{\phi \text{ reference}} = \sum_{\text{inlet}} \rho W A$

4.7 COMPUTATIONAL METHODS FOR THE GAS-AGITATED LADLE

This section describes the methods of computation associated with the ladle predictions. The physical models for both centered and off-centered gas-stirred ladles are also described. The assumptions made with respect to the gas-liquid interaction are presented and the initial[†] and boundary conditions are listed. Some comments on the development of the three-dimensional computer program are made.

4.7.1 DESCRIPTION OF THE PHYSICAL MODEL FOR BOTH CENTERED AND OFF-CENTERED, GAS-STIRRED LADLES

A schematic diagram to show the ladle arrangement in the metallurgical process is shown in Fig. 5a. The ladle is assumed to have a cylindrical shape. For centered-jetting, the gas plug is located at the center of the bottom plate as shown in Fig. 5b. For off-centered jetting, the gas plug is located on the bottom plate half-way between the center line

† "Initial condition" is used in the present work for the assignment of the parameter value at the start of the computation.

and the side wall as shown in Fig. 5c. Argon gas is injected through a submerged lance, plug, or nozzle to stir the liquid metal in the ladle. The gas flow induces motion in the fluid, thus enhancing chemical reactions and minimizing temperature heterogeneities. A gas-liquid mixture column with cylindrical shape and a radius of R_c is assumed. The walls are assumed to be rigid and impermeable. The top surface is assumed to be a free surface. The molten steel level in the ladle remains the same during the gas-stirred process.

Computations were carried out for different geometries and gas flow rates for both laboratory and industrial scales. The physical and thermal properties for the three distinct ladles that are analyzed in this study are listed in Table 3. The properties listed for vessel 1 are those adopted by Deb Roy et al, which are also identical to the conditions described in Szekely's experiments [54]. The conditions listed for vessel 2 shown in Table 3 are identical to those described in Guthrie's experiments [64]. Vessel 1 and vessel 2 are water models which are used to examine the behavior of the mathematical model developed. Vessel 3 is a 150-ton steel ladle in which the flow pattern in the full-scaled ladle can be analyzed.

Table 3 Physical and thermal properties data for the three vessels studied

	<u>Vessel #1</u>	<u>Vessel #2</u>	<u>Vessel #3</u>
diameter (m)	0.6	0.5	3.0
depth of fluid (m)	0.6	0.45	2.7
gas flow rate (m ³ /s)	2.052×10^{-4}	4.30×10^{-4}	5.937×10^{-2}
nozzle diameter (mm)	12.7	2.16	13
liquid	water	water	steel
liquid density (kg/m ³)	995	995	7,500
μ_{lam} (kg/m-s)	0.655×10^{-3}	0.655×10^{-3}	5.0×10^{-3}
Pr	4.34	4.34	0.089

4.7.2 ASSUMPTIONS MADE FOR THE BUOYANCY CALCULATION

To evaluate the density variation in the two-phase region, void fractions are calculated for both non-slip and slip-conditions. The term "slip" can be defined as slipping between the gas bubbles and their surrounding fluid. For non-slip conditions, the general expression to evaluate the void fraction (α) is:

$$\alpha = \frac{V_g}{\int_0^A W \, dA}$$

When slip is considered between the phases, the following expression is used:

$$\alpha = \frac{V_g}{\int_0^A (W + W_{\text{slip}}) \, dA}$$

W_{slip} is the relative velocity between the gas phase and the liquid phase. The slip ratio ($W_{\text{gas}}/W_{\text{liquid}}$) is generally determined from empirical correlations for two-phase flow since it depends on the flow pattern, pressure, voids, etc.. In this work, a slip velocity (W_{slip}) of 0.4 m/s is assumed. The calculation of the void in the mixture column in a given cell is carried out in two different ways based on the following assumptions:

1. An average void fraction is calculated for a horizontal plane with the expression:

$$\bar{\alpha}(z) = \frac{V_g}{\int_0^{2\pi} \int_0^{R_c} r W(z) dr d\theta}$$

This void fraction is used in the computation for all cells in the mixture column of that particular horizontal plane.

2. A local void fraction is calculated for each cell in the mixture column with the expression:

$$\alpha(\theta, r, z) = \frac{\Delta V_g(\theta, r)}{r W(\theta, r, z) \Delta r \Delta \theta}$$

This expression is based on the assumption of uniform distribution of the gas flow in the mixture column.

In the gas-liquid mixture column, the local density is estimated as

$$\rho(\theta, r, z) = [1 - \alpha(\theta, r, z)]\rho_{liq} + \alpha(\theta, r, z)\rho_g \quad r < R_c$$

Since $\rho_g \ll \rho_{liq}$ and α is generally small (e.g. $\alpha < 0.2$),

one may assume that

$$\rho(\theta, r, z) = [1 - \alpha(\theta, r, z)]\rho_{liq} \quad r < R_c$$

Deb Roy et al (1978) suggested a value of 0.24 for the ratio of R_c/R . The value of R_c/R depends on the gas flow rate, pressure, flow pattern, etc.. In this study, a value of 0.25 is chosen for R_c/R to allow for comparison of the present data with former results.

4.7.3 INITIAL AND BOUNDARY CONDITIONS

The initial conditions at the beginning of the computation and the boundary conditions imposed are:

(i) Initial conditions

The fluid velocities and all the turbulence parameters of the flow in the ladle are initially prescribed as follows:

$$U(\theta, r, z) = V(\theta, r, z) = W(\theta, r, z) = 0$$

$$K(\theta, r, z) = K_{\text{initial}} = 0.05 (W_{\text{initial}})^2$$

$$\epsilon(\theta, r, z) = \epsilon_{\text{initial}} = C_{D..} (K_{\text{initial}})^{3/2} / (0.01 R)$$

$$\mu_{\text{eff}}(\theta, r, z) = \mu_{\text{lam}} + C_{\mu} \rho (K_{\text{initial}})^2 / \epsilon_{\text{initial}}$$

$$T(\theta, r, z) = T_{\text{initial}}(z)$$

$$\rho(\theta, r, z) = \rho_{\text{liq}} \quad r \leq R_c$$

$$\rho(\theta, r, z) = (1 - \alpha)\rho_{\text{liq}} + \alpha\rho_g \quad r < R_c$$

The fluid in the ladle is initially stratified with a higher temperature at the top. For the non-slip condition, the initial axial velocities (W) in the mixture column are assigned a small positive value to avoid dividing V_g by zero at the beginning of the computation.

(ii) Boundary conditions at the walls

The fluid velocities and turbulence parameters at the fictitious wall cells are prescribed as:

$$W = V = K = \epsilon = \mu_{\text{eff}} = \rho = 0$$

$$\frac{dT}{dx_j} = 0 \quad (\text{no temperature gradient at walls})$$

(iii) Boundary conditions at the free surface

The fluid velocities and turbulence parameters at the fictitious free surface cells are prescribed as:

$$W = 0$$

$$\frac{dU}{dz} = \frac{dV}{dz} = \frac{dK}{dz} = \frac{d\varepsilon}{dz} = \frac{dT}{dz} = \frac{d\mu_{\text{eff}}}{dz} = 0$$

(no shear is transmitted through the free surface)

(iv) Treatment of near-wall regions

In the near-wall region, the wall-function method is employed as described in Section 3.7. Both the mean and the turbulence quantities are expressed as a function of the dimensionless distance (y^+) normal to the wall. In the near-wall region, both convection and diffusion of the turbulence kinetic energy are negligible and therefore, the production rate of the turbulence kinetic energy is equal to its dissipation rate.

(v) Boundary conditions in angular direction

At the θ -boundary, the conditions are as follows:

$$\phi(1, r, z) = \phi(NX-1, r, z)$$

$$\phi(NX, r, z) = \phi(2, r, z)$$

where $\phi = U, V, W, K, \varepsilon, T, \rho, \mu_{\text{eff}}$

The grid cells $(1, r, z)$ and (NX, r, z) are fictitious boundary cells.

4.7.4 PROGRAMMING DETAILS OF FLOW PREDICTIONS IN A LADLE

The computer program developed has over 8,000 lines. In the computer program, a three-dimensional, cylindrical coordinate system (θ, r, z) was used as well as a coarse uniform grid of $12 \times 10 \times 10$ in the z -, r - and θ -direction. A memory region of 350K was taken up to compile this program. To achieve convergence, about 100 iterations were executed.

4.8 COMPUTATIONAL METHODS FOR THE PHYSICAL MODEL OF THE T-SHAPED TUNDISH

The physical model of the T-shaped tundish is described in this section. The initial and boundary conditions applied to the model are stated. Computational details with respect to the execution of the computer program are also discussed.

4.8.1 DESCRIPTION OF THE PHYSICAL MODEL OF THE T-SHAPED TUNDISH

A schematic diagram of the water model used to predict the flow in the T-shaped tundish, is shown in Fig. 6. Since the flow is symmetrical, only half of the tundish is modelled, as shown in Fig. 7. To simplify the analysis, both the inlet and the outlet nozzles are assumed to be rectangular in shape and identical in size. Velocity gradients at the nozzles are zero. The walls are assumed to be rigid and impermeable.

The constant wall temperatures are lower than the inlet fluid temperature by 10°C. The top surface is assumed to be a free surface. The fluid depth in the tundish is constant since the inlet flow rate is equal to the outlet flow rate.

The physical and thermal properties of the water model which simulates the flow in the T-shaped tundish, are shown in Table 4. The properties listed are similar to those adopted by Heaslip [65]. A similar experimental water model has also been built by Guthrie et al to study the flow in the T-shaped tundish. However, the experimental data available for the comparison of the behavior between the experimental water models and the present mathematical model, are limited.

4.8.2 INITIAL AND BOUNDARY CONDITIONS

The initial and boundary conditions are:-

(i) Initial conditions

The fluid velocities and all turbulence parameters of the flow in the tundish are initially prescribed as follows:

$$W \text{ (at inlet nozzle)} = 0.5 \text{ m/s}$$

$$W \text{ (at outlet nozzle)} = 0.25 \text{ m/s}$$

$$W \text{ (otherwise)} = U(x,y,z) = V(x,y,z) = 0$$

$$K(x,y,z) = K_{\text{initial}} = 0.05 (W_{\text{inlet}})^2$$

$$\epsilon(x,y,z) = \epsilon_{\text{initial}} = C_D (K_{\text{initial}})^{3/2} / (0.01 R)$$

Table 4 Physical and thermal properties data for
the T-shaped tundish (refer to Fig. 6)

<u>Property</u>	<u>Data</u>
length	0.48 m
width	0.32 m
depth	0.15 m
nozzle size	0.02 m × 0.02 m
inlet flow velocity	0.5 m/s
fluid	liquid water
fluid density	995 kg/m ³
μ_{lam}	0.655×10^{-3} kg/m-s
Pr	4.34
T_{inlet}	310°C
T_{wall}	300°C

$$\mu_{\text{eff}}(x,y,z) = \mu_{\text{lam}} + C_{\mu} \rho (K_{\text{initial}})^2 / \epsilon_{\text{initial}}$$

$$T(x,y,z) = T_{\text{wall}}$$

$$\rho(x,y,z) = \rho_{\text{liq}}$$

The fluid in the tundish is assumed to be initially at a constant temperature equal to the wall temperature. Since the total inlet area is only half of the total outlet area, the outlet velocity is prescribed as half of the inlet velocity. The fluid density is kept constant for all nodes.

(ii) Boundary conditions at the walls

The fluid velocities and all turbulence parameters at the fictitious wall cells are prescribed as:

$$W = V = U = K = \epsilon = \mu_{\text{eff}} = \rho = 0$$

$$T = T_{\text{wall}}$$

(iii) Boundary conditions at the free surface

The fluid velocities (U and V) and all the turbulence parameters at the fictitious free surface cells are prescribed as:

$$W = 0$$

$$\frac{dU}{dz} = \frac{dV}{dz} = \frac{dK}{dz} = \frac{d\epsilon}{dz} = \frac{dT}{dz} = \frac{d\mu_{\text{eff}}}{dz} = 0$$

(no shear is transmitted through the free surface)

(iv) Treatment of near wall regions

In the near-wall region, the wall-function method is employed as described in Section 3.7 and Section 4.7.3 (iv).

(v) Boundary conditions at the nozzles

At the nozzles,

$$W_{\text{inlet}} = 0.5 \text{ m/s}$$

$$W_{\text{outlet}} = \frac{1}{2} W_{\text{inlet}}$$

$$U = V = 0$$

$$\frac{dK}{dz} = \frac{d\epsilon}{dz} = \frac{dT}{dz} = \frac{du_{\text{eff}}}{dz} = 0$$

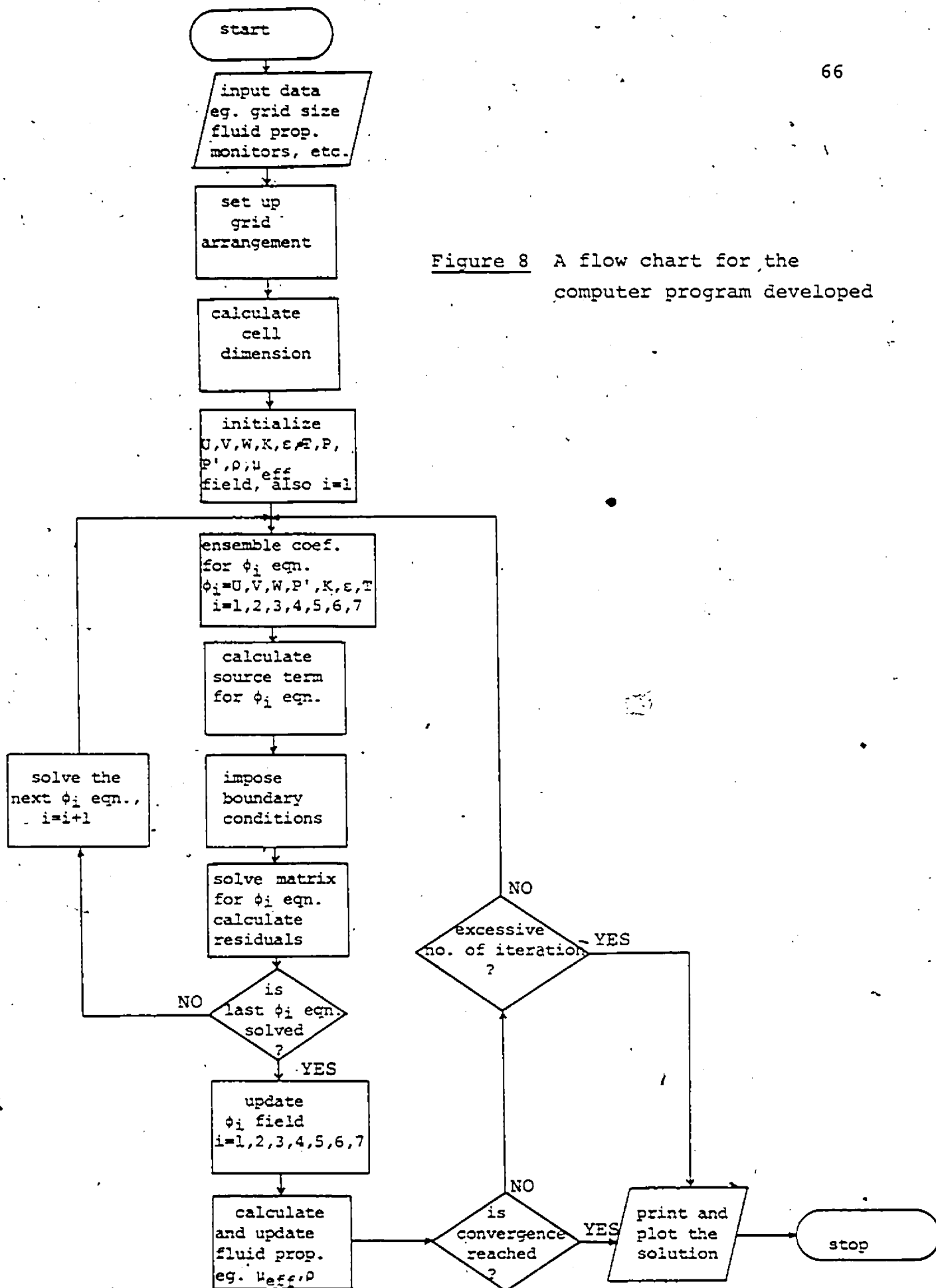
4.8.3 PROGRAMMING DETAILS OF FLOW PREDICTIONS IN A TUNDISH.

Various computational details required for the flow predictions in the tundish which are different from the flow predictions in the ladle are explained here. The grid arrangement is similar to that for the flow prediction in the ladle, except that the Cartesian coordinates (x,y,z) are used rather than the cylindrical coordinates. A variable grid of $20 \times 26 \times 12$ is used in x-, y- and z-direction. A memory region of 1000K was taken up to compile the program. To achieve convergence, about 200 iterations were executed.

4.9 SUMMARY OF THE COMPUTER PROGRAM

A flow chart of the computational procedure for the three-dimensional model developed is shown in Fig. 8. The detailed steps of the computation are as follows:

- (1) Information such as the grid size, ladle or tundish dimensions, fluid properties (i.e. μ_{lam} , μ_{liq} , Prandtl numbers etc.), control parameters, type of coordinate system used, etc. is input through block data.
- (2) The grid arrangement is then set up with the given grid size. A variable mesh size or a uniform mesh size can be specified, and the corresponding weight factor is calculated.
- (3) The cell dimensions, cell areas and cell volumes for the U-cells, V-cells, W-cells and grid cells are calculated.
- (4) The ϕ variable fields ($\phi = U, V, W, K, \epsilon, T, \rho, \mu_{eff}$) are initialized.
- (5) For the U-momentum equation, the following procedure is followed. The coefficients, a_i , are set up for all cells in the domain. Subsequently, the source terms, S_u, S_p are calculated. Special boundary conditions are imposed for the wall, the symmetry line and the free



surface. The set of algebraic equations at the different grid nodes, constitutes a system of simultaneous algebraic equations, the solution of which is obtained by performing successive line-iterations in the three coordinate directions. The algebraic equations at all U-cells along a given U-cell line are solved simultaneously for the values along that line, while the neighbouring values along the other U-cells lines are fixed at their previous iteration values. Along the line in the z-, r- and θ -direction, the set of algebraic equations yields a tridiagonal matrix of coefficients, the solution of which is obtained rapidly by means of the tridiagonal matrix algorithm (see Appendix B).

- (6) Other variables (i.e. V, W, P', K, ϵ, T) are solved successively with the same procedure described in Step 5. The sequence of solution for these variables is chosen according to their relative influence on each other.
- (7) Values of the variables $U, V, W, P', K, \epsilon, T$ for the current iteration are updated.
- (8) Fluid properties (i.e. $\alpha, \rho, \mu_{\text{eff}}$) are calculated and updated based on the updated, dependent variables.
- (9) The results are printed after a desired number of iterations. The velocity profiles, K-distribution, and length

scale distribution are plotted for different, chosen planes. The iteration procedure continues, with a new iteration being initiated and the procedure from Step 5 to Step 9 being repeated, until the relative total divergence (see Section 4.6.3) for all the variables (i.e. U, V, W, P', K, ε, T) is less than 5×10^{-3} or until the number of iterations exceeds the prescribed maximum value.

- (10) Before the termination of the execution, the results are printed (and plotted).

CHAPTER 5
RESULTS AND DISCUSSION

5.1 GENERAL

Computational predictions for both the gas-agitated ladle and the T-shaped tundish are presented in this chapter. First, the predictions of the ladle with centered gas-jetting are presented and discussed. Then, the comparison of the predictions from the water model and the full-scale model is presented. The effect of off-centered gas-jetting in a full-scale model is analyzed next. Lastly, the numerical predictions of the T-shaped tundish are studied.

A numerical study of flow and heat transfer in a gas-agitated ladle is carried out. To examine how well the model behaves, velocity predictions for the small-scale runs were compared with Szekely's [54] and Guthrie's [64] experimental data for the water models of the same scale. Reasonably good agreement between the computations and the water models has been attained.

5.2 COMPUTATIONAL PREDICTIONS FOR CENTERED GAS-STIRRED LADLE

In this section, predictions for velocity and turbulence

properties are studied for the three centered, gas-stirred vessels. Both slip and non-slip conditions are tested. A slip velocity of 0.4 m/s is considered for all three vessels. For the two water models (i.e. vessel 1 and vessel 2), predictions are compared with the experimental results. For all three vessels, the ratio R_c/R is taken to be 0.25.

For vessel 1 with slip condition, the velocity profile is shown in Fig. 9. Generally, high velocity is observed in the mixture column, since the flow is buoyancy-driven by a lower density in the mixture column. Recirculation is observed. The center of the vortex appears near the top corner. Recirculation promotes downward flow near the side wall. Fig. 10 illustrates the turbulence kinetic energy distribution. The maximum K value is $0.014 \text{ m}^2/\text{s}^2$, and the ratio $K_{\text{max}}/(W_{\text{max}})^2$ is 12.9%. The maximum K value is located near the upper region of the mixture column surface, since the velocity gradient is high in this region. On the other hand, values of K are small at the center line because the velocity gradient there is low. The μ -distribution, which is shown in Fig. 11, is similar to the K -distribution. The upper region of the mixture column surface has a high turbulent viscosity. The ratio $\mu_{\text{max}}/\mu_{\text{lam}}$ is 1.513. The length scale distribution is shown in Fig. 12. The maximum length scale is located near the center of the vortex, whereas the length scale near the wall

is small. The ratio l_{\max}/R is 0.6748.

The same model of vessel 1 with non-slip condition was tested. Fig. 13 represents the velocity profile of centered bubbling with non-slip condition. The overall velocity is higher in the non-slip condition than that in the slip condition, as shown in Fig. 9. A higher turbulence effect results since a higher recirculation rate promotes higher velocity gradients in the entire domain. However, the general flow pattern and turbulence properties distributions are similar in both slip and non-slip conditions. The average plume velocity in the mixture column of the non-slip condition is 0.332 m/s, whereas in the slip condition it is 0.224 m/s.

The assumption of the average void fraction rather than the uniform gas concentration was also tested. Fig. 14 shows the velocity profile of centered bubbling, non-slip with the average void fraction calculated at every horizontal level. In the mixture column of the average void run, velocities close to the center line were a little higher than in the uniform gas distribution run (Fig. 13), whereas the velocities near the column surface of the average void run were lower. The small variation of the plume velocity, however, did not affect the rate of recirculation, since the velocities outside the mixture column for both runs are similar.

To demonstrate how recirculation affects the temperature distribution field, a test run of vessel 1 with non-slip condition was executed with a layer of slag on the top surface. This layer of slag would act as a top wall. The slag temperature was higher than the bottom wall temperature by a difference of ΔT , and both temperature were fixed. The side wall was insulated. Initially the fluid had a uniform thermal stratification. At convergence, the temperature distribution was uniform between $T_{\text{bottom}} + 0.66\Delta T$ and $T_{\text{bottom}} + 0.67\Delta T$.

To examine the validity of the present model, the predicted velocity distributions were compared not only with Szekely's experimental data, but also with predicted results from a model developed based on the Los Alamos MAC method (Salcudean et al [58]). The measured velocity distribution by Szekely et al [54] of vessel 1 is presented in Fig. 15a. Salcudean's et al predicted results [58], which are based on the Los Alamos MAC method, are illustrated in Fig. 15b. The Los Alamos model is for transient flow and was run until steady-state was reached. General agreement between measurements and predictions in Fig. 9, 13, 14, 15a, 15b can be noted, since the general flow patterns are very similar.

Test cases of vessel 2 with both slip and non-slip conditions were run, and the velocity distributions are shown in Fig. 16 for slip conditions, and in Fig. 17 for

non-slip conditions. Again, the overall velocity in the non-slip conditions is about 20% higher than that of the slip conditions. When the velocity distributions are compared with Guthrie's [64] measurements (Fig. 18), reasonably good agreement can be found. By looking at the axial velocity component versus radial distance in various Z/H ratio (Fig. 19), good agreement between the measurements and predictions can be found.

5.3 FULL-SCALE AND OFF-CENTERED JETTING PREDICTION

The predicted velocity distributions and turbulence characteristics distributions for a steel ladle with both centered and off-centered jetting are commented upon and compared with the water model. The velocity distribution of the full-scale run for a 150-ton, centered-jetting steel vessel with slip condition is presented in Fig. 20. The velocities in vessel 3 are larger than the velocities in vessel 1, since the column height and the density difference between the liquid and the gas have been increased. The maximum velocity is 1.58 m/s which is more than four times that in the water model vessel. Average plume velocity is 1.08 m/s for slip condition. The general flow pattern is similar to that of the water model prediction. The vortex center is close to the top and the side wall, because of

larger fluid entrainment. The turbulent kinetic energy distribution for vessel 3 is shown in Fig. 21. The maximum turbulent kinetic energy has increased seventeen times compared to that in vessel 1, since the maximum velocity in the steel vessel has increased more than four times compared to that in the water model. The ratio $K_{\max}/(W_{\max})^2$ is 0.10, which is comparable to the same ratio in the water model (reduced scale) which is 0.13. The maximum effective viscosity of vessel 3 (shown in Fig. 22) is 157 N-s/m², which is about one hundred and thirty times that of vessel 1. Again, the μ -distributions for both vessel 1 and vessel 3 are very similar. The length scale distribution is shown in Fig. 23. The ratio l_{\max}/R is 0.6212 which is a little smaller than the one in vessel 1.

The off-centered jetting is often practiced in the steel industry. It is worthwhile to examine how the off-centered gas jets affect the flow. A schematic diagram of the vessel with off-centered jetting is shown in Fig. 24. The gas plug is located midway between the center line and the left wall. Fig. 25a and 25b illustrate the velocity distributions of vessel 1 with off-centered jetting and slip condition. Fig. 25a illustrates the predicted results from the present model and Fig. 25b the results from the Los Alamos model [58]. Good agreement between the two models

can be observed. The velocity distribution of vessel 3 with non-slip, off-centered jet is presented in Fig. 26. A strong recirculation can be observed near the top center region of the vessel. Two small vortices are found near the left side-wall. The average plume velocity is 1.04 m/s, and it is 14% lower than that in the centered-bubbling model. The maximum velocity is 1.48 m/s which is again 14% lower than that in the centered-bubbling model. In the mixture column (Fig. 26), velocities close to the left wall are higher than the velocities close to the center line. This is due to the asymmetry of the plume; less fluid is entrained in the left side of the vessel than in the right side, therefore less redistribution of momentum occurs.

The kinetic energy of turbulence distribution is shown in Fig. 27. Again, the maximum value is found near the mixture column surface and the free surface. The K values near the center portion of the mixture column are small. Generally, the kinetic energy of turbulence in the right-hand part of the vessel shown in Fig. 27 is less than 10% of the maximum K value. The maximum K value is evaluated at $0.43 \text{ m}^2/\text{s}^2$ which is seventeen times higher than that in the centered-bubbling vessel. This can be explained since the velocity gradient in this region is higher than that in the corresponding region in the centered-bubbling model. One side of the mixture

column is close to the wall and the fluid entrainment becomes small. The effective viscosity distribution is shown in Fig. 28 and 29. Similar to the K distribution, the maximum value is located in the outer zone of the mixture column surface near the free surface, and the μ value in the center portion of the mixture column is small. Generally, turbulence is higher near the free surface than near the side walls and bottom wall. μ_{\max} is 225 N-s/m² and the ratio $\mu_{\max}/\mu_{\text{lam}}$ is 45,000. These values indicate that the turbulence effect is significant. The maximum degree of turbulence is about 40% higher than that in the centered-bubbling. The length scale distribution is shown in Fig. 30. The maximum length scale is located below the center of recirculation near the upper center region. The ratio l_{\max}/R is 0.772, which is about 25% higher than that in the centered-bubbling model.

5.4 COMPUTATIONAL PREDICTIONS FOR A T-SHAPED TUNDISH

Velocity and turbulence properties predictions for the T-shaped tundish are analyzed. A few comparisons of the predictions with the experimental flow directions are studied. These flow directions are obtained from Chushao Xu of McGill University who recently built a water model similar to Heaslip's [65]. The velocity directions of the predictions in the horizontal cuts near the top and bottom planes and the vertical

cuts near the inlet and outlet orifices (Fig. 31 through 35) coincide with the experimental directions (Fig. 36a and 36b). Velocities are much higher near the two orifices. The ratio of the average recirculatory speed to the inlet velocity is in the order of 10^{-2} . On examining the flow patterns, it is noticed that most inlet fluid changes direction by 180° after hitting the bottom wall. Some of this upward flowing fluid hits the top free surface and then flows downward to the exit orifice. This path enhances inclusions to float on the free surface and join the layer of slag. The temperature distribution in the tundish was examined. The inlet temperature was kept 10° (ΔT) higher than the wall temperature. All the walls were kept at a constant temperature. The temperature distribution predictions (Fig. 37 through 40) show that the inlet fluid was cooled by the wall such that outlet temperature was $0.05\Delta T$ higher than the wall temperature. With these predictions, the ladle outlet temperature, the tundish inlet flow rate, and the tundish wall temperature could be adjusted carefully to control the temperature of molten steel going into the mold.

The turbulence parameters shown in Fig. 41 through 43 determine the degree of turbulence in the tundish. A high turbulent kinetic energy was found in the inlet region since the velocity gradient is high in this region. For the same

reason, a relatively high level of turbulence kinetic energy was found in the outlet region. In most of the wall regions and corners, the effective viscosity was comparable to laminar viscosity.

Some of the fluid does leave the tundish in a short path without being recirculated (this is also known as short-circuiting). Short-circuiting is not desirable in the tundish operation since inclusions may leave the tundish and solidify in the mold, thus degrading the thermal and mechanical properties of the steel. More research should be done in this area so that baffles can be built between the inlet and outlet orifices to eliminate short-circuiting.

CHAPTER 6CLOSURE6.1 CONCLUSIONS

The numerical procedure based on the SIMPLE algorithm has been successfully developed for application to the buoyancy-driven flow and forced-convection-driven flow dealt with in this study. The three-dimensional, $K-\epsilon$ turbulence model employed has been found adequate for buoyancy-driven flows and forced-convection, recirculatory flows in cavities.

For the gas-agitated ladle, agreement between present predictions and the available experimental data is satisfactory. From the turbulence parameters predictions, a much stronger turbulence in the full-scaled, steel ladle was observed (compared to the water model). On the other hand, some interesting aspects of the flow in the T-shaped tundish (regarding the velocity and turbulence distributions) for which no data or previous computations were available, have been revealed by the predictions. The elaborated model can be applied to investigate other three-dimensional turbulent flows (flows in molds, converters, etc.).

6.2 RECOMMENDATION FOR FUTURE WORK

Some possible areas for future study in connection with this work are suggested:

- (i) In ladle modelling, a cylindrical mixture column was employed to represent the buoyant plume. Other configurations of the buoyant plume (e.g. conical) should be investigated.
- (ii) Variable void or gas distributions for the mixture column should be investigated since these conditions approach a more realistic model.
- (iii) The present off-centered jetting model and the tundish model should be compared with experimental models as the experimental data becomes available.
- (iv) Full-scale tundish computations should be carried out for the T-shaped tundish and other geometries.
- (v) The design of baffles in the T-shaped tundish to avoid short-circuiting, should be investigated.
- (vi) The values of the model constants used in the present model should be reviewed, since they may not be adequate for the molten steel.

Figure 1 (a) Vertical, bend-strand, and curved-mold continuous-casting machines (Wagstaff and Stock, 1975).
 (b) Arrangement of continuous-casting machine at Atlas Steels (Wagstaff and Stock, 1975)

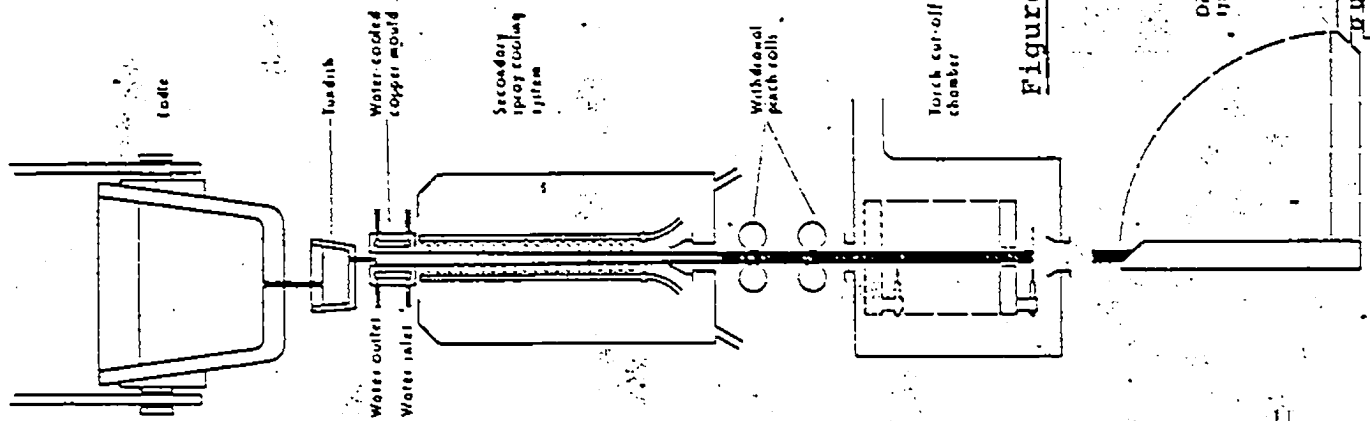


Figure 1b

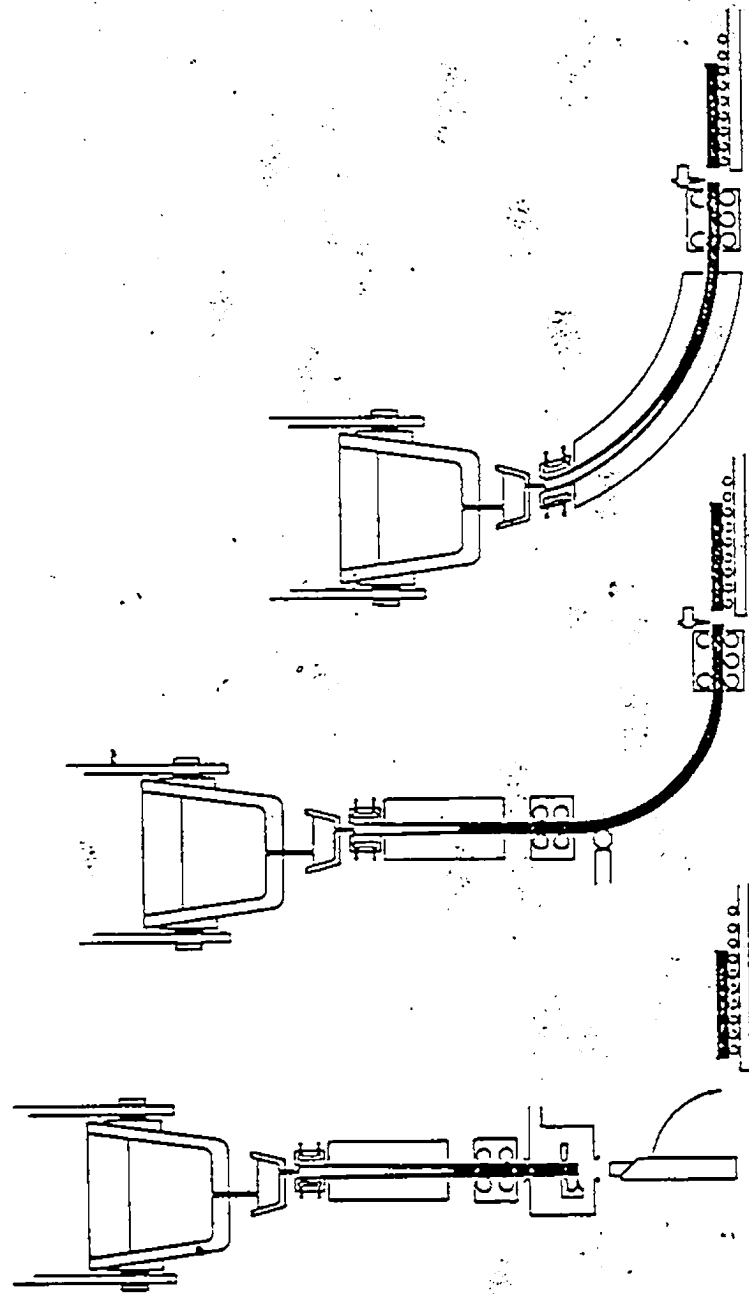


Figure 1a

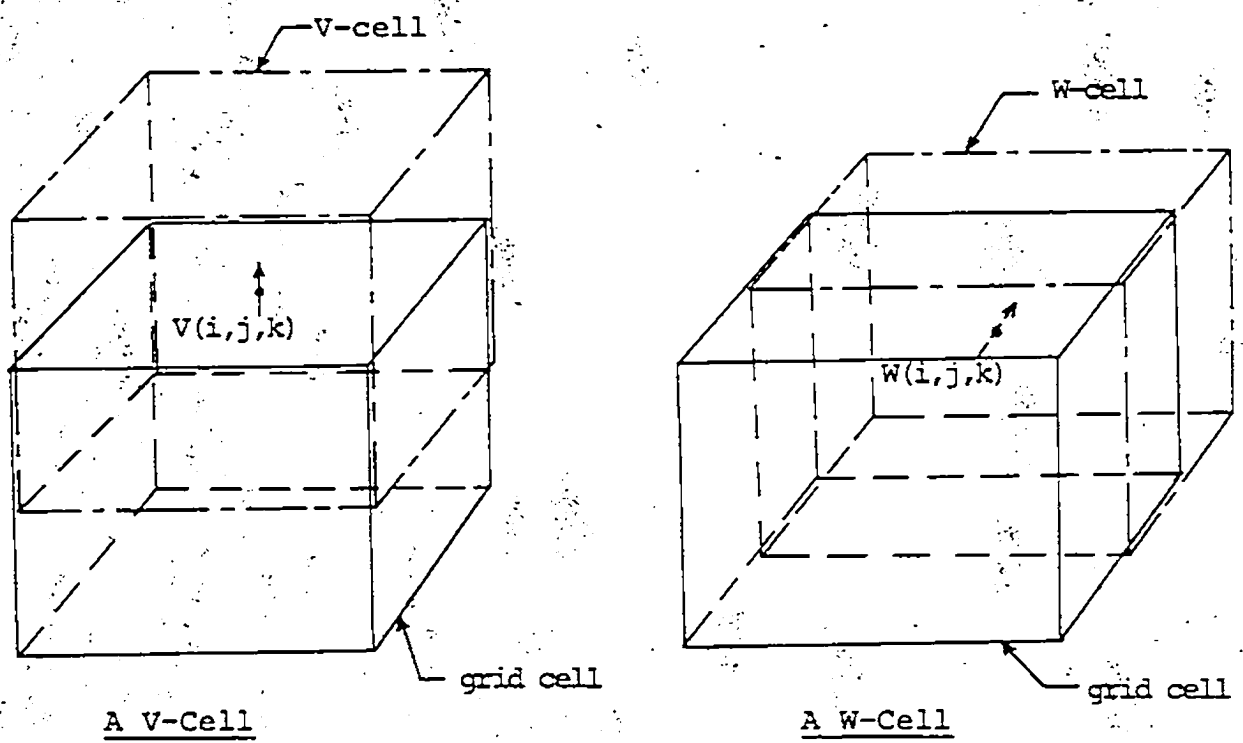
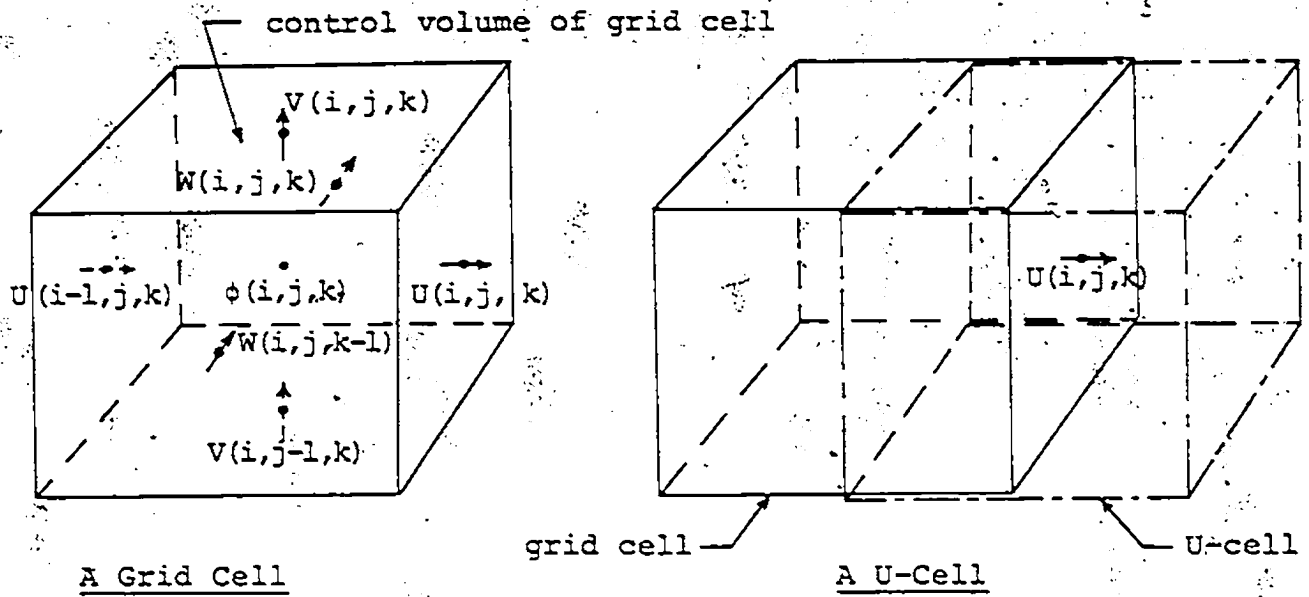


Figure 2 Cell arrangements for Cartesian Coordinates

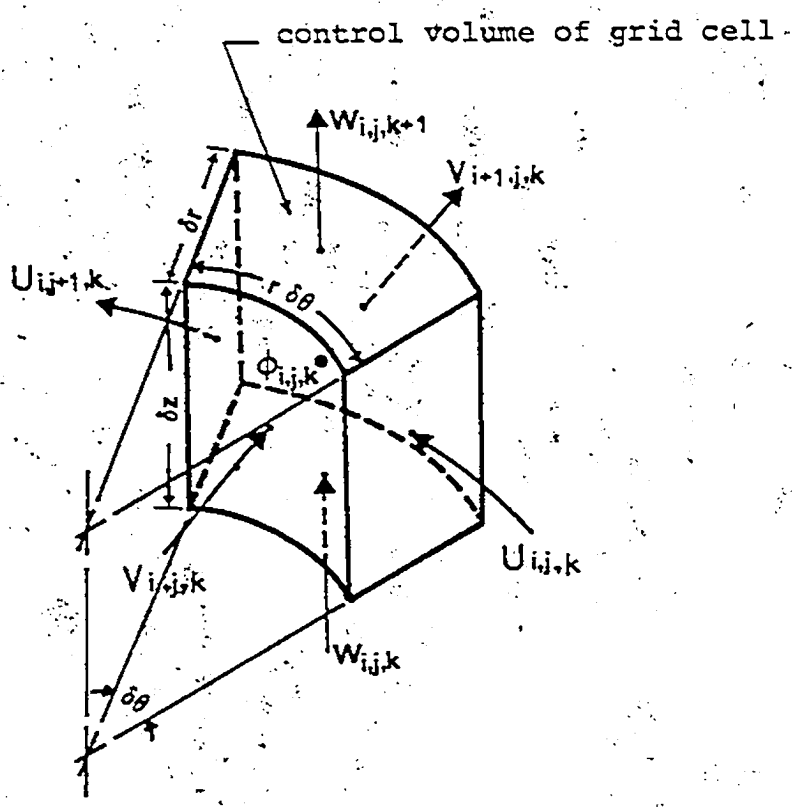


Figure 3 A grid cell for cylindrical coordinates

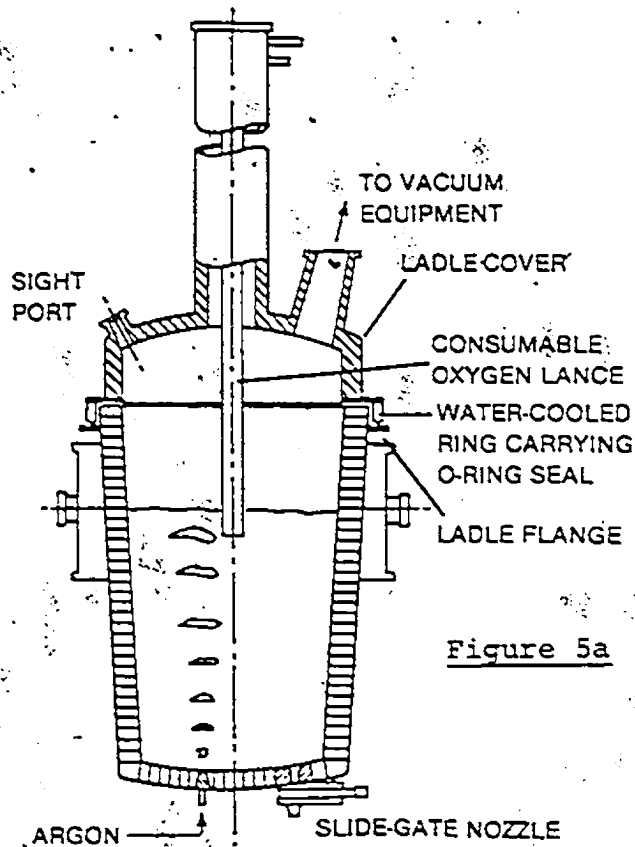


Figure 5a

Figure 5 (a) Arrangement of ladle, cover and consumable lance in the vacuum-oxygen decarburization process in Atlas Steels [34], (b) Schematic diagram of centered jet and (c) Schematic diagram of off-centered jet.

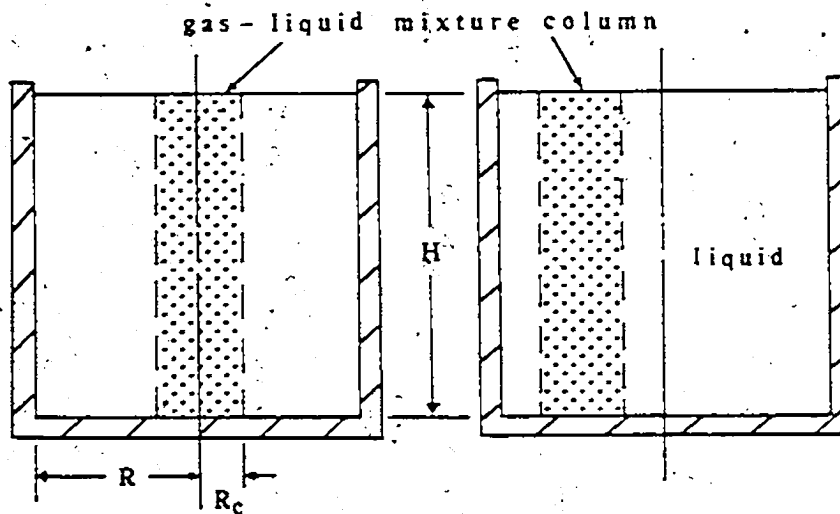


Figure 5b

Figure 5c

Figure 6 Schematic diagram of the T-shape tundish

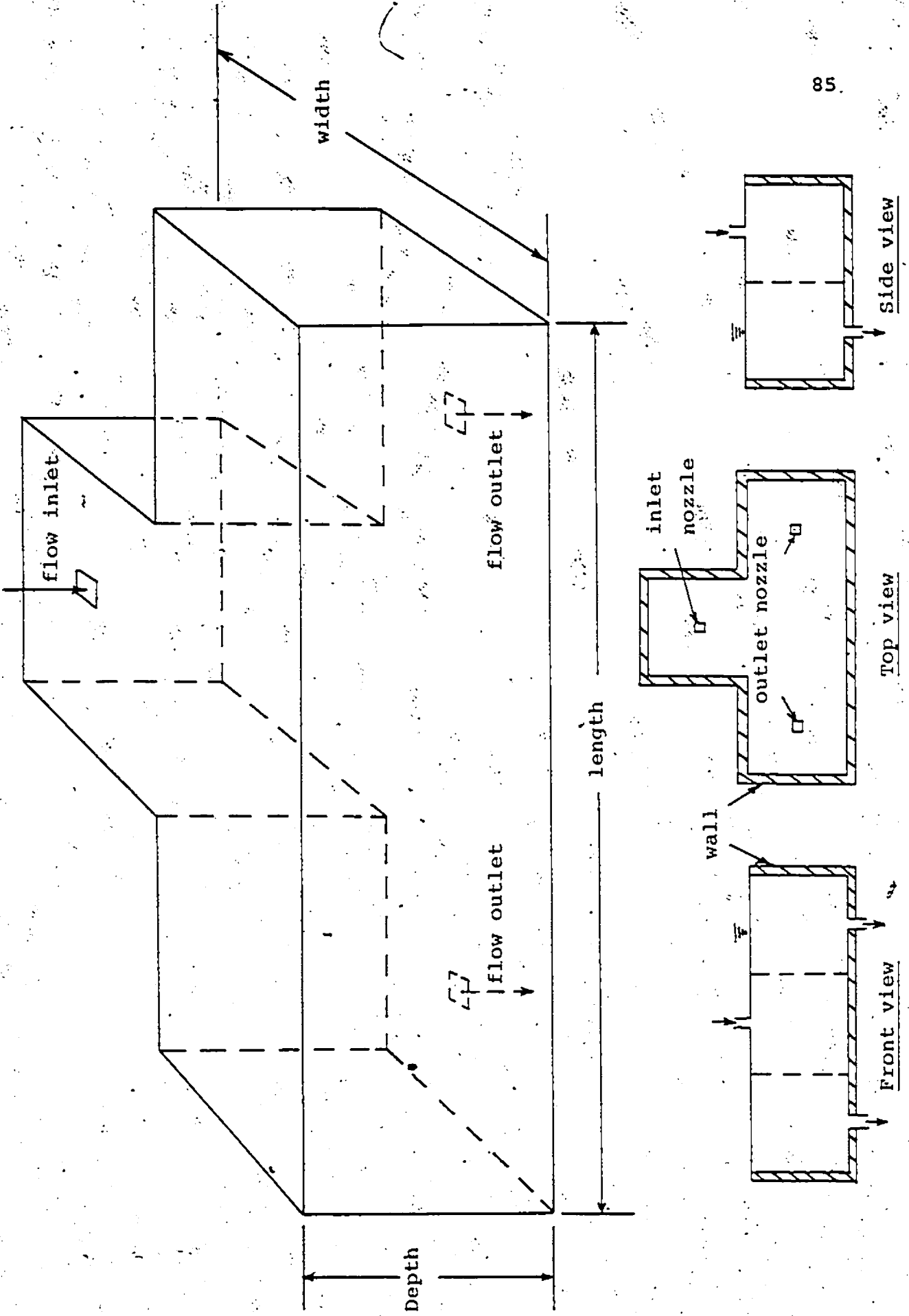
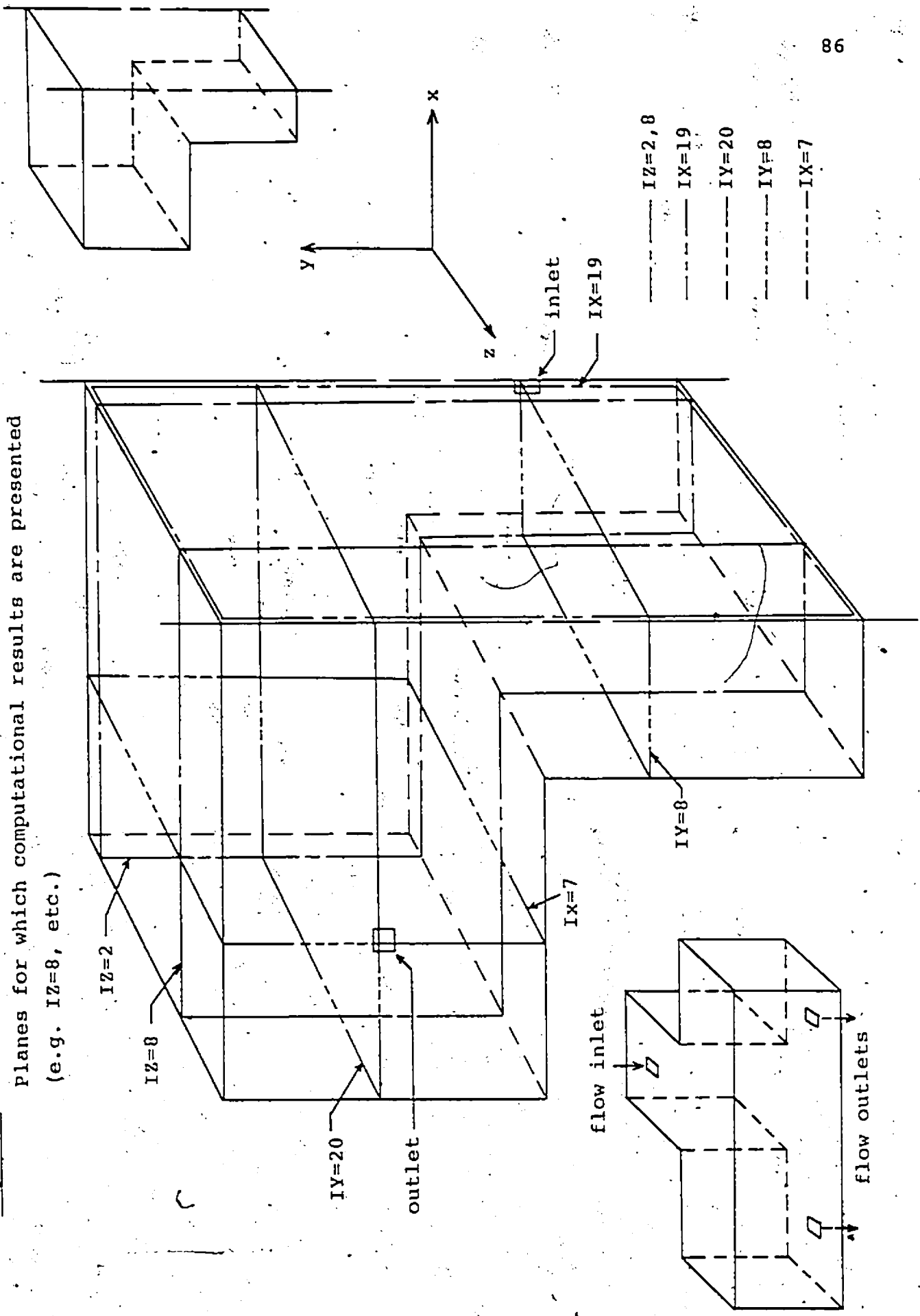


Figure 7 Schematic diagrams of the T-shaped tundish (half).
 Planes for which computational results are presented
 (e.g. IZ=8, etc.)



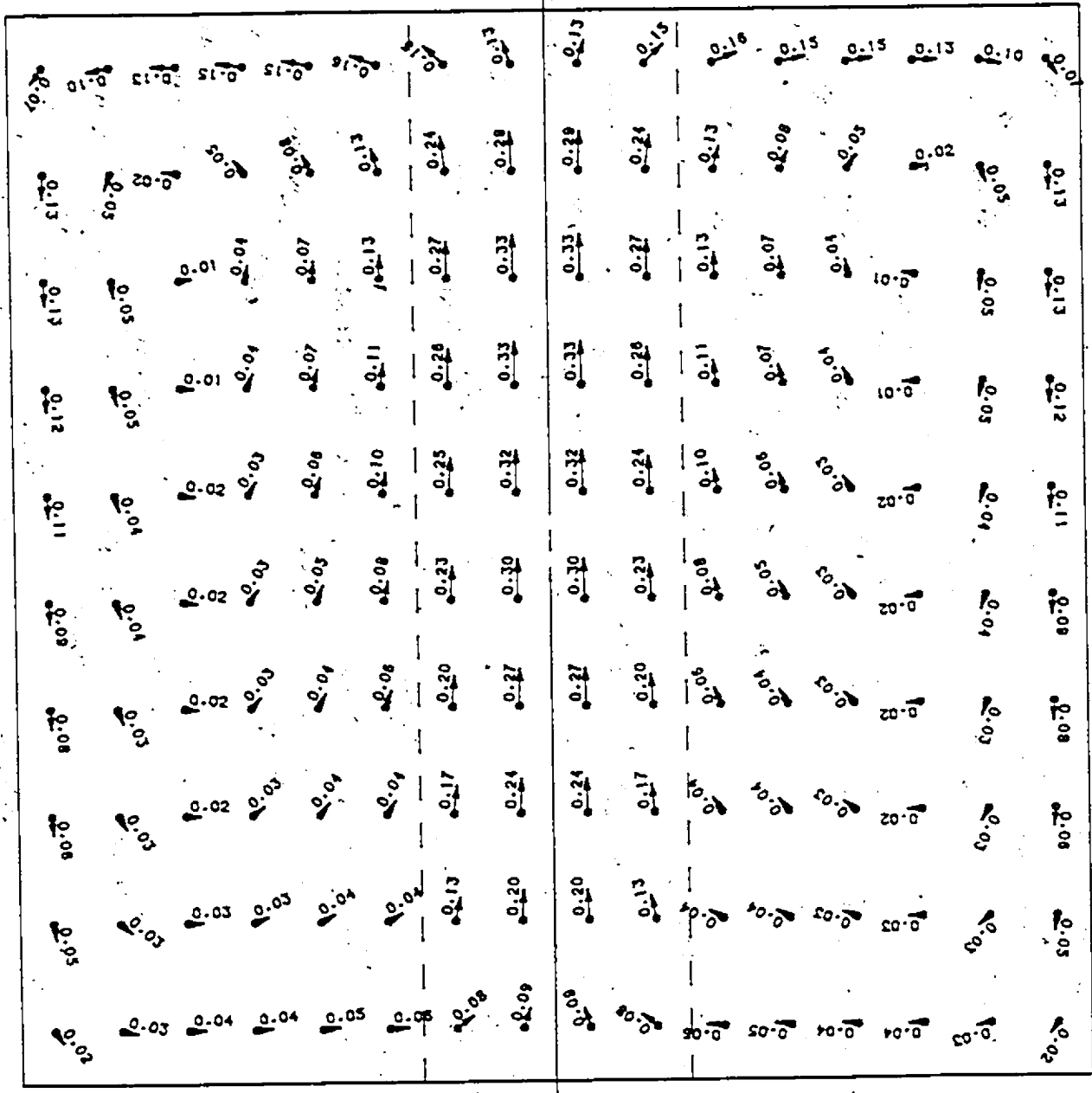


Figure 9 Computed velocity distribution in vessel 1.
Centered jet with slip. Computed values in m/s.

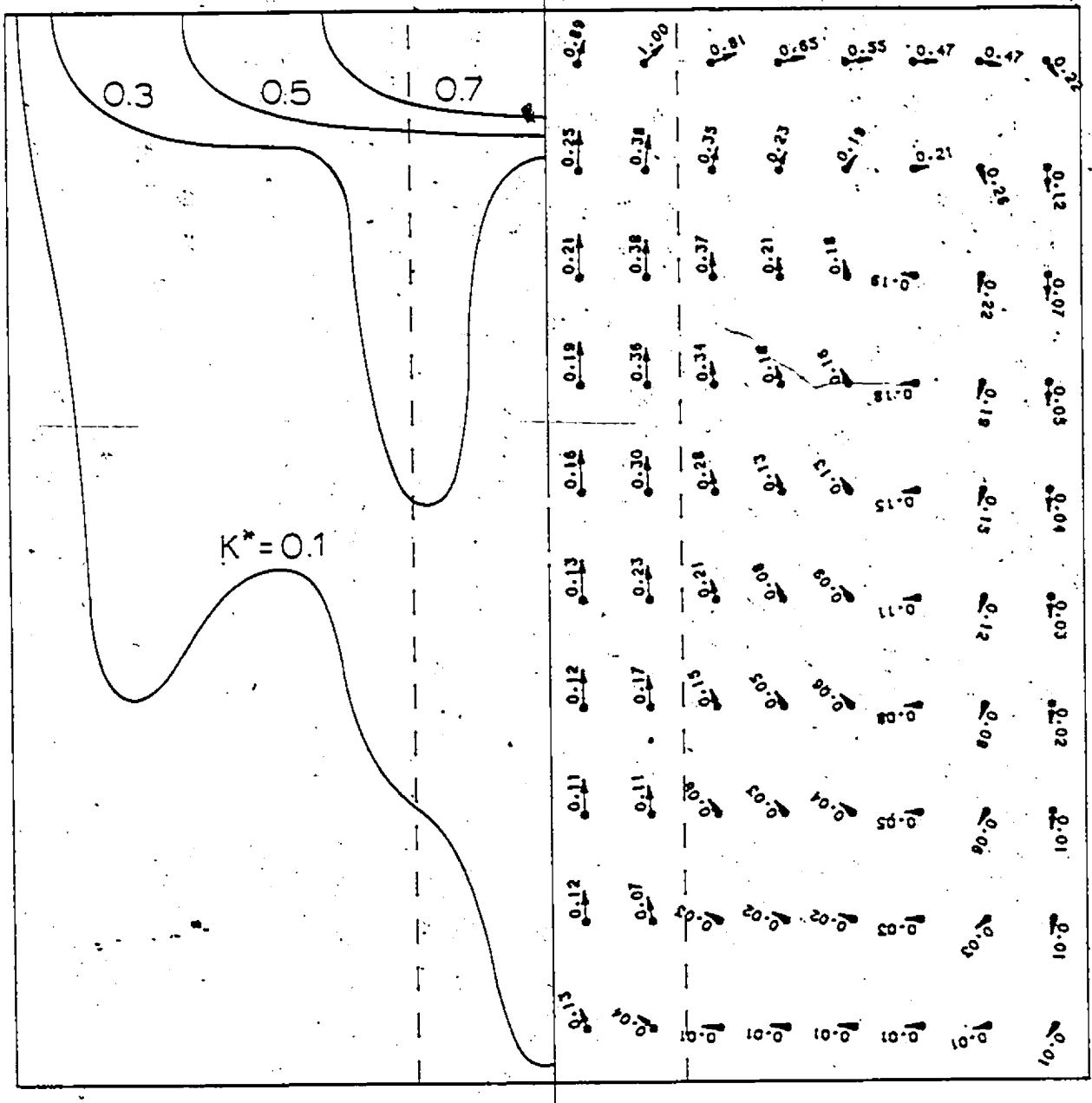


Figure 10 Predicted turbulence kinetic energy distribution in vessel 1. Centered jet with slip.
 $K^* = K/K_{\max}$, $K_{\max} = 0.014 \text{ m}^2/\text{s}^2$, $K_{\max}/(W_{\max})^2 = 0.129$

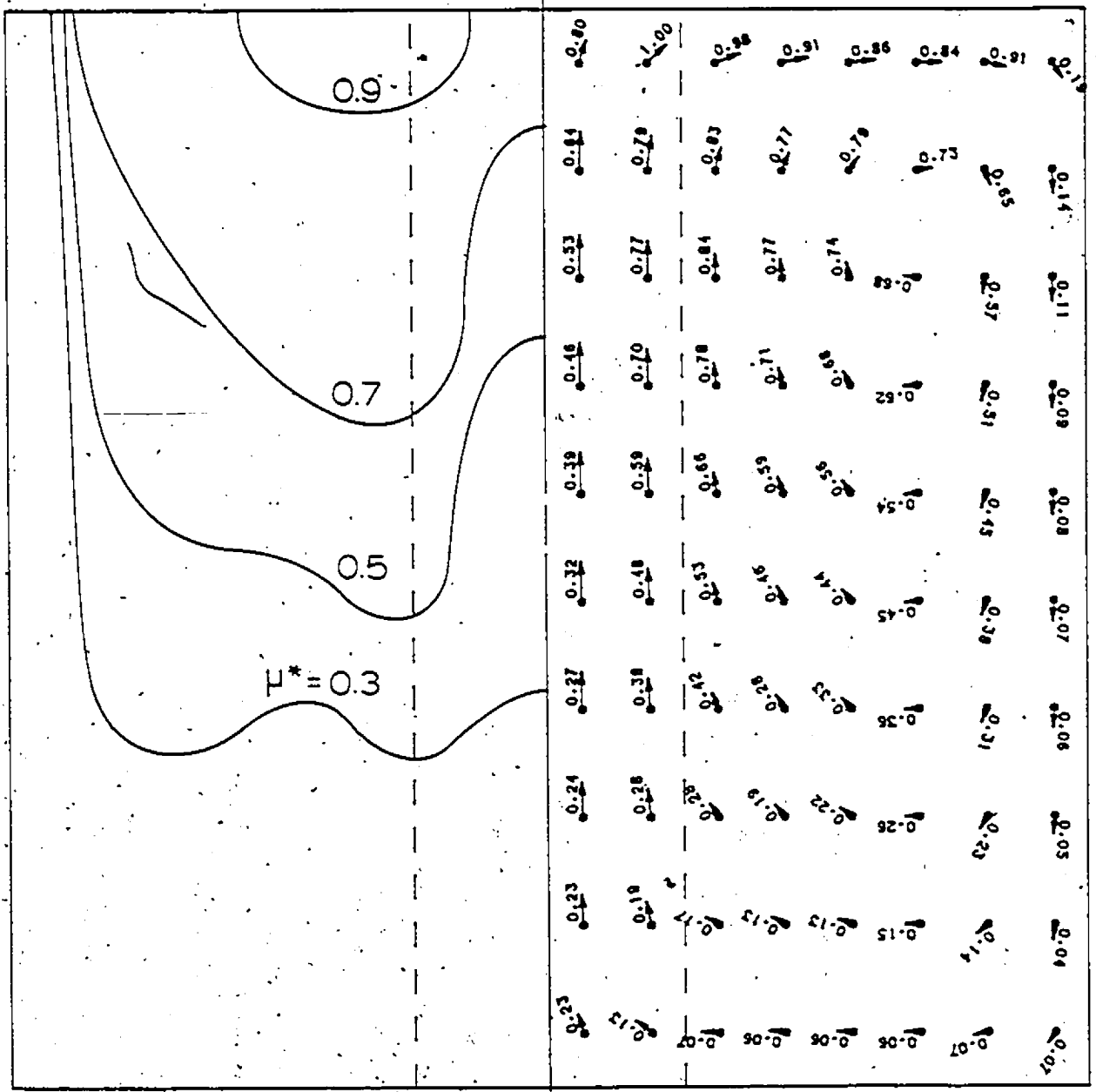


Figure 11 Predicted effective viscosity distribution in vessel 1. Centered jet with slip.
 $\mu^* = \mu_{\text{eff}} / \mu_{\text{max}}$, $\mu_{\text{max}} = 1.21 \text{ N-s/m}^2$, $\mu_{\text{max}} / \mu_{\text{lam}} = 1513$

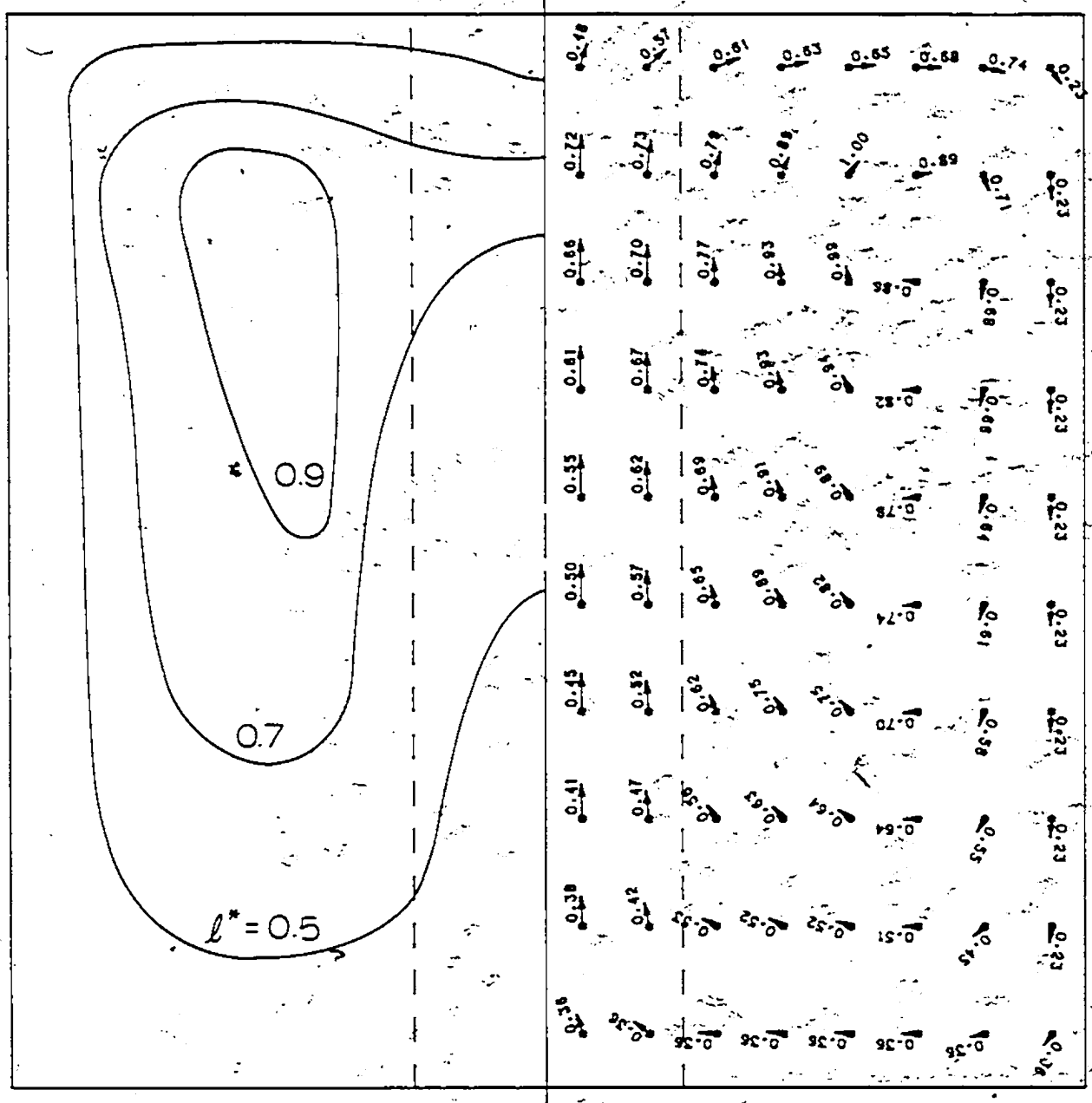


Figure 12 Predicted characteristic length scale distribution in vessel 1. Centered jet with slip.

$$l^* = l/l_{\max}, \quad l_{\max}/R = 0.675$$

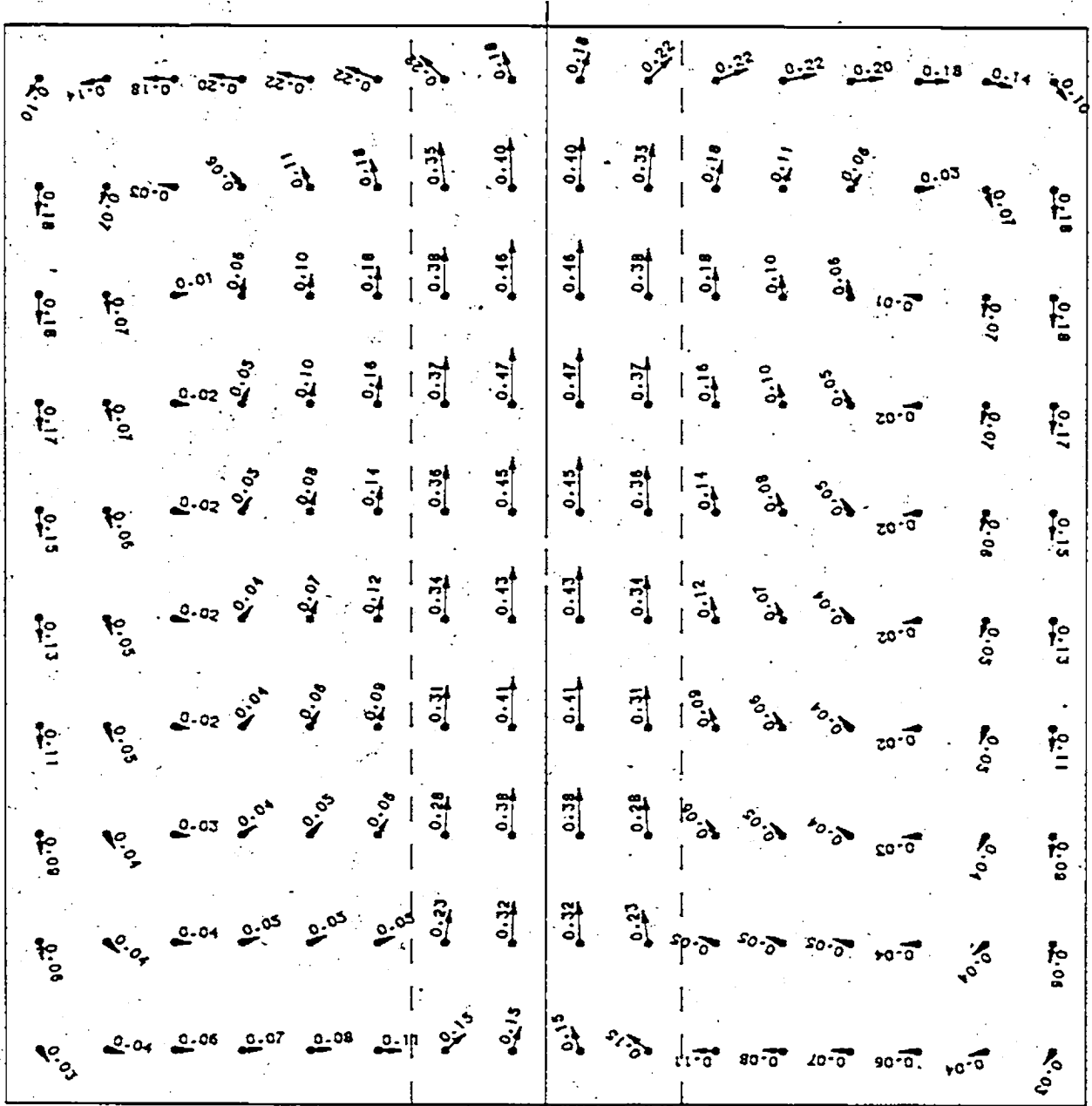


Figure 13 Computed velocity distribution in vessel 1.
 Non-slip centered jet. Computed values in m/s.

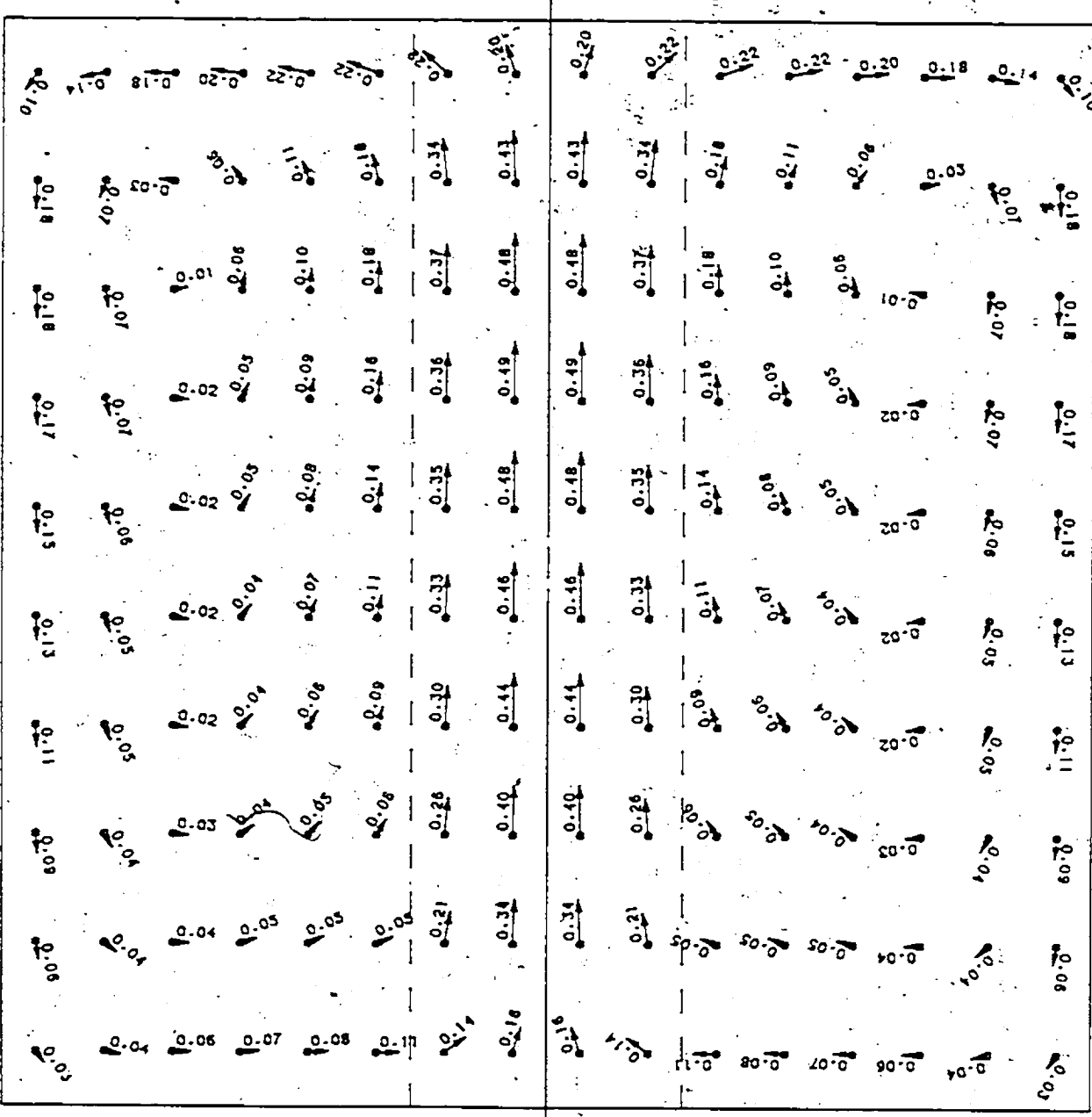


Figure 14 Predicted velocity distribution in vessel 1. Non-slip centered jet with average void fraction calculated at each horizontal level. Computed values in m/s.

Figure 15a

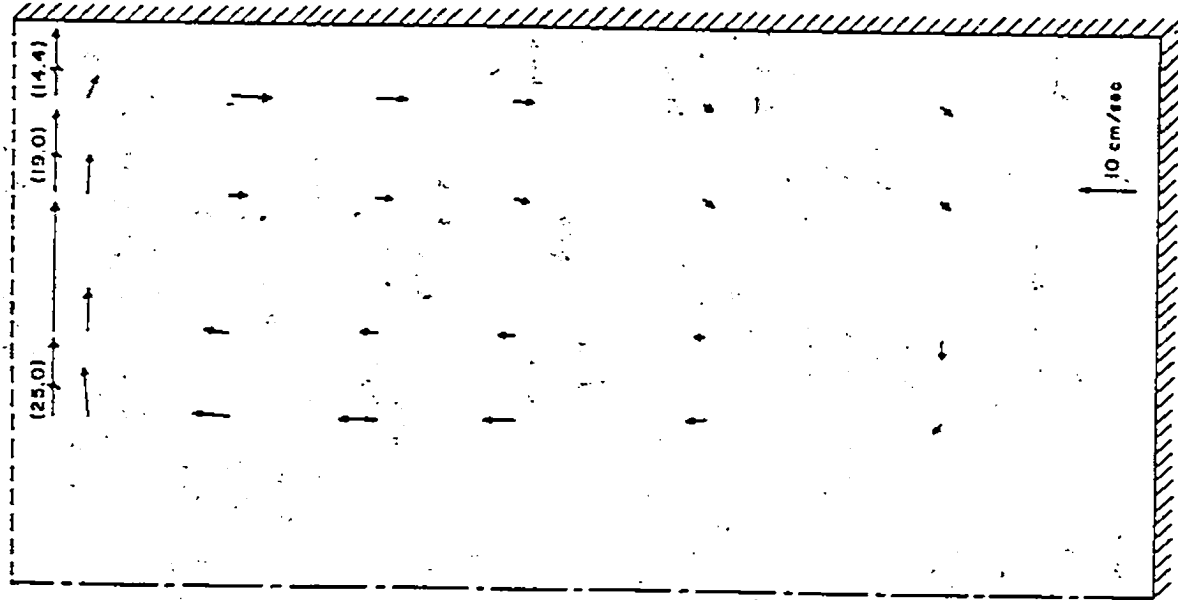


Figure 15b

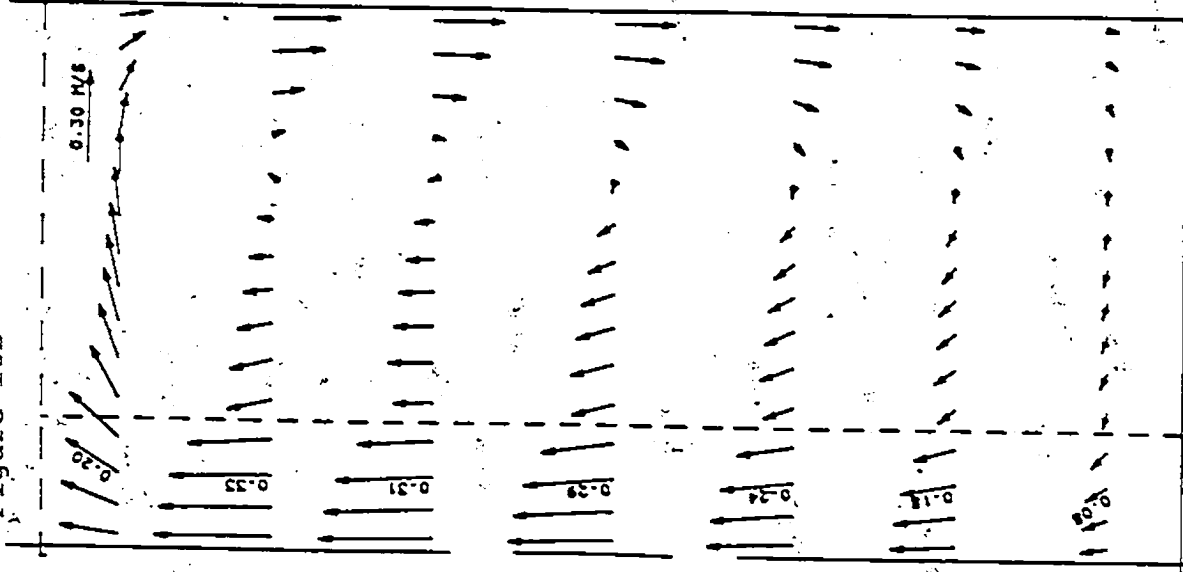


Figure 15 (a) Szekely's et al experimental flow pattern [54] in vessel 1. Centered jet. 9
(b) Salcudean's et al predicted velocity pattern [58] in vessel 1. Centered jet with slip.



Figure 16 Predicted velocity distribution in vessel 2.
Centered jet with slip. Computed values in m/s.

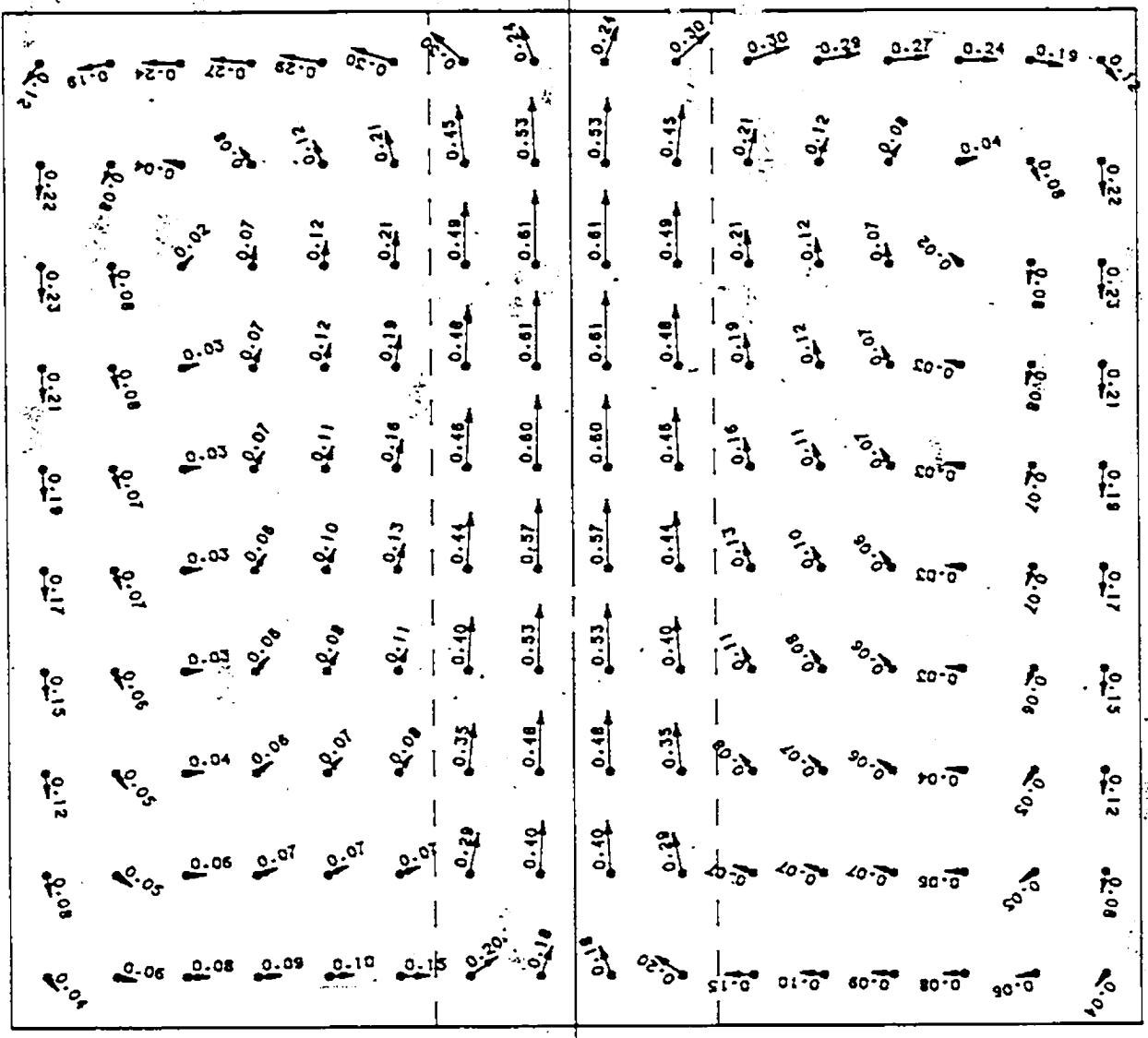


Figure 17 Predicted velocity distribution in vessel 2.
Non-slip centered jet. Computed values in m/s.

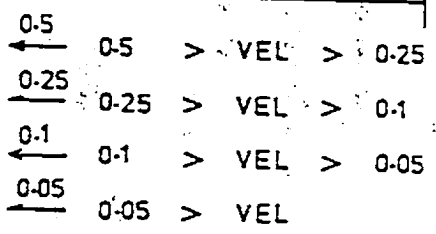
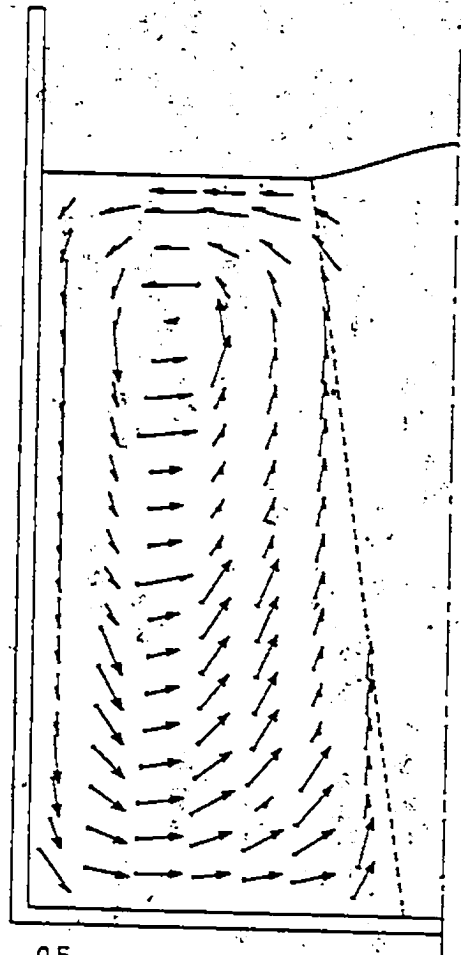


Figure 18 Guthrie's et al experimental flow pattern in vessel 2. Velocities in m/s.

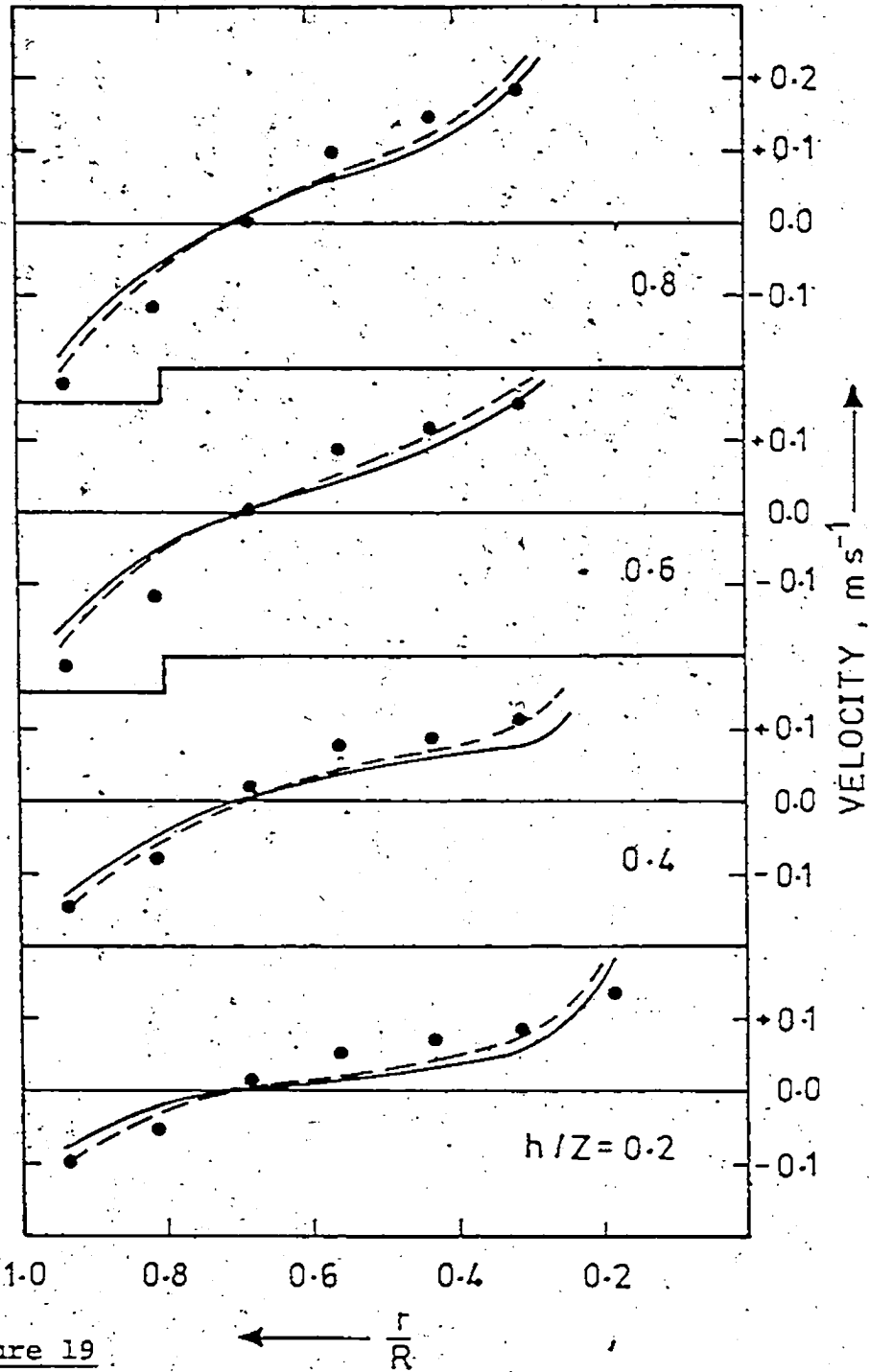


Figure 19

Comparison of experimentally measured [63] and predicted vertical velocity components at different depths in vessel 2

- Experimental
- slip
- non-slip

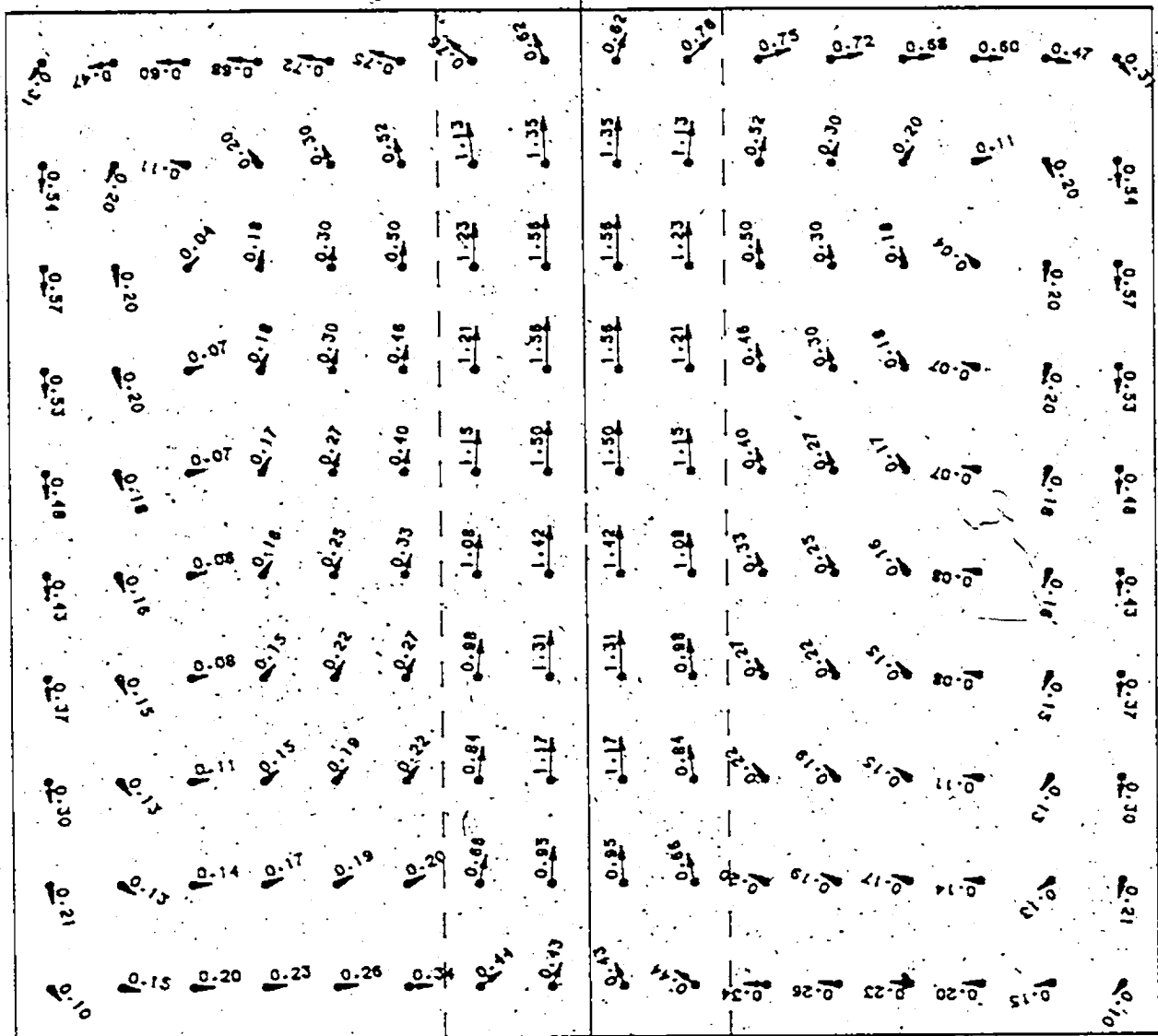


Figure 20 Predicted velocity distribution in vessel 3.
Centered jet with slip. Computed values in m/s.

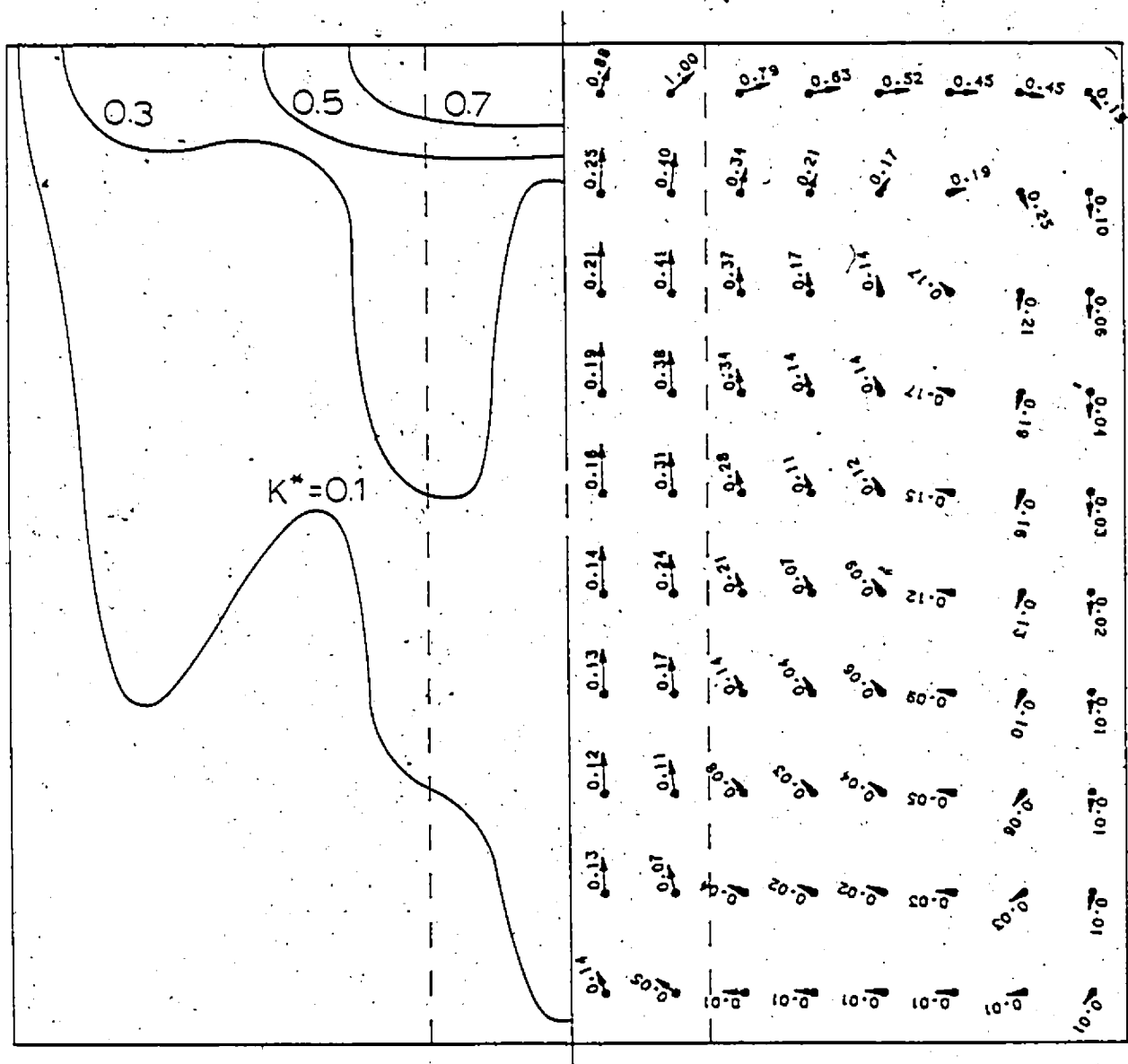


Figure 21 Predicted turbulence kinetic energy distribution in vessel 3. Centered jet with slip.
 $K^* = K/K_{max}$, $K_{max} = 0.253 \text{ m}^2/\text{s}^2$, $K_{max}/(W_{max})^2 = 0.104$

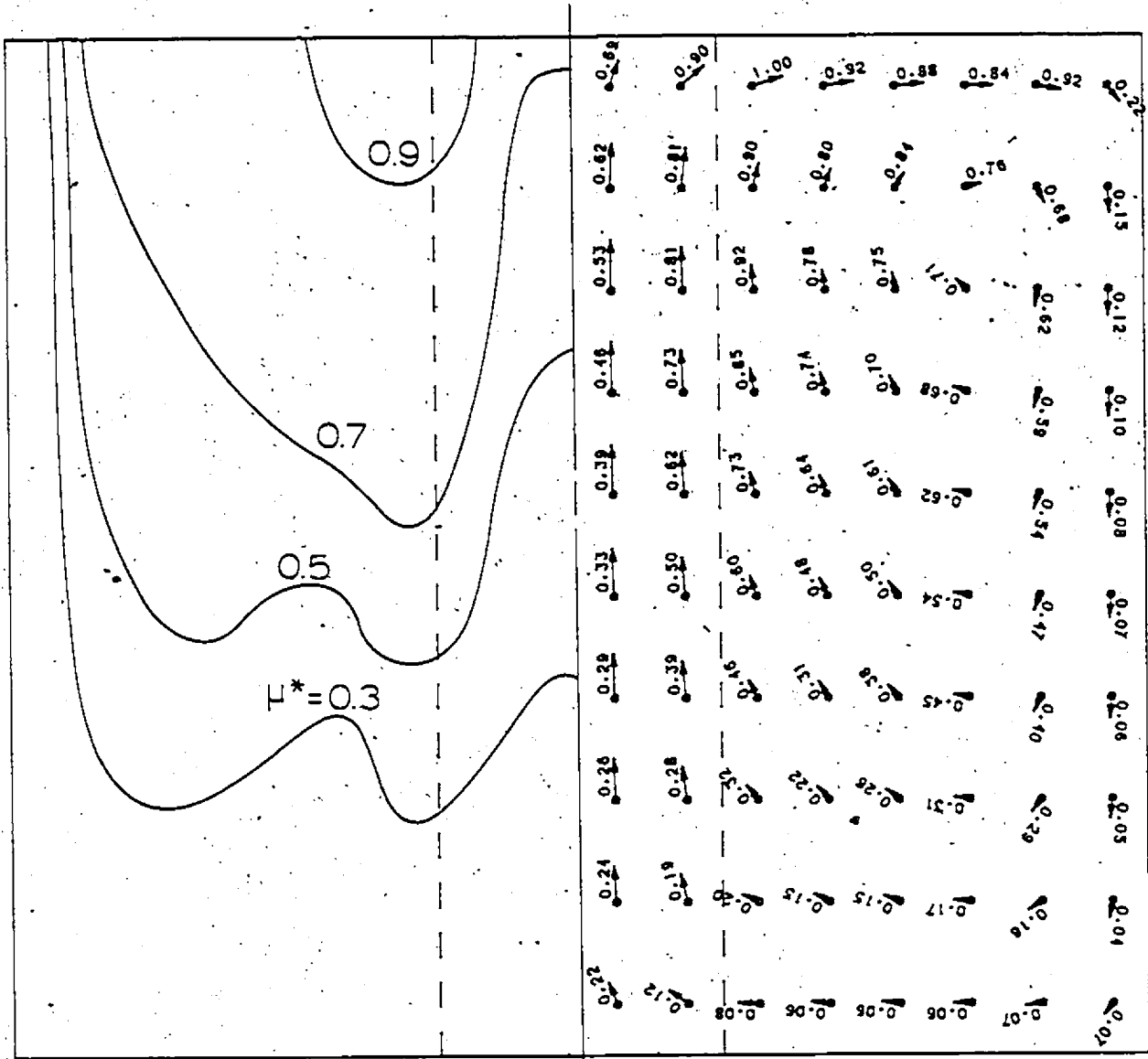


Figure 22 Predicted effective viscosity distribution in vessel 3. Centered jet with slip.

$$\mu^* = \mu_{\text{eff}} / \mu_{\text{max}}, \quad \mu_{\text{max}} = 157 \text{ N-s/m}^2, \quad \mu_{\text{max}} / \mu_{\text{lam}} = 31400$$

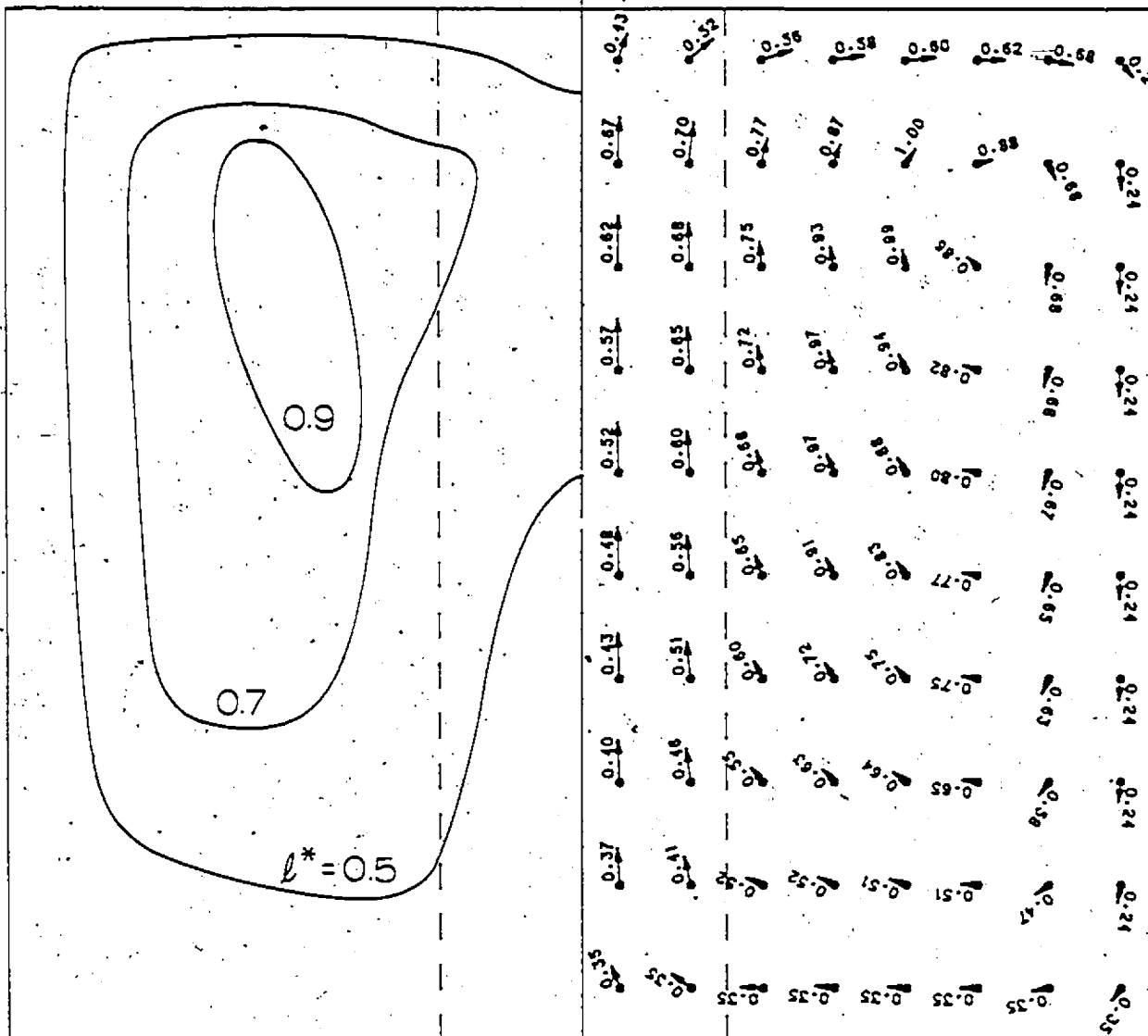


Figure 23 Predicted characteristic length scale distribution in vessel 3. Centered jet with slip.

$$l^* = l/l_{\max}, \quad l_{\max}/R = 0.6212$$

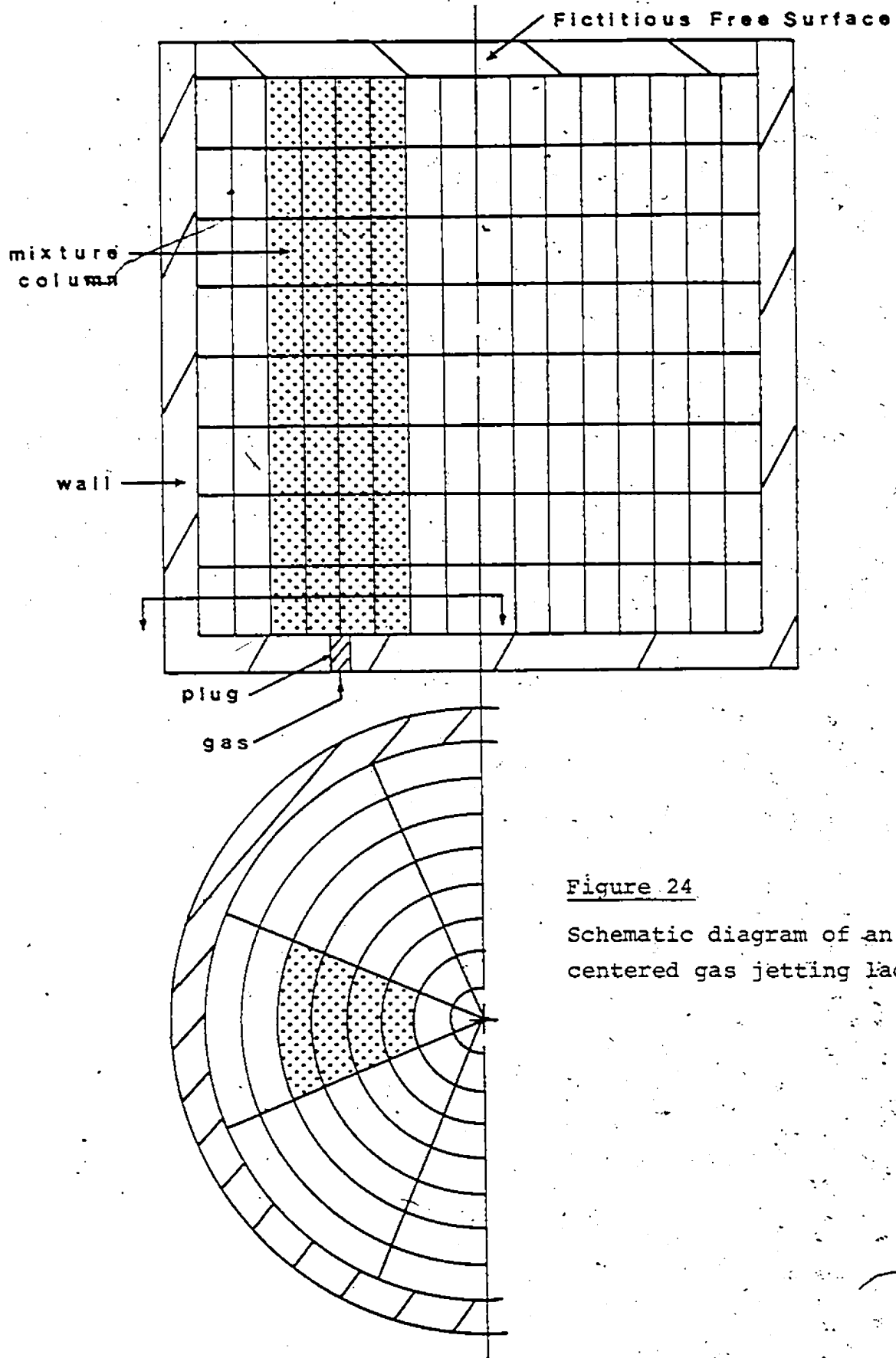


Figure 24
Schematic diagram of an off-centered gas jetting ladle.

Figure 25(b)

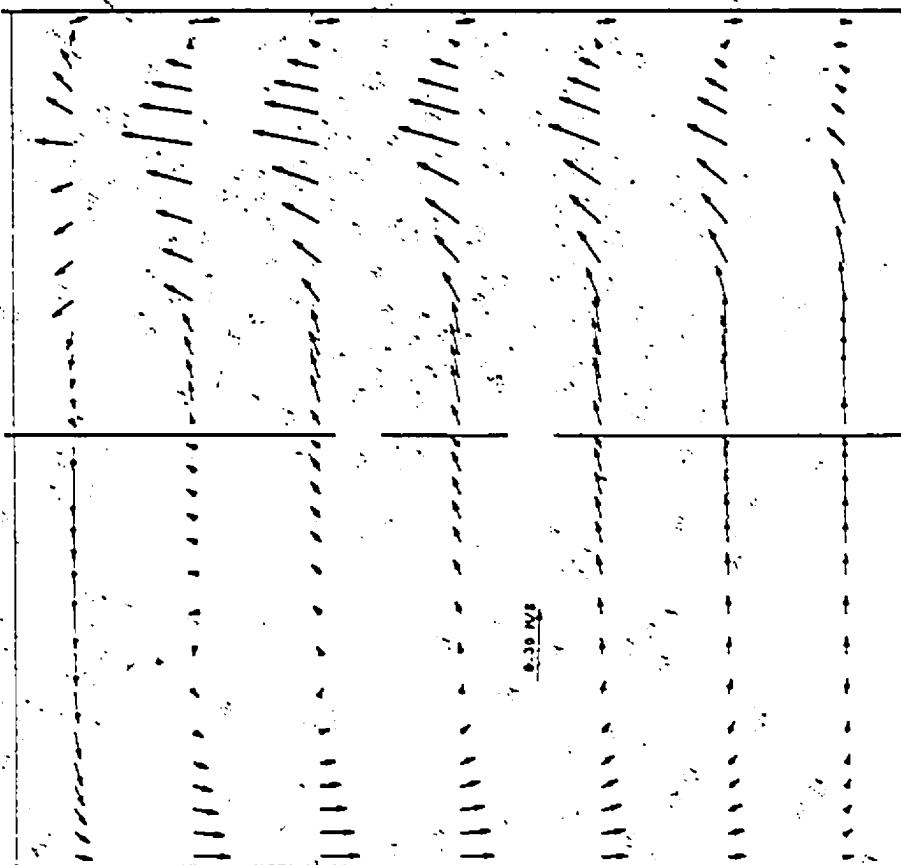


Figure 25(a)

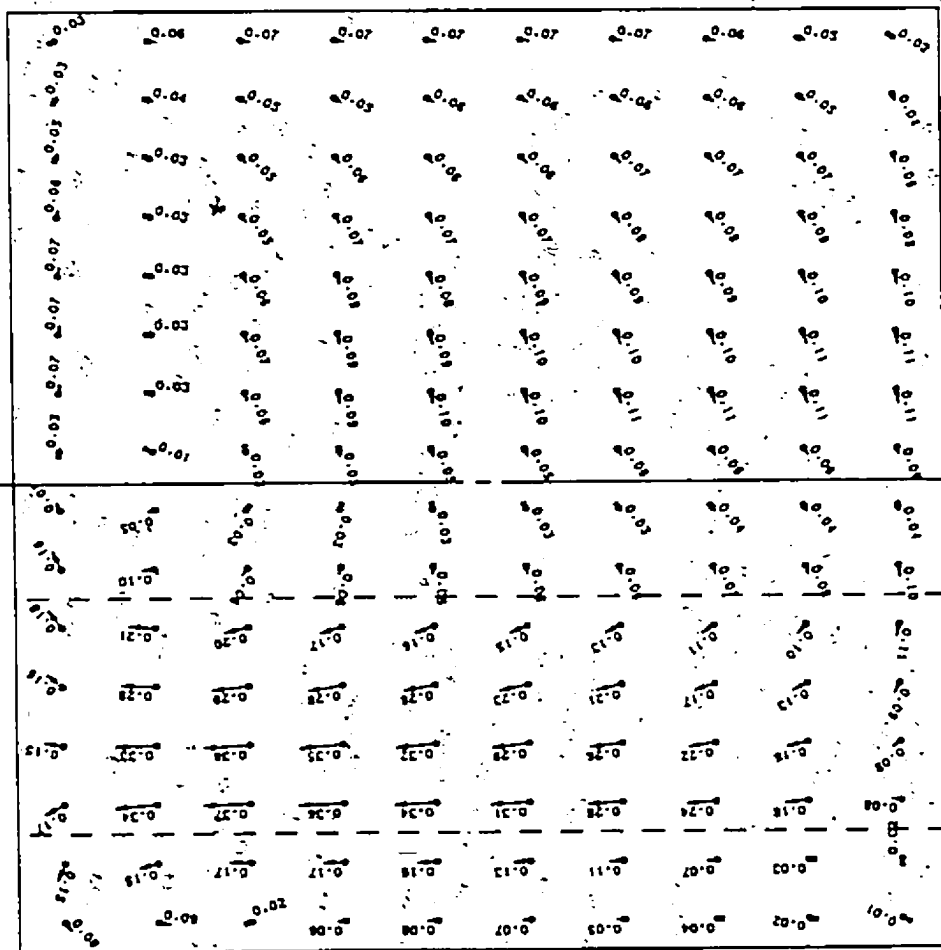


Figure 25 (a) predicted velocity distribution in vessel 1. Off-centered jet with slip.
 Computed values in m/s. (b) Salcudean's et al predicted velocity distribution
 in vessel 1. Off-centered jet with slip.

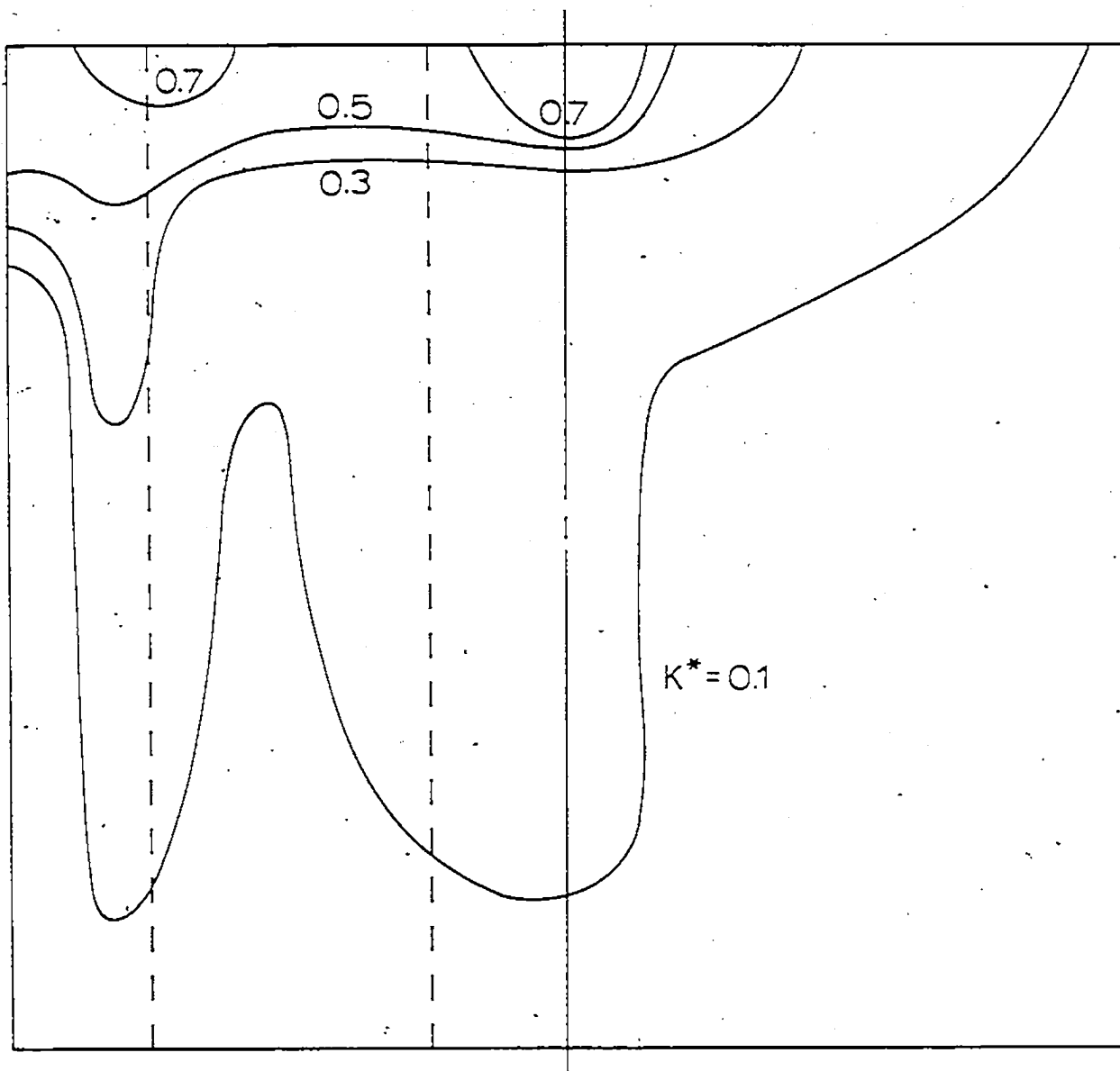


Figure 27. Predicted turbulence kinetic energy distribution in vessel 3. Non-slip off-centered jet.

$$K^* = K/K_{\max}, \quad K_{\max} = 0.430 \text{ m}^2/\text{s}^2, \quad K_{\max}/(W_{\max})^2 = 0.186$$

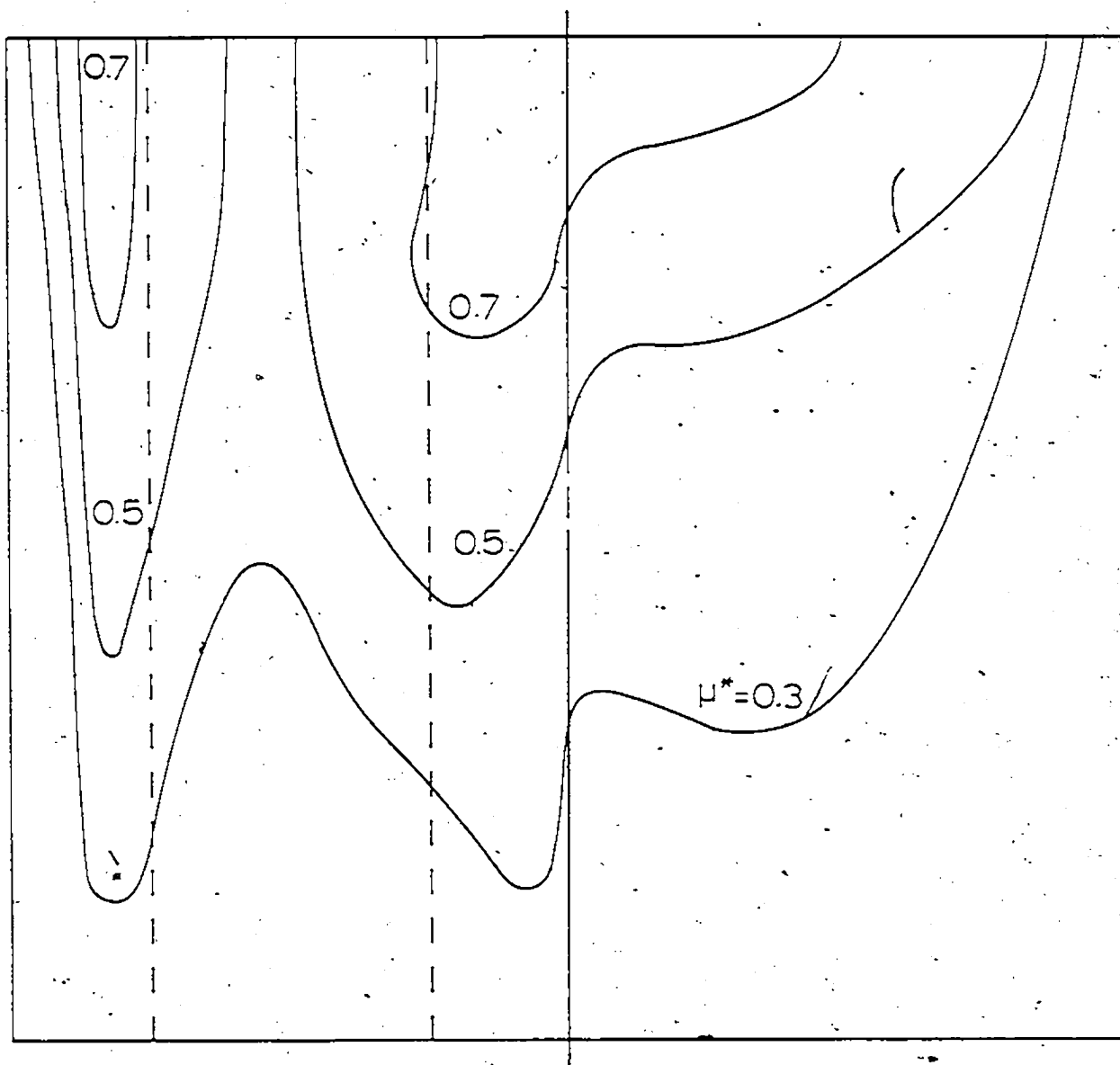


Figure 28 Predicted effective viscosity distribution in vessel 3.
Non-slip off-centered jet.

$$\mu^* = \mu_{\text{eff}}/\mu_{\text{max}}, \quad \mu_{\text{max}} = 225 \text{ N-s/m}^2, \quad \mu_{\text{max}}/\mu_{\text{lam}} = 45000$$

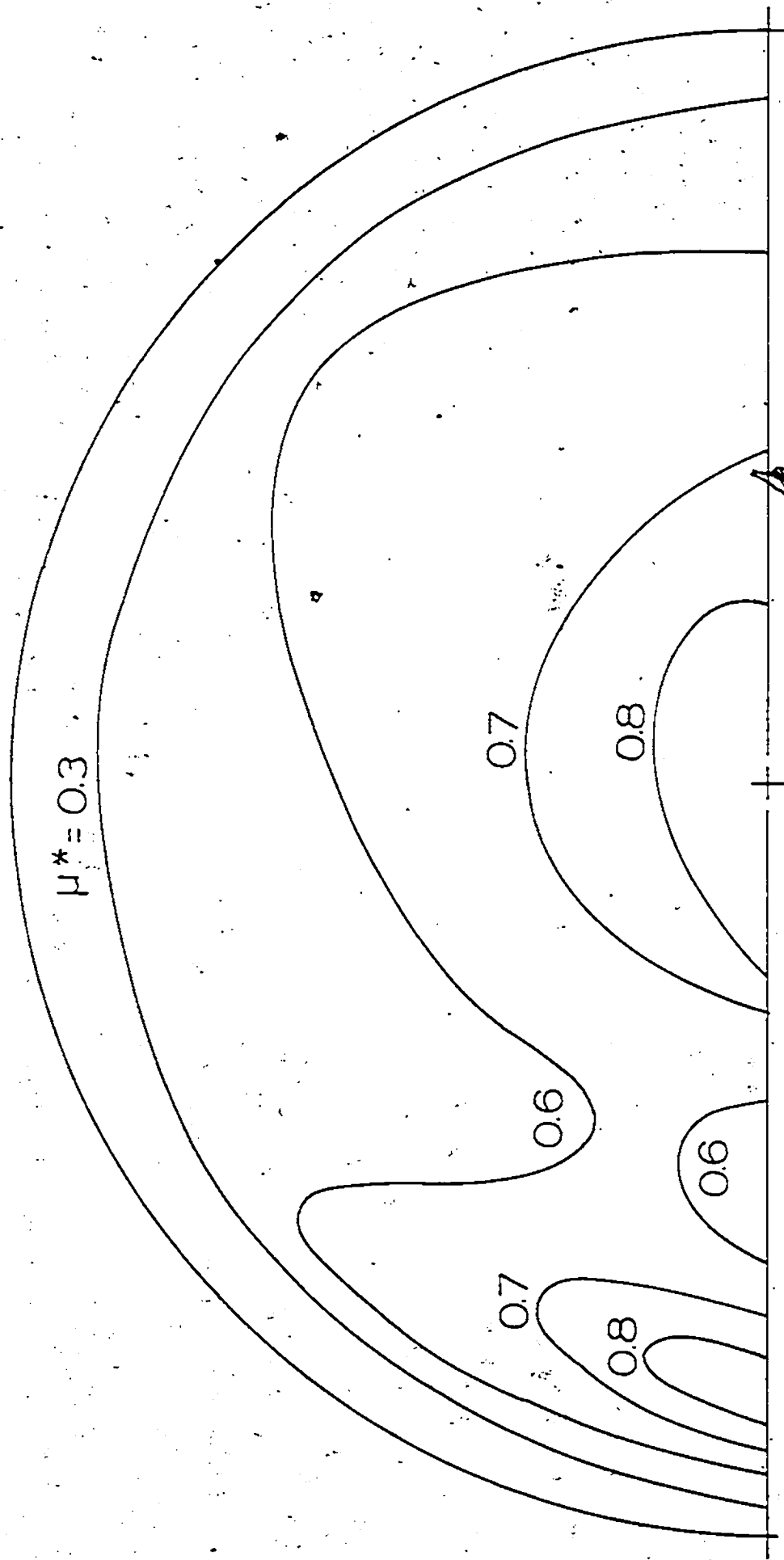


Figure 29 Predicted effective viscosity distribution in vessel 3. Non-slip off-centered

jet. (Half cross-section through the top of the vessel is illustrated)

$$\mu^* = \mu_{\text{eff}} / \mu_{\text{max}}^* \quad \mu_{\text{max}}^* = 225 \text{ N-s/m}^2, \quad \mu_{\text{max}} / \mu_{\text{lam}} = 45000$$

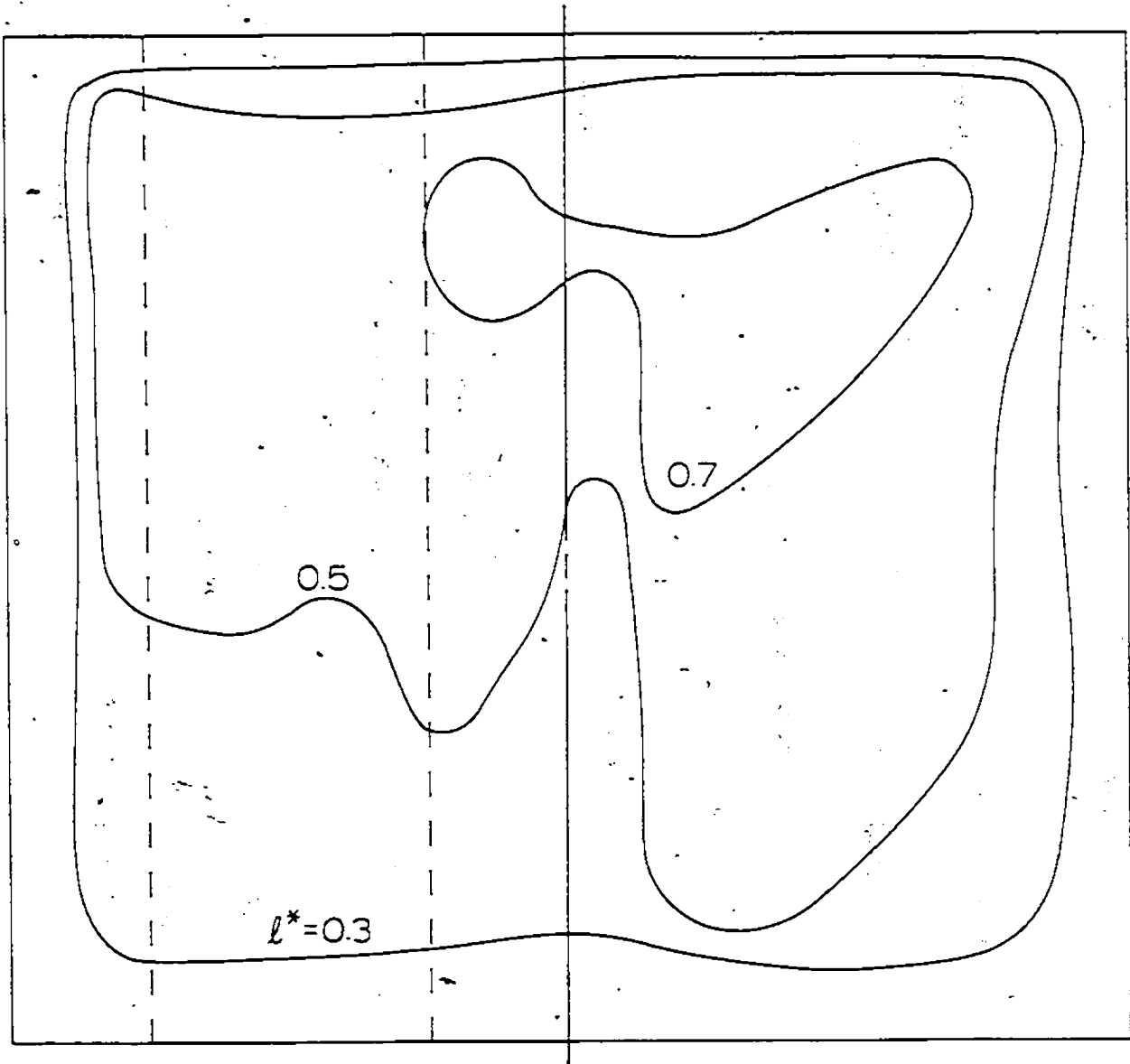


Figure 30 Predicted characteristic length scale distribution in vessel 3. Non-slip off-centered jet.

$$l^* = l/l_{\max}, \quad l_{\max}/R = 0.772$$

$\overleftarrow{0.3}$ $\text{VEL} > 0.1$
 $\overleftarrow{0.1}$ $0.1 > \text{VEL} > 0.03$
 $\overleftarrow{0.03}$ $0.03 > \text{VEL} > 0.01$

$\overleftarrow{0.01}$ $0.01 > \text{VEL} > 0.003$
 $\overleftarrow{0.003}$ $0.003 > \text{VEL}$

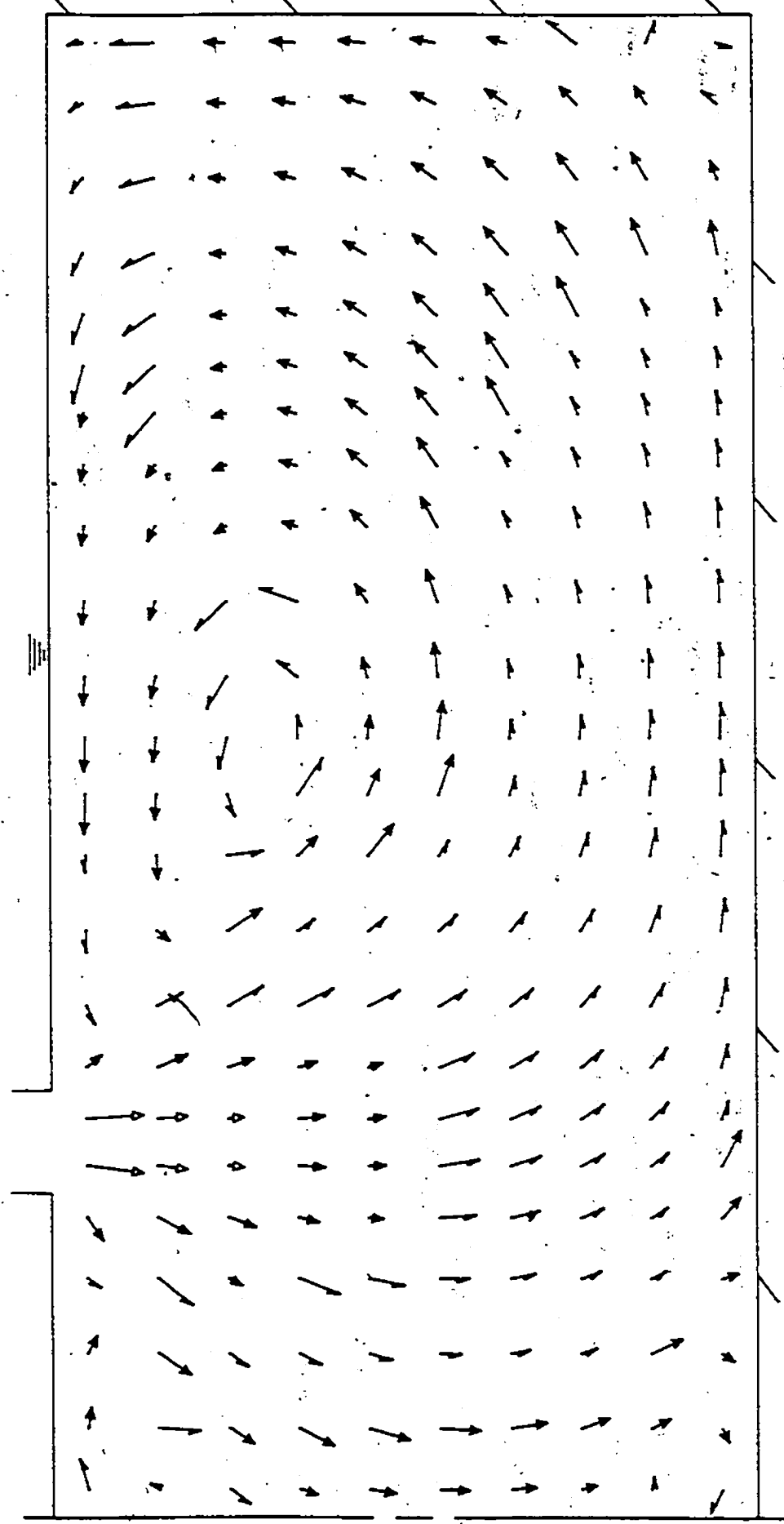


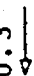
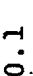
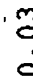
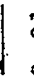
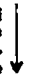
Figure 31 Predicted velocity distribution. Plane, IX=19 (see Fig. 7), in the T-shaped tundish. Computed values in m/s.

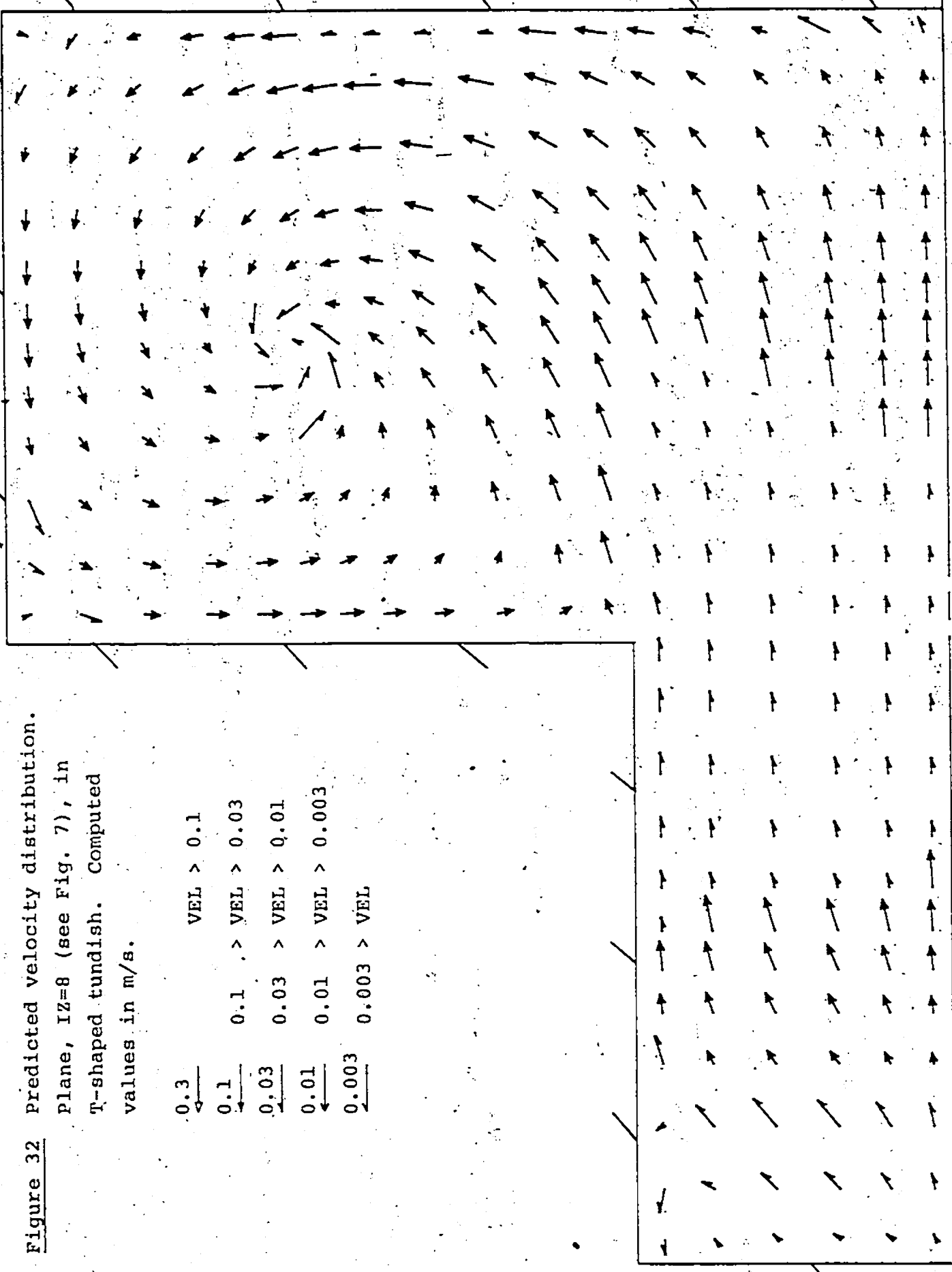
Figure 32 Predicted velocity distribution.

Plane, IZ=8 (see Fig. 7), in

T-shaped tundish. Computed

values in m/s.

- 0.3  VEL > 0.1
- 0.1  > VEL > 0.03
- 0.03  > VEL > 0.01
- 0.01  > VEL > 0.003
- 0.003  > VEL



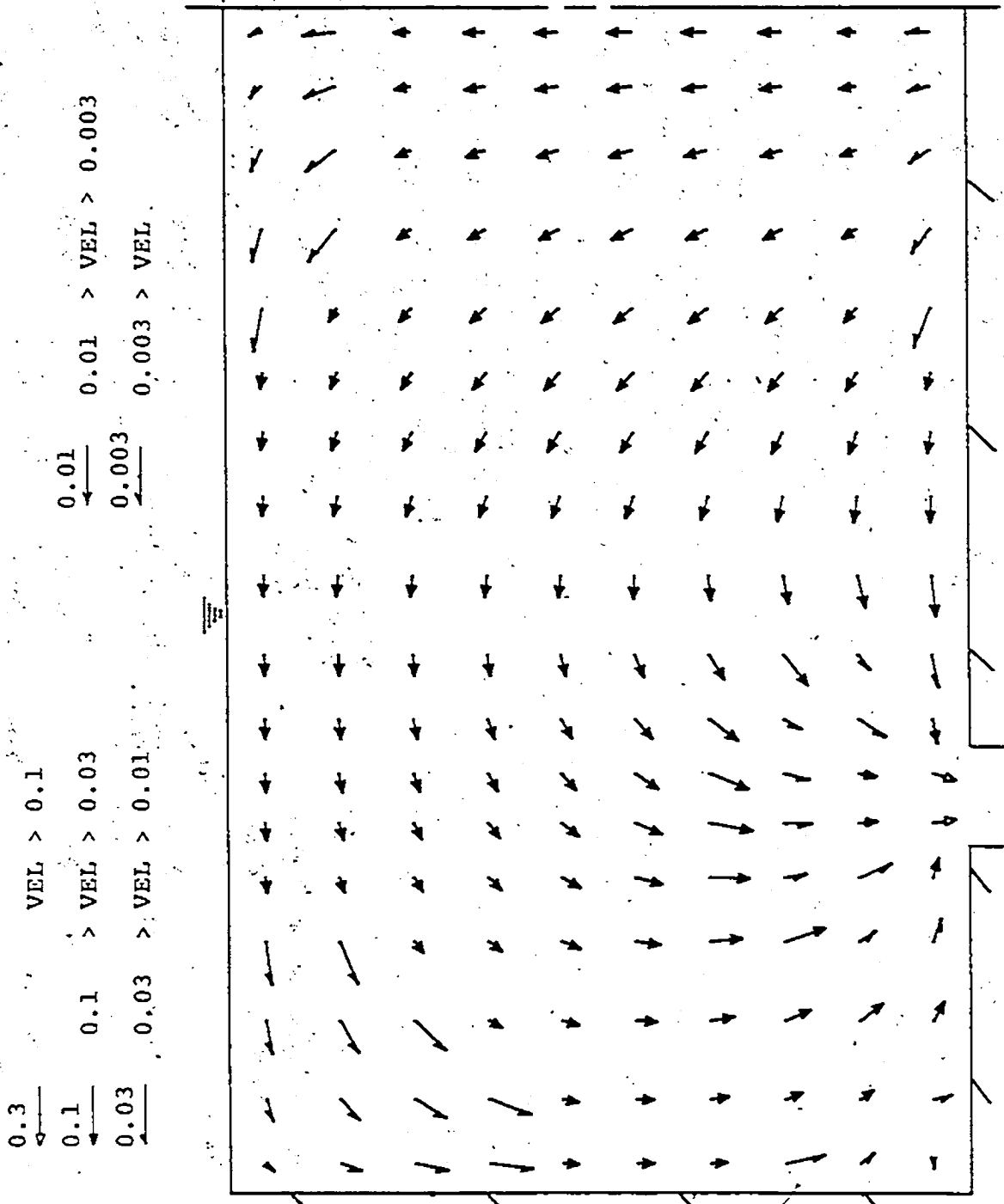


Figure 33 Predicted velocity distribution. Plane, $Y=20$ (see Fig. 7), in the T-shaped tundish. Computed values in m/s.

$\overline{0.3}$ $\overline{0.1}$ $\overline{0.03}$ $\overline{0.01}$ $\overline{0.003}$ $\overline{0.001}$
 $\text{VEL} > 0.1$ $> \text{VEL} > 0.03$ $> \text{VEL} > 0.01$

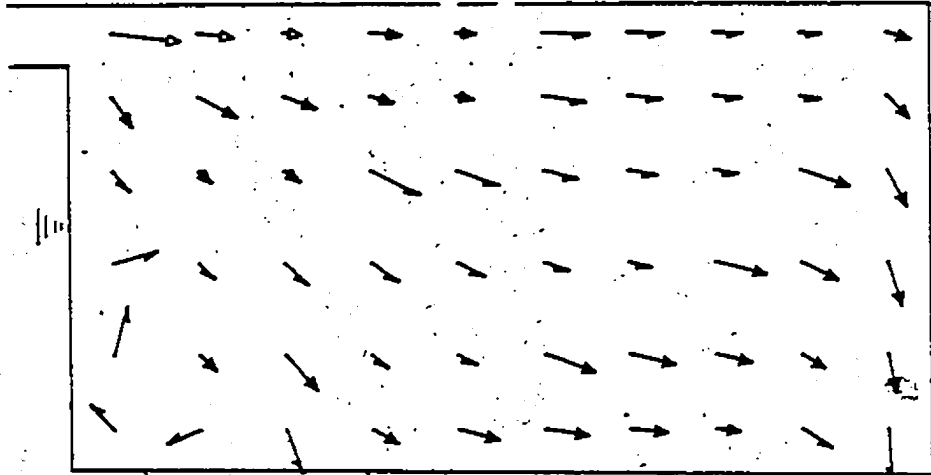


Figure 35 Predicted velocity distribution. Plane, IY=8 (see Fig.7), in the T-shaped tundish. Computed values in m/s.

$\overline{0.01}$ $\overline{0.003}$ $\overline{0.001}$
 $0.01 > \text{VEL} > 0.003$ $0.003 > \text{VEL}$

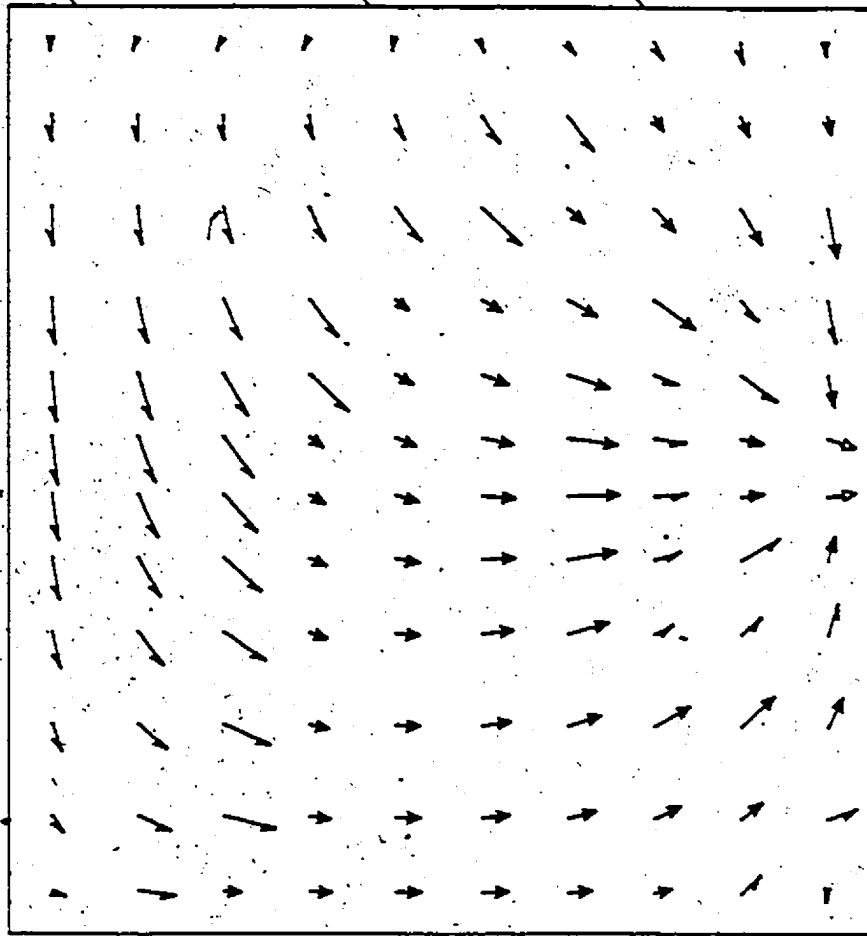


Figure 34 Predicted velocity distribution. Plane, IX=7 (see Fig.7), in the T-shaped tundish. Computed values in m/s.

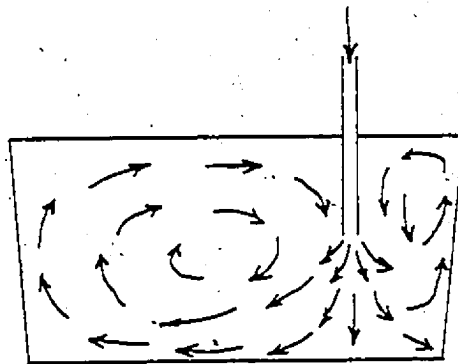
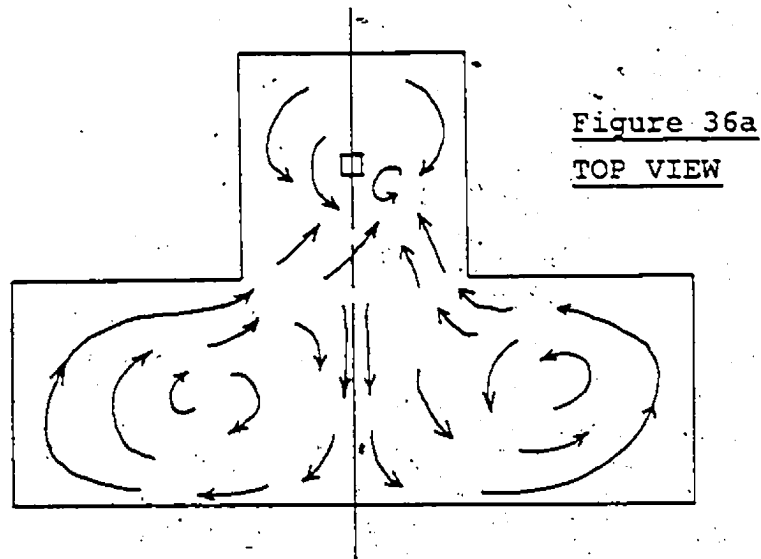


Figure 36 Experimental flow directions in the T-shaped tundish (Chushao Xu, McGill University)

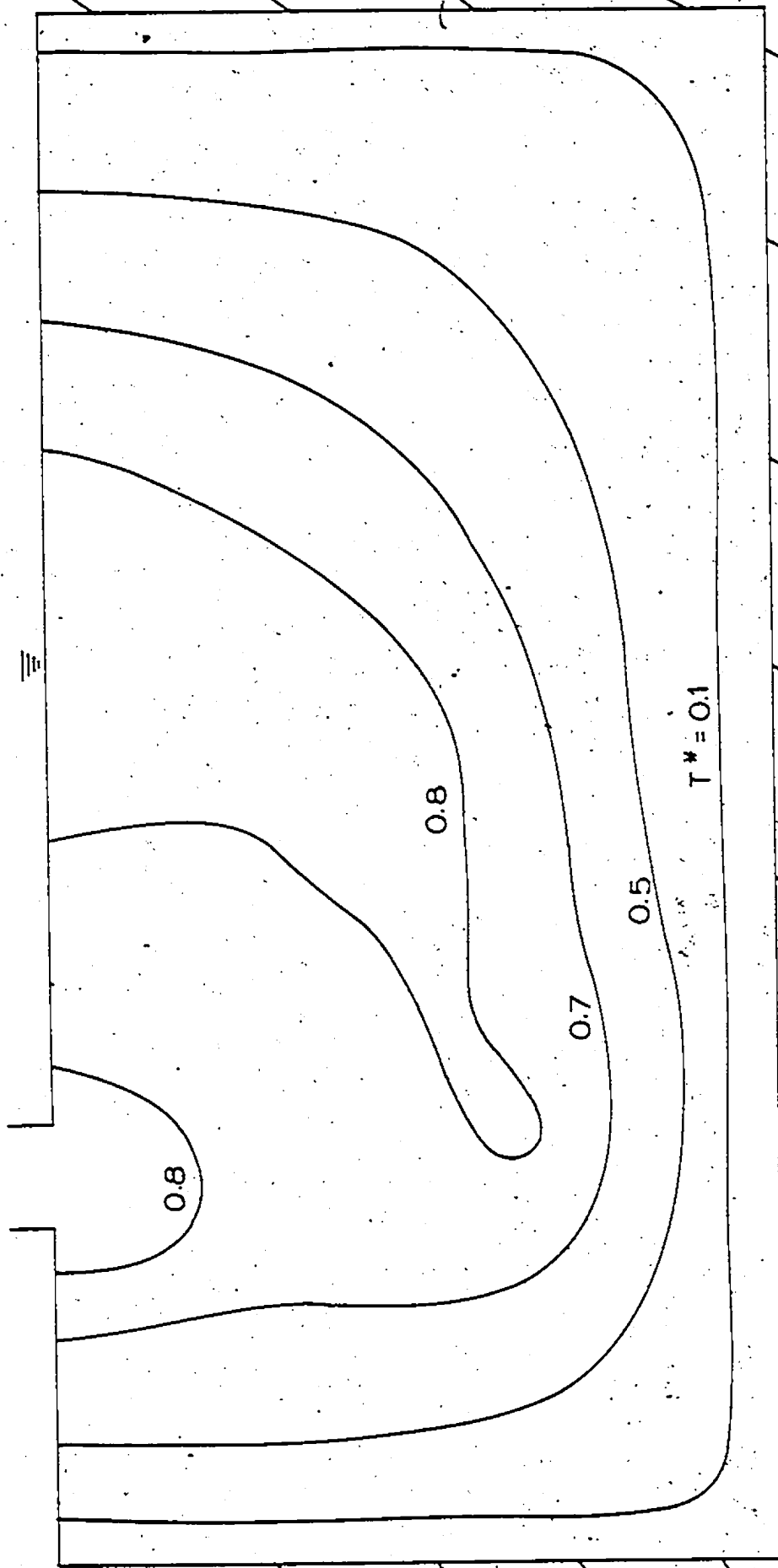
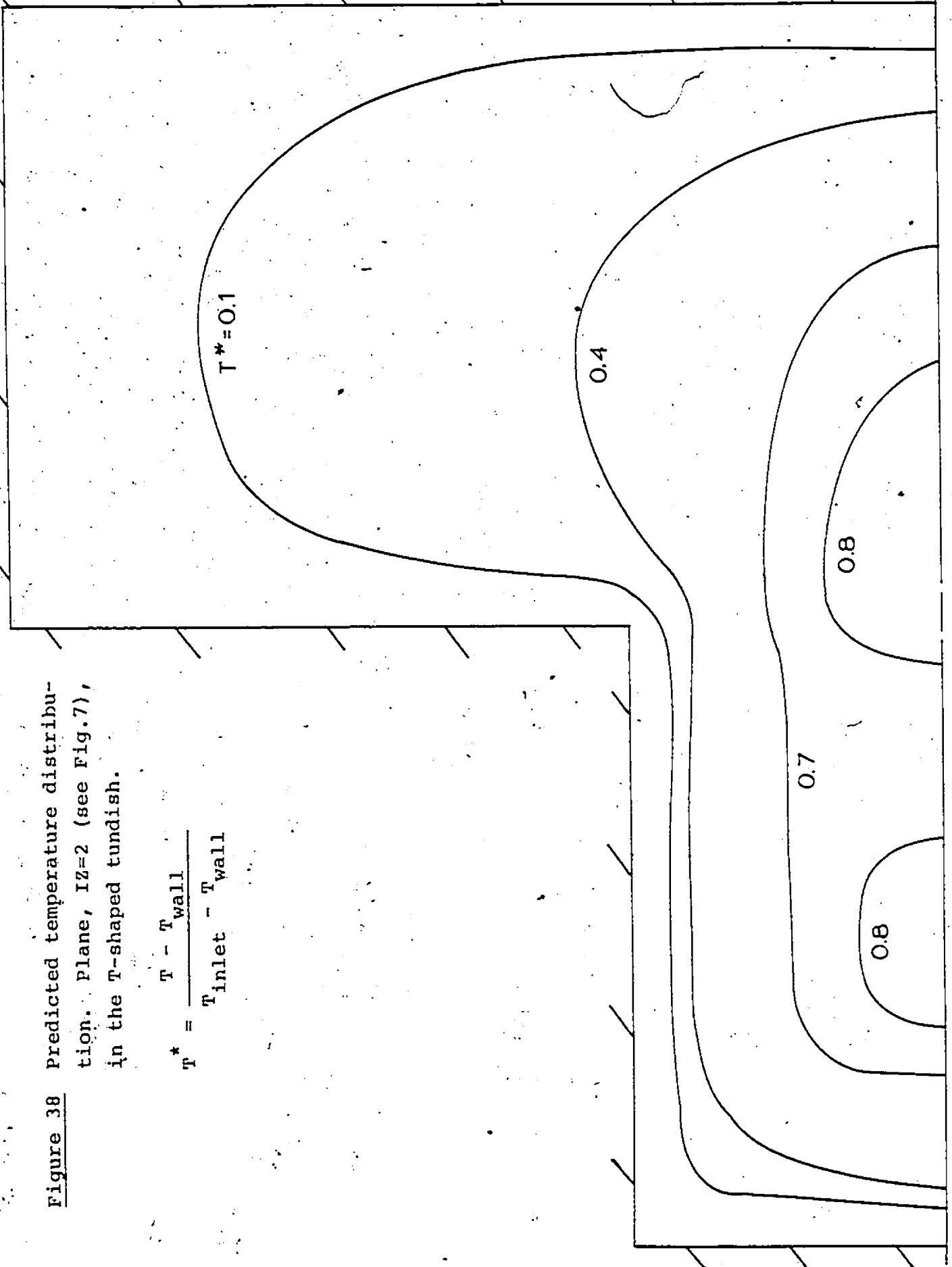


Figure 37. Predicted temperature distribution. Plane, IX=19
 (see Fig. 7), in the T-shaped tundish.

$$T^* = \frac{T - T_{\text{wall}}}{T_{\text{inlet}} - T_{\text{wall}}}$$

Figure 38 Predicted temperature distribution. Plane, IZ=2 (see Fig.7), in the T-shaped tundish.

$$T^* = \frac{T - T_{\text{wall}}}{T_{\text{inlet}} - T_{\text{wall}}}$$



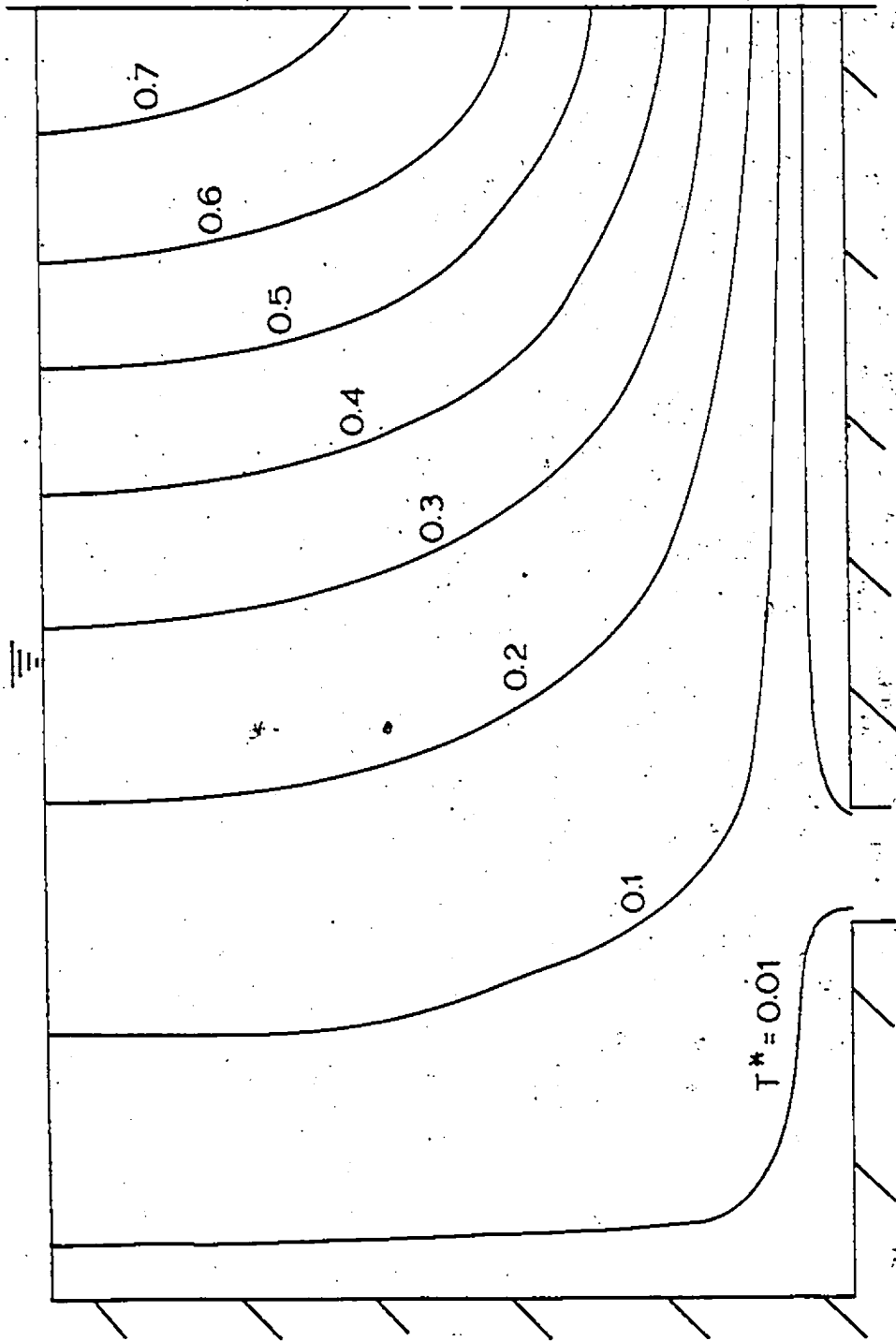


Figure 39 Predicted temperature distribution. Plane, $T^* = \frac{T - T_{wall}}{T_{inlet} - T_{wall}}$
IY=20 (see Fig. 7), in the T-shaped tundish.

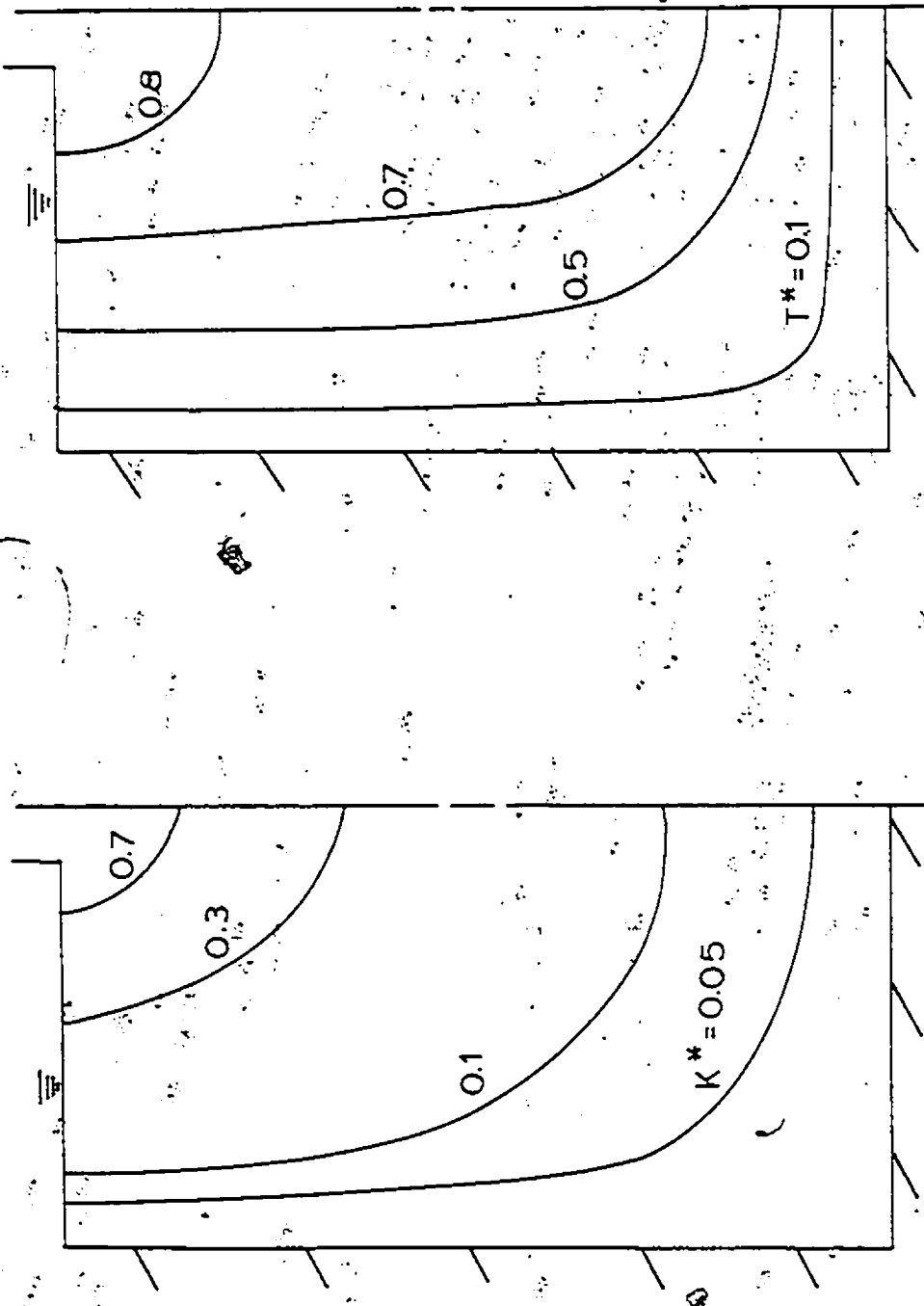


Figure 40 Predicted turbulence kinetic energy distribution. Plane, IY=8 (see Fig. 7), in the T-shaped tundish.

$$K^* = K/K_{max} \quad K_{max} = 0.184 \text{ m}^2/\text{s}^2$$

$$K_{max}/(w_{inlet})^2 = 0.736$$

Figure 41 Predicted temperature distribution. Plane, IY=8 (see Fig. 7), in the T-shaped tundish.

$$T^* = \frac{T - T_{wall}}{T_{inlet} - T_{wall}}$$

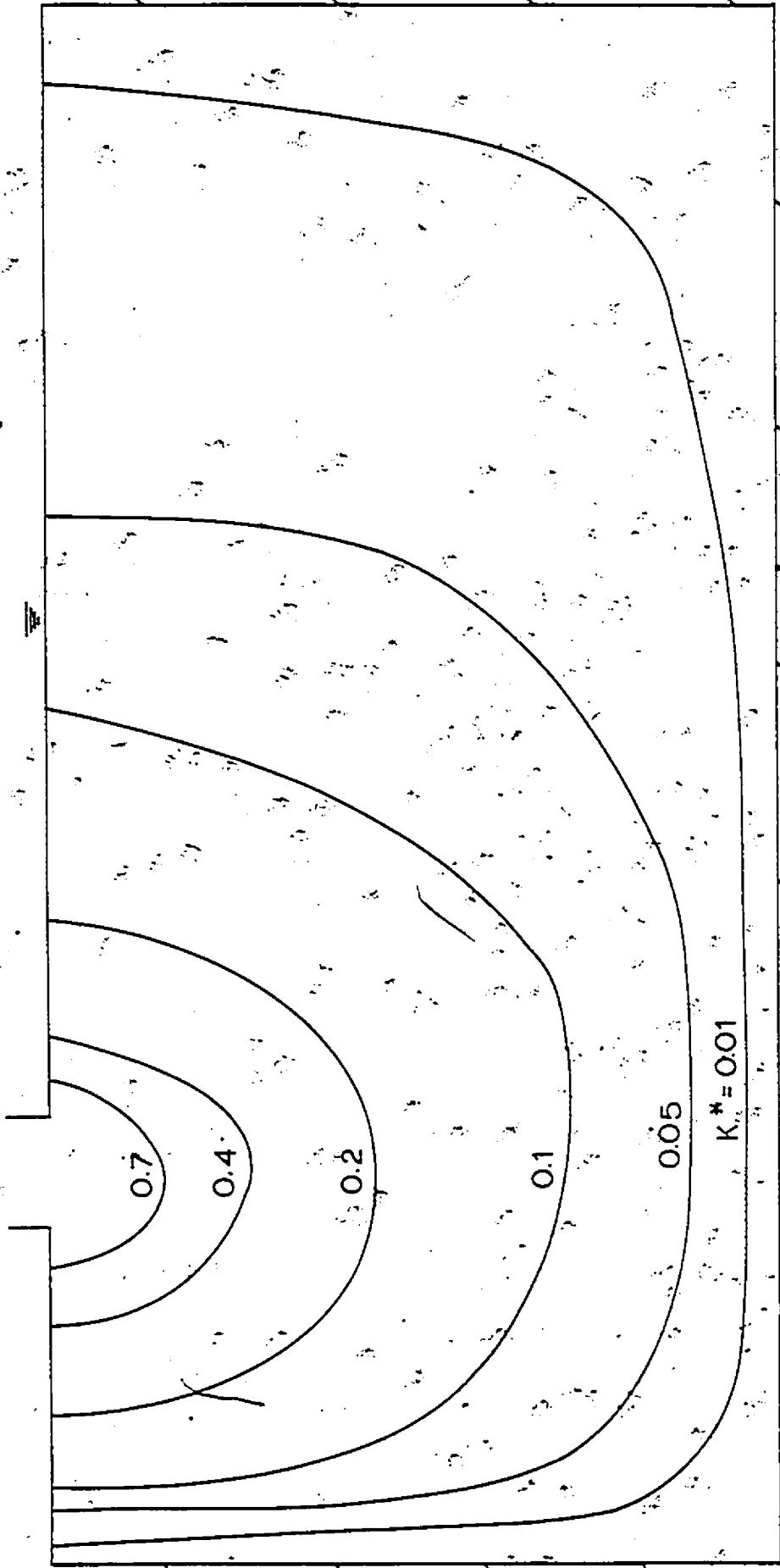


Figure 42 Predicted turbulence kinetic energy distribution. Plane, IX=9
 (see Fig. 7), in the T-shaped tundish.

$$K^* = K/K_{\max} \quad K_{\max} = 0.184 \text{ m}^2/\text{s}^2$$

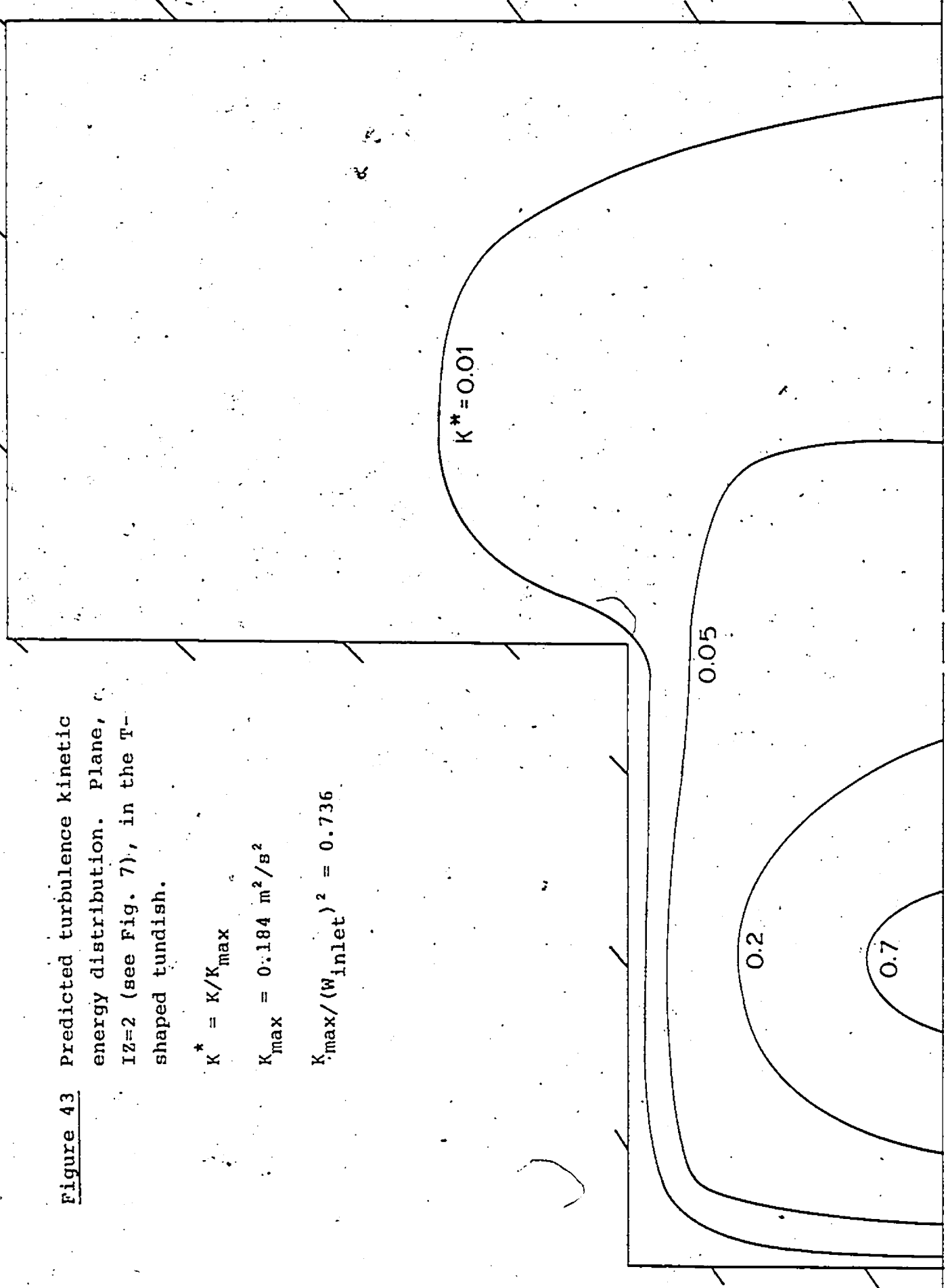
$$K_{\max}/(\bar{W}_{\text{inlet}})^2 = 0.736$$

Figure 43 Predicted turbulence kinetic energy distribution. Plane, IZ=2 (see Fig. 7), in the T-shaped tundish.

$$K^* = K/K_{max}$$

$$K_{max} = 0.184 \text{ m}^2/\text{s}^2$$

$$K_{max}/(W_{inlet})^2 = 0.736$$



BIBLIOGRAPHY

1. Patankar, S.V. and Spalding, D.B. (1972). "A Calculation Procedure for Heat, Mass and Momentum Transfer in Three-Dimensional Parabolic Flows", Int. J. Heat Mass Transfer, Vol. 15, pp. 1787.
2. Patankar, S.V. and Spalding, D.B. (1967). "Heat and Mass Transfer in Boundary Layers", Morgan-Grampian Press, London.
3. Patankar, S.V. and Spalding, D.B. (1970). "Heat and Mass Transfer in Boundary Layers", Intertext Books, London.
4. Gosman, A.D., Pun, W.M., Runchal, A.K., Spalding, D.B. and Wolfshtein, M. (1969). "Heat and Mass Transfer in Recirculating Flows", Academic Press, London.
5. Harlow, F.H. and Welch, J.E. (1965). "Numerical Calculation of Time-Dependent Viscous Incompressible Flow of Fluid with Free Surface", Phys. of Fluids, Vol. 8, pp. 2182.
6. Amsden, A.A. and Harlow, F.H. (1970). "The SMAC Method: A Numerical Technique for Calculating Incompressible Fluid Flows", Los Alamos Scientific Laboratory, LA-4370.
7. Gosman, A.D. and Spalding, D.B. (1971). "The Prediction of Confined Three-Dimensional Boundary Layers", Proc. of Conf. on Internal Flows, University of Salford.
8. Pratap, V.S. and Spalding, D.B. (1976). "Fluid Flow and Heat Transfer in Three-Dimensional Duct Flows", Int. J. Heat Mass Transfer, Vol. 19, pp. 1183-1188.
9. Majumdar, A.K., Pratap, V.S. and Spalding, D.B. (1977). "Numerical Computation of Flow in Rotating Ducts", J. of Fluids Engineering, Trans. of ASME, pp. 148.
10. Markatos, N.C.G., Spalding, D.B., Tatchell, D.G. and Vlachos, N. (1978). "A Solution Method for Three-Dimensional Turbulent Boundary Layers on Bodies of Arbitrary Shapes", Computer Methods in Applied Mechanics and Engineering, Vol. 15, pp. 161-174.

11. Pollard, A. and Spalding, D.B. (1978). "The Prediction of the Three-Dimensional Turbulent Flow Field in a Flow-Splitting Tee-Junction", *Computer Methods in Applied Mechanics and Engineering*, Vol. 13, pp. 293-306.
12. Patankar, S.V. (1980). "Numerical Heat Transfer and Fluid Flow", *Series in Computational Methods in Mechanics and Thermal Sciences*, Hemisphere Publishing Corporation.
13. Rodi, W. and Srivatsa, S.K. (1980). "A Local Elliptic Calculation Procedure for Three-Dimensional Flows and Its Application to a Jet in a Cross-Flow", *Computer Methods in Applied Mechanics and Engineering*, Vol. 23, pp. 67-83.
14. Serge-Eldin, M.A. and Spalding, D.B. (1981). "A Computational Procedure for Three-Dimensional Recirculating Flows Inside Can Combustors", in "Numerical Methods in Heat Transfer", edited by Lewis, R.W., Morgan, K. and Zienkiewics, O.C., John Wiley & Sons Ltd.
15. Launder, B.E. and Spalding, D.B. (1974). "The Numerical Computation of Turbulent Flows", *Computer Methods in Applied Mechanics and Engineering*, Vol. 3, pp. 269-289.
16. Spalding, D.B. (1972). "A Novel Finite-Difference Formulation for Differential Equation Involving Both First and Second Derivatives", *Int. J. Num. Methods in Eng.*, Vol. 4.
17. Leschziner, M.A. (1980). "Practical Evaluation of Three Finite Difference Schemes for the Computation of Steady-State Recirculating Flows", *Computer Methods in Applied Mechanics and Engineering*, Vol. 23, pp. 293-312.
18. Prandtl, L. (1925). "Über die ausgebildete Turbulenz". *ZAMM*. Vol. 5, pp. 136.
19. Prandtl, L. (1945). "Über ein neues Formel-System für die ausgebildete Turbulenz", *Nachr. Akad. Wiss., Göttingen, Math.-Phys. K.L.*, pp. 6.
20. Bradshaw, P., Ferriss, D.H. and Atwell, N.P. (1967). "Calculation of Boundary-Layer Development Using the Turbulent Energy Equation", *J. Fluid Mech.*, Vol. 28, Part 3, pp.593-616.

21. Kolmogorov, A.N. (1942). "Equations of Turbulent Motion in an Incompressible Fluid", Izv. Akad. Nauk. SSSR, Sexia fizicheska VI, No. 1-2, pp. 56-58. Also Imperial College, Mech. Eng. Report ON/6 (1968).
22. Harlow, F.H. and Nakayama, P.I. (1968). "Transport Turbulence Energy Decay Rate", Los Alamos Sci. Lab., Univ. California Report, LA-3854.
23. Spalding, D.B. (1970). "The Prediction of Two-Dimensional Steady Turbulent Flows", Imperial College, Heat Transfer Section Rep. EF/TN/A/16.
24. Jones, W.P. and Launder, D.B. (1972). "The Calculation of Low-Reynolds-Number Phenomena with a Two-Equation Model of Turbulence", Int. J. Heat Mass Transfer, Vol. 16, pp. 1119-1130.
25. Launder, B.E. and Spalding, D.B. (1972). "Mathematical Models of Turbulence", Academic Press, London.
26. Hanjalic, K. and Launder, B.E. (1972). "A Reynolds Stress Model of Turbulence and its Application to Thin Shear Flows", J. Fluid Mech., Vol. 52, Part 4, pp. 609-638.
27. Van Driest, E.R. (1957). "On Turbulent Flow near a Wall", J. Aero. Sci., 23, 1007.
28. Chou, P.Y. (1945). "On the Velocity Correlations and the Solution of the Equations of Turbulent Fluctuation", Quart. Appl. Math., Vol. 3, pp. 38.
29. Widdowson, P. (1981). "Ladle Composition and Temperature Control", Ironmaking and Steelmaking, Vol. 13, pp. 293-306.
30. Guthrie, R.I.L. (1982). "The Role of Fluid Mechanics in Ladle Metallurgy", I&SM, Jan., pp. 41-45.
31. The Iron & Steel Institute, special report eighty-nine. "Continuous Casting of Steel", Report of the Proceeding of the Autumn General Meeting in Nov. 1975.
32. Leclerc, J., Martin, R. and Amory, D. (1973). "Comments on Steelmaking Practice for a Continuous Casting of Slabs for Plates and Sheets", AIME Open Hearth Conf. Proc., Vol. 56, pp. 218-235.

33. Relander, K., Lounamaa, K. and Lindholm, T. (1979). "Continuous Slab Casting at Raabe Steel Works", Iron-making and Steelmaking, No. 5, pp. 245-250.
34. Whittaker, D.A. and Palmer, A.R. (1981). "Ladle Metallurgy at the Well and Plant of Atlas Steels", I&SM, June, pp. 31-35.
35. Grip, C.E., Tivelius, B., Sohlgren, T. and Gossas, P. (1981). "Ladle Metallurgy in SSAB (Oxelosund, Domnarvet and Lulea)", I&SM, Feb., pp. 33-39.
36. Hlinka, J.W. (1975). "Water Model for the Quantitative Simulation of the Heat and Fluid Flow in Liquid-Steel Refractory Systems", in "Mathematical Process Models in Iron- and Steelmaking", The Metals Society, London, pp. 157-164.
37. Robertson, A.D. and Sheridan, S.T. (1970). "Water Modelling of Liquid Steel at Swinden Laboratories", J. of the Iron and Steel Institute, July, pp. 625-632.
38. Hlinka, J.W. and Miller, T.W. (1970). "Temperature Loss in Liquid Steel-Refractory Systems", Iron and Steel Engineer, Aug., pp. 123-133.
39. Salcudean, M. and Guthrie, R.I.L. (1979). "A Three-Dimensional Representation of Fluid Flow Induced in Ladles or Holding Vessels by the Action of Liquid Metal Jets", Metallurgical Transactions B, Vol. 10B, pp. 423-428.
40. Salcudean, M. and Guthrie, R.I.L. (1982). "Non Symmetrical Flows in Liquid Metal Systems", Transaction ISIJ, Vol. 22, pp. 22-29.
41. Issa, R.I. and Gosman, A.D. (1981). "The Computation of Three-Dimensional Turbulent Two-Phase Flows in Mixer Vessels", in "Numerical Methods in Laminar and Turbulent Flow", edited by Taylor, C. and Schrefler, B.A., Pineridge Press, Swansea, U.K.
42. Alberty, R. and Leclercq, A. (1975). "Heat Losses from Liquid Steel in the Ladle and in the Tundish of a Continuous-casting Installation", in "Mathematical Process Models in Iron- and Steelmaking", The Metals Society, London, pp. 151-156.

43. Szekely, J. and Yadaya, R.T. (1975). "Modelling of the Flow Field in the Mould Region of Continuous-Casting Systems", in "Mathematical Process Models in Iron- and Steelmaking", The Metals Society, London, pp. 165-173.
44. Brimacombe, J.K., Lait, J.E. and Weinberg, F. (1975). "Application of Mathematical Models to Predict Pool Profiles in Continuously Cast Steel", in "Mathematical Process Models in Iron- and Steelmaking", The Metals Society, London, pp. 174-186.
45. Spencer, S., Carless, P. and Magee, E. (1981). "Mathematical Model for Simulation of Solidification and Cooling of Cast Rods", Ironmaking and Steelmaking, No. 3, pp. 129-135.
46. Stanek and Szekely, J. (1976). "A Mathematical Model of the Closed Mold (Watts) Horizontal Continuous Casting Process", Metallurgical Transactions B, Vol. 7B, Dec., pp. 619-630.
47. Asai, S. and Szekely, J. (1975). "Turbulent Flow and its Effects in Continuous Casting", Ironmaking and Steelmaking (Quarterly), No. 3, pp. 205-213.
48. Mizikar, E.A. (1967). "Mathematical Heat Transfer Model for Solidification of Continuously Cast Slabs", Transactions of the Metallurgical Society of AIME, Vol. 239, pp. 1747-1753.
49. Perkins, A. and Iring, W.R. (1975). "Two-Dimensional Heat Transfer Model for Continuous Casting of Steel", in "Mathematical Process Models in Iron- and Steelmaking", The Metals Society, London, pp. 187-199.
50. Szekely, J. and Chang, C.W. (1976). "Melt Velocities, Temperature Profiles and Scrap Melting Kinetics in Induction Furnaces", Electric Furnace Proceedings, pp. 213-220.
51. Szekely, J., Chang, C.W. and Ryan, R.E. (1977). "The Measurement and Prediction of the Melt Velocities in a Turbulent, Electromagnetically Driven Recirculating Low Melting Alloy Systems", Metallurgical Transaction B, Vol. 8B, June, pp. 333-338.
52. El-Kaddah, N. and Szekely, J. (1981). "Mathematical Model for Desulphurization Kinetics in Argon-Stirred Ladles", Ironmaking and Steelmaking, No. 6, pp. 269-278.

53. Miyashita, Y., Miyahara, S., Ueno, Y., Ishikawa, M. and Honda, A. (1981). "Development and Metallurgical Analysis of the Horizontal Continuous Casting", I&SM, Vol. 22, Aug., pp. 22-28.
54. Szekely, J., Wang, H.J. and Kiser, K.M. (1976). "Flow Pattern Velocity and Turbulence Energy Measurements and Predictions in a Water Model of an Argon-Stirred Ladle", Metallurgical Transactions B, Vol. 7B, June, pp. 287-295.
55. Deb Roy, T., Majumdar, A.K., and Spalding, D.B. (1978). "Numerical Prediction of Recirculation Flows with Free Convection Encountered in Gas-Agitated Reactors", Appl. Math. Modelling, Vol. 2, pp. 146-150.
56. Szekely, J., El-Kaddah, N.H., and Grevet, J.H. (1980). "Flow Phenomena in Argon-Stirred Ladles Room Temperature Measurements and Analysis", Scaninject II Conference preprint, Lulea, Sweden, pp. 5: 1-32.
57. Pun, W.M. and Spalding, D.B. (1977). Report HTS 76/2 Heat Transfer Section, Imperial College of Science and Technology, London.
58. Salcudean, M., Low, C.H., Hurda, A. and Guthrie, R.I.L. (1982). "Three-Dimensional Analysis of Recirculatory Flows in Gas Agitated Reactors", Chemical Engineering Communications, in print.
59. Salcudean, M. and Wong, R.C.L. (1982). "Computation of Steady-State Multi-Dimensional Flows in Gas-Stirred Reactors", to be published.
60. Hinze, J.O. (1975). "Turbulence", McGraw Hill Series in Mechanical Engineering, McGraw Hill Inc..
61. Ideriah, F.J.K., "Turbulent Natural and Forced Convection in Plumes and Cavities", PhD. Thesis, Faculty of Engineering, University of London, June, 1977.
62. Abdelrehim, Z.E. (1979). "Heat Transfer in Turbulent Recirculatory Flows Affected by Buoyancy Forces in Rectangular Cavities", Master Thesis, Department of Mechanical Engineering, University of Ottawa.
63. Roache, P.J. (1972). "Computational Fluid Dynamics", Hermosa Publishers, Albuquerque.

64. Sahai, Y., Guthrie, R.I.L. (1982). "Hydrodynamics of Gas Stirred Melts - Part I", to be published.
65. Heaslip, L.J. (1981). "Water Model Study of Various Tundish Designs", interim report for Atlas Steels Limited.

Appendix A

Derivation of Momentum Equations

By applying the expression for Reynolds stresses (equation 7) to the momentum equation (5), the U-momentum equation for steady flow of an incompressible fluid without body force, can be expressed in cylindrical coordinates as:

$$\begin{aligned}
 v \frac{\partial(\rho U)}{\partial r} + \frac{U}{r} \frac{\partial(\rho U)}{\partial \theta} + \frac{\rho UV}{r} + w \frac{\partial(\rho U)}{\partial z} &= - \frac{1}{r} \frac{\partial P}{\partial \theta} \\
 + \frac{\partial}{\partial r} \left[\frac{1}{r} \frac{\partial}{\partial r} (r \mu_{\text{eff}} U) \right] + \frac{1}{r^2} \frac{\partial^2 (\mu_{\text{eff}} U)}{\partial \theta^2} + \frac{2}{r^2} \frac{\partial (\mu_{\text{eff}} V)}{\partial \theta} \\
 + \frac{\partial^2 (\mu_{\text{eff}} U)}{\partial z^2} + \frac{1}{r} \frac{\partial}{\partial r} \left[\mu_{\text{eff}} r \left(\frac{1}{r} \frac{\partial V}{\partial \theta} - \frac{U}{r} \right) \right] + \frac{\partial}{r \partial \theta} \left[\frac{\mu_{\text{eff}}}{r} \left(\frac{\partial U}{\partial \theta} \right) \right] \\
 + \frac{\partial}{\partial z} \left(\frac{\mu_{\text{eff}}}{r} \frac{\partial w}{\partial \theta} \right) + \frac{\mu_{\text{eff}}}{r} \left(\frac{\partial U}{\partial r} + \frac{\partial V}{r \partial \theta} \right) & \quad (A.1)
 \end{aligned}$$

By regrouping some of the terms, equation (A.1) becomes

$$\begin{aligned}
 \frac{1}{r} \frac{\partial}{\partial r} (r \rho UV) + \frac{1}{r} \frac{\partial}{\partial \theta} (\rho UU) + \frac{\partial}{\partial z} (\rho UW) \\
 - \left\{ U \left[\frac{\partial(\rho V)}{\partial r} + \frac{1}{r} \frac{\partial(\rho U)}{\partial \theta} + \frac{\partial(\rho W)}{\partial z} + \frac{\rho V}{r} \right] \right\} - \frac{1}{r} \frac{\partial}{\partial r} (\mu_{\text{eff}} r \frac{\partial U}{\partial r}) \\
 = 0 \\
 - \frac{1}{r} \frac{\partial}{\partial \theta} (\mu_{\text{eff}} \frac{\partial U}{r \partial \theta}) - \frac{\partial}{\partial z} (\mu_{\text{eff}} \frac{\partial U}{\partial z}) - \frac{\mu_{\text{eff}}}{r} \frac{\partial^2 w}{\partial \theta \partial z} \\
 - \frac{1}{r} \frac{\partial}{\partial r} \left[\mu_{\text{eff}} r \left(\frac{1}{r} \frac{\partial V}{\partial \theta} - \frac{U}{r} \right) \right] + \frac{\rho UV}{r} - \frac{\partial}{r \partial \theta} \left[\frac{\mu_{\text{eff}}}{r} \left(\frac{\partial U}{\partial \theta} - 2V \right) \right] \\
 - \frac{\mu_{\text{eff}}}{r} \left(\frac{\partial U}{\partial r} + \frac{\partial V}{r \partial \theta} - \frac{U}{r} \right) + \frac{\partial P}{r \partial \theta} = 0 & \quad (A.2)
 \end{aligned}$$

Since the continuity equation states that

$$\frac{\partial(\rho V)}{\partial r} + \frac{1}{r} \frac{\partial(\rho U)}{\partial \theta} + \frac{\partial(\rho W)}{\partial z} + \frac{\rho V}{r} = 0$$

then equation (A.2) can be reduced to equation (15), which in turn can be easily put into the general form as shown in equation (19). Similar procedures are applied to the V- and W-momentum equations in order to obtain the form present in equations (13) and (14).

Appendix B

Tridiagonal Matrix Algorithm (TDMA) [62]

For each grid node on the y-direction line, the algebraic equation can be expressed as:

$$\underbrace{\left(\sum_{j=e,w,n,s,h,l} a_j - Sp \right)}_{\text{}} \phi_p = \underbrace{a_n \phi_N^* + a_s \phi_S + a_e \phi_E + a_w \phi_W}_{\text{}} + \underbrace{a_h \phi_H + a_l \phi_L + Su}_{\text{}} \quad (\text{B.1})$$

The underlined quantities, which contain ϕ 's on the neighbouring lines, are assumed to be known. For a line of NY-2 nodes, equation B.1 can be expanded to form a system of NY-2 equations of the form

$$d_i \phi_i = a_i \phi_{i+1} + b_i \phi_{i-1} + c_i$$

$$\text{or } -a_i \phi_{i+1} + d_i \phi_i - b_i \phi_{i-1} = c_i, \quad i=2,3,\dots, \text{NY}-1 \quad (\text{B.2})$$

$$\text{where } d_i = \sum_j a_j - Sp$$

$$a_i = a_n$$

$$b_i = a_s$$

(B.3)

$$c_i = a_e \phi_E + a_w \phi_W + a_h \phi_H + a_l \phi_L + Su$$

and the values of ϕ_1 and ϕ_{NY} are specified from the boundary condition.

recursive formula for B_j , T_j and A_j are obtained

$$\begin{array}{lll}
 T_2 = d_2 & & A_2 = a_2/T_2 \\
 B_3 = b_3 & T_3 = d_3 - B_3 A_2 & A_3 = a_3/T_3 \\
 \dots & \dots & \dots \\
 B_j = b_j & T_j = d_j - B_j A_{j-1} & A_j = a_j/T_j \\
 \dots & \dots & \dots \\
 B_{NY-2} = b_{NY-2} & T_{NY-2} = d_{NY-2} - B_{NY-2} A_{NY-3} & A_{NY-2} = a_{NY-2}/T_{NY-2} \\
 B_{NY-1} = b_{NY-1} & T_{NY-1} = d_{NY-1} - B_{NY-1} A_{NY-2} & A_{NY-1} = a_{NY-1}/T_{NY-1}
 \end{array}$$

provided $T_j \neq 0$ for $j = 2, 3, \dots, NY-2, NY-1$

The general recursive formulas are

$$\begin{array}{l}
 B_j = b_j \\
 T_j = d_j - B_j A_{j-1} \\
 A_j = a_j/T_j
 \end{array} \tag{B.5}$$

Since $P = LU$, equation $P\phi = Q$ becomes $LU\phi = Q$

Let $C = U\phi$, where

$$C = \begin{bmatrix} C_2 \\ C_3 \\ \dots \\ C_j \\ \dots \\ C_{NY-2} \\ C_{NY-1} \end{bmatrix}$$

then $LU\phi = Q$ becomes $LC = Q$

(B.6)

By expanding the system of equations in (B.6), the C's can be obtained as:

$$C_j = (c_j + b_j c_{j-1}) / T_j ; \quad j = 2, 3, \dots, NY-1$$

$$C_{NY-1} = (c_{NY-1} + b_{NY-1} c_{NY-2}) / T_{NY-1} + a_{NY-1} \phi_{NY} / T_{NY-1} \quad (B.7)$$

with C_1 defined as ϕ_1

With A_{NY-1} defined as in equations (B.5), the second term on the right-hand side of C_{NY-1} becomes $\phi_{NY} A_{NY-1}$

Using the equation $U\phi = C$, the resulting column matrix from the multiplication of U and ϕ is equated to the column matrix C , which gives

$$\begin{aligned} \phi_{NY-1} &= C_{NY-1} \\ \phi_{NY-2} &= C_{NY-2} + A_{NY-2} \phi_{NY-1} \\ &\dots\dots\dots \\ \phi_j &= C_j + A_j \phi_{j+1} \\ &\dots\dots\dots \\ \phi_2 &= C_2 + A_2 \phi_3 \end{aligned}$$

Using the definition of C in (B.7), the above calculations can be summarized as:

$$\phi_j = (c_j + b_j c_{j-1}) / T_j + A_j \phi_{j-1} ; \quad j = 2, 3, \dots, NY-1$$

with $T_j = d_j - b_j A_{j-1}$

$$A_j = a_j / T_j$$

$$A_1 = C_1 = 0$$

Note that the "forward substitution" for the calculation of C_j , A_j and T_j is performed from $j = 2$ to $j = NY-1$, while the "backward substitution" for the calculation of ϕ_j is performed from $j = NY-1$ to $j = 2$.